

University of Warwick institutional repository: <http://go.warwick.ac.uk/wrap>

A Thesis Submitted for the Degree of PhD at the University of Warwick

<http://go.warwick.ac.uk/wrap/69105>

This thesis is made available online and is protected by original copyright.

Please scroll down to view the document itself.

Please refer to the repository record for this item for information to help you to cite it. Our policy information is available from the repository home page.



**Detector Development for a Neutrino Detector with
Combined Optical and Charge Readout in Room
Temperature Liquids**

by

Nicola McConkey

Thesis

Submitted to the University of Warwick

for the degree of

Doctor of Philosophy

Department of Physics

June 2014

THE UNIVERSITY OF
WARWICK

Contents

List of Tables	iii
List of Figures	iv
Acknowledgments	ix
Declarations	xi
Abstract	xii
Chapter 1 Introduction	1
Chapter 2 Background and Theory	2
2.1 Motivation - Neutrino Physics	2
2.1.1 The Neutrino	2
2.1.2 Neutrino Oscillations	4
2.1.3 Neutrino Mixing	7
2.1.4 Neutrinoless Double Beta Decay	10
2.2 Neutrino Detectors	13
2.2.1 Overview of Detectors in Current Long Baseline Neutrino Experiments	13
2.2.2 Overview of Current Detectors for Double Beta Decay Experiments	16
2.2.3 Future Long Baseline Neutrino Experiments	20
2.3 Detector Technology	22
2.3.1 Ionisation Chambers	22
2.3.2 Multiwire Proportional Counters	24
2.3.3 Time Projection Chambers	24
2.3.4 Thick Gas Electron Multipliers	26
2.3.5 Preamplifiers	28

2.4	Charge Transport in Liquids	30
2.4.1	Theory of Charge Transport in Liquids	30
2.4.2	History of Charge Transport in Room Temperature Liquids	33
2.4.3	Organic Liquid Scintillators and Solvents	37
2.4.4	Liquid Argon	39
2.5	A Room Temperature Liquid Time Projection Chamber	40
Chapter 3 Detector Design and Construction		41
3.1	Radioactive Sources summary	41
3.2	Organic Liquids summary	44
3.3	Wire Proportional Counter	44
3.4	Gridded Ionisation Chamber	47
3.5	Multiwire Proportional Counter	54
3.6	Optical Readout Test Stand	57
3.7	Dark Current Measurements	64
3.8	Data Acquisition Systems	66
3.9	Data Processing Tools	68
Chapter 4 Results		72
4.1	Optical Readout	72
4.1.1	Absorption and Emission Spectra	72
4.1.2	Alpha and Beta spectra	78
4.2	Charge Readout	97
4.2.1	Initial Experiences	97
4.2.2	Event Rates	100
4.2.3	Dark Current	110
4.3	Optical readout of a THGEM in liquid scintillator	121
Chapter 5 Discussion and Conclusions		125

List of Tables

2.1	Currently known leptons and their flavours.	4
2.2	The 2014 best fits for the neutrino mixing parameters, taken from [28].	9
2.3	Extracted data from a table in [47], showing the sensitivity of a selection of double beta decay experiments	17
2.4	Charge transport properties for a selection of liquids, extracted from [79] and [67]	34
2.5	The organic liquids and solvents tested and their molecular structure.	38
3.1	Summary of radioactive source properties	42
3.2	The decay chain for thorium 232, extracted from [96]	43
3.3	Summary of organic liquids	44
3.4	Parallel plate distances in the dark current detector, and corresponding E fields	64
3.5	The calculated pulse parameters, and their functions.	71
4.1	The Muon energy deposited in each liquid	80
4.2	Comparison of the performance of PMTs 1 & 2 and 2 & 3	84
4.3	Summary table for optical measurements	98

List of Figures

2.1	Feynman diagrams of three examples of neutrino interaction: charged current (A), neutral current (B) and elastic scattering (C).	5
2.2	An illustration of the normal and inverted hierarchy of neutrino mass states from [26]	8
2.3	Feynman diagrams for 2ν beta decay (left) and neutrinoless double beta decay (right) from [16]	11
2.4	The continuous energy spectrum for two neutrino beta decay, and the delta peak from neutrinoless double beta decay, from [38].	12
2.5	Three reconstructed images from the ICARUS test run.	15
2.6	Schematic of a gaseous ionisation chamber.	22
2.7	Schematic of a gridded ionisation chamber.	23
2.8	A plot of the electric field lines created by a MWPC.	25
2.9	Schematic of a time projection chamber.	25
2.10	A finite element calculation image created using COMSOL [106], showing the electric field strength surrounding a THGEM.	27
2.11	A schematic diagram of how a THGEM works in liquid argon.	28
2.12	Circuit diagram for a current or voltage sensitive preamplifier.	29
2.13	Diagram of a charge sensitive “feedback” amplifier.	30
2.14	Mobilities of various liquids, from [72]. The dashed line separates liquids with a mean free path Λ above and below the de Broglie λ wavelength of thermalised electrons.	31
2.15	The charge yield of tetramethylpentane (TMP), a room temperature liquid and liquid argon (LAr) as a function of electric field, from [74].	32
2.16	Background current density as a function of time in n-heptane, taken from [84].	36
3.1	Schematic of the wire proportional counter.	45

3.2	Americium 241 alpha spectrum in argon gas, taken using the Wire Proportional Counter with the source collimated and pointing along the direction of the wire. The red line shows a Gaussian fit, with mean value 77.7 ± 0.2 and standard deviation 10.3	46
3.3	The initial circuit diagram for a custom-made voltage-sensitive preamplifier	46
3.4	Calibration curve for voltage-sensitive preamplifiers, created by inputting delta pulses across a 1.6 pF capacitor.	47
3.5	Circuit diagram for the custom-made 4 channel DC power supply.	48
3.6	A photo of the gridded ionisation chamber in its initial configuration.	49
3.7	A schematic diagram of the view from above of the gridded ionisation chamber detector lid with all dimensions, holes, and connections.	50
3.8	The circuit diagram for the modified voltage-sensitive preamplifier.	51
3.9	A schematic diagram of the rebuilt gridded ionisation chamber, with the anode and grid at the bottom of the chamber, with two power supply circuits.	53
3.10	The energy spectrum from an americium 241 alpha source in the gridded ionisation chamber in argon gas at an anode voltage of 100 V. The red line shows a Gaussian fit of the data, with mean 1.72 ± 0.01 and standard deviation 0.12.	54
3.11	A COMSOL image showing a cross-section through part of the MWPC detector.	56
3.12	A schematic showing the signal path in the MWPC.	57
3.13	The multiwire proportional counter.	58
3.14	The α energy spectrum from the multiwire proportional counter for the thorium 232 source in argon gas at a cathode voltage of 2000 V. The red line shows a Gaussian fit to the data, with mean 0.471 ± 0.003 and standard deviation 0.082.	59
3.15	Quantum efficiency as a function of incident light wavelength for the PMT type 9954B, copied from [107].	59
3.16	Circuit for the custom-made voltage preamplifiers used for the PMTs.	60
3.17	The TAC spectrum for the two PMTs, with no source present in the detector.	61
3.18	The TAC spectrum for two PMTs looking at the dish containing the liquid scintillator cocktail Ecoscint O, with the thorium source.	61
3.19	The optical readout detector system.	62

3.20	Dark current detector comprising seven drift chambers of varying drift distances.	65
3.21	Dark current detector system.	65
3.22	The Block Diagram for the LabVIEW data acquisition code.	67
4.1	The light emission (red) and absorption (black) spectra for Di isopropyl naphthalene.	74
4.2	The light emission (red) and absorption (black) spectra for Mono isopropyl naphthalene.	75
4.3	The light emission (red) and absorption (black) spectra for Mono isopropyl biphenyl.	75
4.4	The light emission (red) and absorption (black) spectra for Phenyl xylyl ethane.	76
4.5	The light emission (red) and absorption (black) spectra for Cyclopentane.	77
4.6	The light emission (red) and absorption (black) spectra for Tetramethyl pentane.	77
4.7	The average decay time in Ecoscint for americium (alpha) and muon (beta) pulses.	80
4.8	The thorium energy spectrum in Optifluor O, without cuts (blue) and with alpha (red) and beta (green) selections.	81
4.9	A double pulse observed in DIN, in PMT 1 (upper) and PMT 2 (lower): possible evidence of the Bi 212 and Po 212 decays in the thorium decay chain.	82
4.10	The energy spectrum for Ecoscint O, showing the americium alpha, thorium alpha contributions, thorium beta contributions, and the muons.	83
4.11	The energy spectra for americium and 2 cm muon depth in Ecoscint O, with PMTs 1 & 2, and PMTs 2 & 3.	86
4.12	The energy spectrum for Optifluor O, showing the americium alpha, thorium alpha contributions, thorium beta contributions, and the muons.	86
4.13	The energy spectrum for DIN, showing the americium alpha, thorium alpha contributions, thorium beta contributions, and the muons.	87
4.14	The energy spectrum for PXE, showing the americium alpha, thorium alpha contributions, thorium beta contributions, and the muons.	89

4.15	The energy spectrum for MIPN, showing the americium alpha, thorium alpha contributions, thorium beta contributions, and the muons.	90
4.16	The energy spectrum for the initial MIBP measurement, using PMTs 1 and 2, showing the americium alpha, thorium alpha contributions, thorium beta contributions, and the 2 cm depth muons.	92
4.17	The energy spectrum for the repeat MIBP measurement, using PMTs 2 and 3, showing the americium alpha, thorium alpha contributions, thorium beta contributions, and muons.	93
4.18	The energy spectrum for TMP, showing the thorium source and the muons.	95
4.19	The energy spectrum for C5, showing the americium alpha, thorium source, and the muons.	96
4.20	Pulse (a) is an example of a pulse shape typically observed in the DIN-filled wire proportional counter. Pulses (b) and (c) are two pulse populations observed in the DIN-filled gridded ionisation chamber. The time binning is 10 ns per bin for figure (a), and 5 ns per bin in (b) and (c).	99
4.21	Event rate as a function of electric field in DIN solvent (black) and Ultima Gold F cocktail (red).	101
4.22	Event rate as a function of electric field in MIPN solvent.	102
4.23	Event rate as a function of electric field in MIBP solvent.	102
4.24	Total event rate as a function of electric field in LAB scintillator cocktail.	103
4.25	The event rate as a function of electric field in Ecoscint O.	103
4.26	Drift speed as a function of electric field, in MIBP.	105
4.27	Drift speed as a function of electric field, in MIPN.	106
4.28	Drift speed as a function of drift field, in DIN.	106
4.29	A scatter plot of two pulse fitter parameters, showing two distinct populations in a data sample taken with 3.2 kVcm^{-1} drift field. . . .	107
4.30	A contour plot of two pulse fitter parameters, showing two populations which are not very well separated, in a data sample taken with 5.1 kVcm^{-1} drift field.	108
4.31	A histogram of the rise time pulse parameter at a drift field of 3.2 kVcm^{-1} , showing histograms of the uncut sample, the pulse fitter-based cut selection, and the parameter-based cut selection	109

4.32	The drift speed in DIN as a function of electric field, showing the uncut sample (blue), the pulse fitter-based cut selection (green), and the parameter-based cut selection (red).	109
4.33	A scatter plot of two pulse fitter parameters, which shows a concentration of pulses, but no distinct populations, in a sample taken with 4.6 kVcm^{-1} drift field.	110
4.34	Background pulse rate in DIN at a field of 5 kVcm^{-1}	111
4.35	Total PXE event rate at 2.5 kVcm^{-1} , with no cuts.	112
4.36	Left: Event rate of cut selection at 2.5 kVcm^{-1} . Right: Selected pulse type, with sampling window of $1500 \mu\text{s}$, with 5 ns per time bin. . . .	113
4.37	Left: Event rate of cut selection at 2.5 kVcm^{-1} . Right: Selected pulse type, with sampling window of $1500 \mu\text{s}$, with 5 ns per time bin	113
4.38	Total event rate PXE at 11 kVcm^{-1}	114
4.39	Left: Event rate of cut selection at 11 kVcm^{-1} , fit with a straight line at a rate of 131 events. Right: Selected pulse type, with sampling window of $750 \mu\text{s}$, with 5 ns per time bin.	115
4.40	Dark current in DIN as a function of time and electric field.	116
4.41	Dark current in Ultima Gold F as a function of time and electric field.	117
4.42	The dark current as a function of drift field in DIN (black) and Ultima Gold (red).	117
4.43	Dark current in Optifluor O as a function of time and electric field.	118
4.44	The dark current as a function of electric field for Optifluor O.	119
4.45	Dark current in PXE as a function of time and electric field.	120
4.46	Pulse amplitude as a function of time with a drift field of 5 kVcm^{-1}	122
4.47	Event rate as a function of drift field, fitted with a straight line at 5188 ± 29 events per 20 hours.	122
4.48	Event rate as a function of time, with THGEM operational. Each consecutive sample lasted 5 hours.	123

Acknowledgments

It is only right that the first person I thank in this thesis is my supervisor, Yorck Ramachers, who has been excellent in that capacity, both to work with and learn from. Above all, he is an incredibly good person to discuss physics with.

I would also like to extend my thanks to the entire Warwick Experimental Particle Physics group, for providing such a friendly and supportive environment to work in. All those with whom I've shared an office over the years have influenced my approach to physics, increasing both my knowledge and my cynicism. I would especially like to thank Leigh Whitehead, for his help in proofreading bits of my thesis.

I would very much like to thank Bob Day and Dave Greenshields in the Electronics Workshop, for tirelessly designing, repairing and modifying preamplifiers and power supplies for me! The Mechanics Workshop have also been instrumental in bringing my detectors into being, especially Andy Sheffield, Bob Bridgeland and Jon Tizick. I also want to thank Duncan Brealey, since the Physics Stores is an invaluable resource, and one of my favourite places in the department!

Over the course of this PhD I have had an incredible amount of support from friends, family and colleagues. I would most like to thank Jen Morgan, and Adam Griffin, for both keeping me relatively sane by drinking tea with me, and Warwick Folk Society, for keeping me entertained in between the physics.

My parents have encouraged me at every step to pursue my interests, and therefore I must thank them for helping me to get to where I am today; in the very interesting field of neutrino physics.

Above all, I would like to acknowledge my husband Jake, who has supported

and encouraged me throughout my PhD, and endured with patience and good nature my writing up period. His unwavering support and faith in my ability have helped me through the difficult times!

Declarations

This thesis is submitted to the University of Warwick in support of my application for the degree of Doctor of Philosophy. It has been composed by myself and has not been submitted in any previous application for any degree, apart from some of the background material in sections 2.1 - 2.3, which was previously submitted for an MSc by Research degree in Physics at the University of Warwick [1].

The work presented (including data generated and data analysis) was carried out by the author except in the cases outlined below:

The two voltage sensitive preamplifiers, the high voltage power supply, and the multichannel preamplifier power supply were all designed, built, and repaired by Bob Day and Dave Greenshields in the Warwick Electronics Workshop. The printed circuit boards for the dark current detector were designed and etched by Bob Day.

The gridded ionisation chamber componenets, multiwire proportional counter frame, two detector chambers, their lids, support structures, and internal mounting structures were all manufactured by Bob Bridgeland, Jon Tizik and Andy Sheffield in the Warwick Mechanics Workshop.

The pulse fitter code was written by Yorck Ramachers.

Parts of the work in chapter four of this thesis have been published by the author: [2],[3].

Abstract

A room temperature liquid scintillator time projection chamber has the potential to give both fine grained tracking and calorimetry, analogous to liquid argon, only without the cryogenic infrastructure. This type of detector would be invaluable as a cost effective, large volume detector for use in neutrino physics.

This motivates the search for candidate liquids with both excellent charge transport properties and optical properties. This work presents results from tests of five dielectric room temperature liquid scintillators; Di isopropyl naphthalene, Phenyl xylyl ethane, Linear alkyl benzene, Mono isopropyl biphenyl, and Mono isopropyl naphthalene, whose charge transport properties are investigated for the first time. The results are also presented from room temperature liquids Tetramethyl pentane, and Cyclopentane, whose optical properties have not previously been investigated.

The liquids tested have shown favourable properties, although none of the above liquids has been found to have both charge transport and scintillation light at a suitable level for use in a neutrino detector.

Chapter 1

Introduction

The field of this thesis is experimental particle physics.

The topic is detector physics, specifically research into the feasibility of a room temperature liquid scintillator time projection chamber (TPC), and development of prototype detectors to test the charge transport and optical properties of room temperature liquids. The motivation for this is to offer a cost effective alternative to liquid noble gas detectors in neutrino physics.

This thesis presents a comprehensive description of the challenging experimental work undertaken, and gives the results of these experiments in the context of their successes and failures, with an outlook to future work in this area.

Chapter 2 aims to convince the reader that the work in this thesis is well motivated, giving an overview of relevant parts of the field of neutrino physics, and highlighting the context in which the technology sits. In addition, this chapter gives the background details of each of the detector technologies used in the thesis.

Chapter 3 includes a detailed description and discussion of the detectors designed, built, commissioned and operated in each of the experiments.

Chapter 4 presents and reviews results from each of the experiments. Chapter 5 discusses these results in the context of the thesis, and gives a conclusion.

Chapter 2

Background and Theory

2.1 Motivation - Neutrino Physics

This section covers the relevant theoretical topics to motivate the creation of detectors with which to study the properties of neutrinos.

2.1.1 The Neutrino

The neutrino was postulated in 1930, by Pauli [4], as a solution to problems in nuclear physics with the observed β decays:

$$(Z, A) \rightarrow (Z + 1, A) + e^- + \bar{\nu} \quad (2.1)$$

and

$$(Z', A') \rightarrow (Z' - 1, A') + e^+ + \nu \quad (2.2)$$

where (Z, A) is a nucleus with atomic number Z , mass number A [5].

Beta decay had previously been considered only as a two body process, which would result in a single decay energy for the emitted electrons. This was incompatible with the observation of a continuous energy spectrum for beta decay, made by Chadwick in 1914 [6]. A theory of beta decay including the third, undetected particle suggested by Pauli, was put forward by Fermi in 1934 [7].

The third particle involved in beta decay also allowed conservation of angular momentum in the interaction. The decay of a half-integer spin parent nucleus had been shown to produce a half-integer spin daughter nucleus; with the added emission of a spin- $\frac{1}{2}$ electron, angular momentum conservation would not hold true unless another spin- $\frac{1}{2}$ particle was included.

The neutrino, an electrically neutral particle with a very small interaction

cross-section, (of the order of $\bar{\sigma} = 10^{-44} \text{ cm}^2$ (p5,[5])) was discovered experimentally 26 years later. The interaction

$$\bar{\nu} + p \rightarrow e^+ + n \quad (2.3)$$

was measured by Reines and Cowan [8], using the antineutrinos being produced by the β decay in a U-235 nuclear reactor.

In 1959 it was suggested by Pontecorvo [9] that the neutrinos emitted in pion decay might be different from those emitted in β decay. If the neutrinos (ν_e and ν_μ) were identical, the reactions

$$\nu_\mu + n \rightarrow \mu^- + p \quad (2.4)$$

and

$$\nu_\mu + n \rightarrow e^- + p \quad (2.5)$$

(and their inverse reactions) would result at the same rate, but if ν_e and ν_μ were distinct particles, the latter would not be observed. At Brookhaven this was tested using a neutrino beam, which provided evidence that $\nu_e \neq \nu_\mu$ [10].

The existence of more than one flavour of neutrino prompted questioning of how many flavours were in existence, and how they corresponded to the other leptons known to exist, for instance, when the tau lepton was discovered in 1975 [11].

A partial answer to this question was provided in the late '80s by the Large Electron Positron collider (LEP) [12]. Extremely precise measurements were made of the total decay width Γ_Z of the Z^0 boson resonance. The partial decay widths of Z to quarks and charged leptons are given by electroweak theory and, when summed and subtracted from the measured total decay width, give a decay width for light neutrinos, $\Gamma_{\nu\text{Total}}$, defined as the following:

$$\Gamma_{\nu\text{Total}} = N_\nu \cdot \Gamma_\nu \quad (2.6)$$

where N_ν is the number of flavours of neutrinos, and Γ_ν is the decay width to a neutrino, as calculable. The data from LEP gives the following result [13],

$$N_\nu = 2.9841 \pm 0.0083 \quad (2.7)$$

which matches well with the number of extant lepton flavours, 3. The three flavours of light neutrino are ν_e , ν_μ and ν_τ . Any other neutrinos must be either more massive than half of the mass of the Z^0 boson, and would therefore be unable to contribute

Table 2.1: Currently known leptons and their flavours.

Flavour		
Electron, e^-	Muon, μ^-	Tau, τ^-
Positron, e^+	Anti muon, μ^+	Anti tau, τ^+
Electron neutrino, ν_e	Muon neutrino, ν_μ	Tau neutrino, ν_τ
Electron antineutrino, $\bar{\nu}_e$	Muon antineutrino, $\bar{\nu}_\mu$	Tau antineutrino, $\bar{\nu}_\tau$

to the decay width, or non-coupling to the Z - i.e. sterile neutrinos, or both, of course. There have been hints of the existence of a fourth generation of neutrinos [14] but as yet, no conclusive evidence.

The tau neutrino was first observed experimentally in 2000 by DONUT [15]. The currently known leptons are shown in table 2.1.

2.1.2 Neutrino Oscillations

The oscillation of a neutrino from one flavour state to another is a quantum mechanical phenomenon which is theoretically possible in the event that the weak and mass eigenstates are not identical. This means that the propagation state of a neutrino is different from its weak interaction state. This type of flavour oscillation is well known in the quark sector, where the mixing is described by the Cabbibo-Kobayashi-Maskawa (CKM) matrix [16].

There is substantial experimental evidence to support the existence of neutrino oscillations, an overview of which is presented.

The Solar Neutrino Problem

The nuclear fusion processes occurring in the solar core make the sun a high luminosity source of electron neutrinos. Knowledge of this source is gained by studying the thermonuclear processes and creating a Standard Solar Model (SSM) of the behaviour of the sun [16]. An SSM also uses the observed data for the luminosity and radius of the sun, as well as the heavy-element-to-hydrogen ratio at the surface of the sun. Many different SSMs have been created, allowing predictions of the solar neutrino flux.

The first experiment to measure the solar neutrino flux was the Homestake experiment, in 1968 [17]. This was a radiochemical experiment, using chlorine-argon decays, which was sensitive to neutrinos with an energy greater than 0.814 MeV. The observed ν_e flux was only one third of that predicted by the SSMs of the time [18].

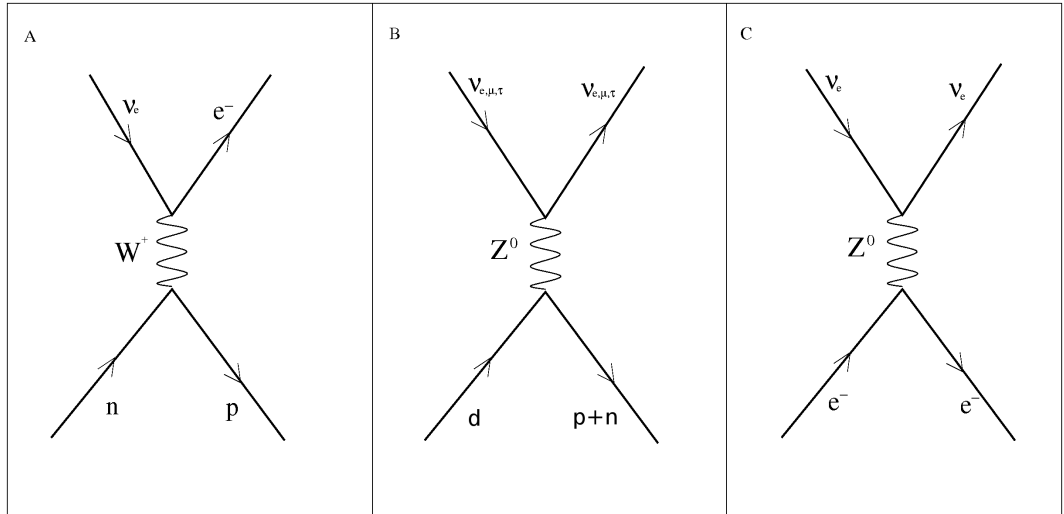


Figure 2.1: Feynman diagrams of three examples of neutrino interaction: charged current (A), neutral current (B) and elastic scattering (C), as measured at SNO.

This incompatibility of measurement and model was initially put down to a fault in the experiment, but was subsequently shown independently to be correct.

Further radiochemical solar neutrino experiments such as GALLEX/GNO [19], and SAGE [20], detectors using gallium, had a lower energy threshold than chlorine, and therefore were sensitive to lower energy neutrinos, but similarly resulted in disagreement with the SSM. The water Čerenkov detectors Kamiokande and Super-Kamiokande also observed solar neutrinos, measuring fluxes of half, and just less than half of those predicted by the SSM [21].

It was evident there was a large discrepancy between the observed solar neutrino flux, and the standard solar model. This became known as the Solar Neutrino Problem.

The SNO experiment provided crucial evidence which helped to solve this problem [22]. SNO was a heavy water Čerenkov detector, which enabled it to measure three types of neutrino interactions: charged current interactions (CC), elastic scattering on electrons (ES), but also neutral current (NC) interactions on deuterium (see figure 2.1 for Feynman diagrams of an example of each process). Similar to the Kamiokande experiments, the neutrinos detected through CC processes must be ν_e , due to the threshold energies of the processes involved. The NC interaction, however is equally sensitive to all active neutrino flavours.

The flux of CC interactions measured by SNO was about one third of the measured NC flux (p380,[16]). This was evidence of incident non ν_e neutrinos; previous solar neutrino experiments were not able to observe all of the incident

neutrino flavours, hence they observed a smaller flux than predicted.

From the SNO data, calculations of the total ν_μ and ν_τ flux were made, and the total flux of all three neutrino flavours is in agreement with the standard solar models.

This evidence suggested an oscillation between flavours for the solar neutrinos between production in the solar core, and observation on earth. A global fit of the data from the above experiments shows that the neutrino mixing angle for this oscillation is large, but not maximal.

Atmospheric Neutrinos

Atmospheric neutrinos are created as a result of the interactions of primary cosmic rays with the nuclei in the atmosphere [16]. Neutrinos are produced by the decay of secondaries, predominantly pions:

$$\pi^+ \rightarrow \mu^+ + \nu_\mu \quad (2.8)$$

$$\pi^- \rightarrow \mu^- + \bar{\nu}_\mu \quad (2.9)$$

The muons also subsequently decay,

$$\mu^+ \rightarrow e^+ + \nu_e + \bar{\nu}_\mu \quad (2.10)$$

$$\mu^- \rightarrow e^- + \bar{\nu}_e + \nu_\mu \quad (2.11)$$

resulting in a neutrino flux of electron and muon neutrinos, with approximately twice as many ν_μ and $\bar{\nu}_\mu$ than ν_e and $\bar{\nu}_e$.

In the late 1980s the Kamiokande experiments observed a significantly smaller flux of atmospheric neutrinos than was predicted by Monte Carlo models. The observed deficit was found to be only in the ν_μ sector, with the ν_e matching the predictions. This became known as the *atmospheric neutrino anomaly*. It was a controversial result at the time, since other atmospheric neutrino experiments, such as Frejus had not observed any anomaly, and the IMB experiment found an anomaly for only a certain energy range of ν_μ events.

In 1998 an important result [23] was presented by the Super-Kamiokande collaboration, leading to the resolution of the problem. As a Čerenkov detector, Super-K was able to determine the direction of the incoming neutrino. An asymmetry was observed between down and up going ν_μ events: events caused by neutrinos from the atmosphere directly above the detector, and those neutrinos which had passed through the centre of the earth before reaching the detector, respectively.

The up going neutrino flux was measured to be considerably smaller than the down going counterpart, whereas the ν_e fluxes were as expected, equal.

The atmospheric neutrino anomaly observed by Kamiokande, IMB and Super-Kamiokande has since been observed by Soudan 2 [24], and using beamline neutrinos, in K2K [25]. This provides strong evidence to support the disappearance of atmospheric muon neutrinos travelling through the earth. This fits in extremely well with the neutrino oscillation theory, which states that the oscillation probability for neutrinos is dependent on $\frac{L}{E}$, where L is the distance from source to detector, and E is the energy of the neutrino.

The ν_e flux for up and down going neutrinos appeared equal, since the loss of ν_e due to oscillations is compensated by the oscillation from ν_μ to ν_e . The oscillation probability is discussed in section 2.1.3 and the mixing matrices are shown in equation 2.13.

Many further neutrino experiments have provided supporting evidence for neutrino oscillations, especially using other sources of neutrinos, such as nuclear reactors, and neutrino beams. Neutrino oscillation is now a widely accepted theory, and experiments set out to measure, with increasing accuracy, the mixing angles involved.

2.1.3 Neutrino Mixing

The evidence presented in section 2.1.2 suggests the existence of neutrino oscillations, which implies the mass and flavour eigenstates for neutrinos are different. This has the implication that neutrinos are massive, a subject further discussed in section 2.1.4.

Two Flavour Oscillation Probability

Let us consider for simplicity the oscillation probability in a two neutrino system [5]:

$$P_{\nu_\alpha \rightarrow \nu_\beta} = \frac{1}{2} \sin^2 2\theta \left(1 - \cos \left(\frac{\Delta m^2 L}{2E} \right) \right) \quad (2.12)$$

where α and β represent the two flavour states, theta is the mixing angle between the two states, Δm^2 is the mass squared difference between the two propagation states ($m_i^2 - m_j^2$), L is the oscillation length, and E is the energy of the neutrino.

Since L and E are experimental variables, this leaves two parameters to measure, the mixing angle and mass difference, or in the three flavour case, the three mixing angles, and the two mass differences. Since the sign of one of the mass

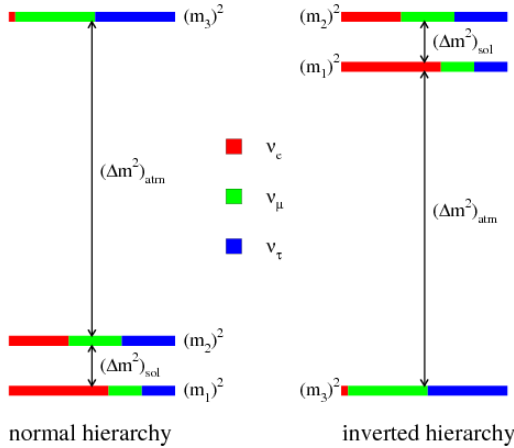


Figure 2.2: An illustration of the normal and inverted hierarchy of neutrino mass states from [26]

differences has been measured in the solar neutrino sector, the problem is reduced to a single unknown, the so called *mass hierarchy*.

There are two possible orderings of the neutrino masses, the "normal hierarchy" and the "inverted hierarchy". These are shown in figure 2.2. In the normal hierarchy there are two light neutrino mass states, and one correspondingly heavier neutrino state. In this instance Δm_{23}^2 is positive. In the inverse hierarchy there are two heavy neutrino mass states, and one light neutrino mass state, when Δm_{23}^2 is negative.

An overview of some of the experiments measuring these oscillation parameters is given in section 2.2.1.

Mixing Matrices for Three Flavour Oscillation

The neutrino flavour eigenstates, $|\nu_e\rangle$, $|\nu_\mu\rangle$, $|\nu_\tau\rangle$ are proposed to be linear combinations of the neutrino mass eigenstates, $|\nu_1\rangle$, $|\nu_2\rangle$, $|\nu_3\rangle$ [5]. The coefficients for this linear combination are given by the Pontecorvo-Maki-Nakagawa-Sakata (PMNS) matrix [27]. The PMNS matrix multiplied by the mass states gives the weighted flavour states we observe by the weak interaction, as is shown by the following equation.

$$\begin{pmatrix} \nu_e \\ \nu_\mu \\ \nu_\tau \end{pmatrix} = \begin{pmatrix} U_{e1} & U_{e2} & U_{e3} \\ U_{\mu1} & U_{\mu2} & U_{\mu3} \\ U_{\tau1} & U_{\tau2} & U_{\tau3} \end{pmatrix} \begin{pmatrix} \nu_1 \\ \nu_2 \\ \nu_3 \end{pmatrix} \quad (2.13)$$

Table 2.2: The 2014 best fits for the neutrino mixing parameters, taken from [28].

Parameter	Value
$\sin^2(2\theta_{12})$	0.846 ± 0.021
$\sin^2(2\theta_{23})$ [normal mass hierarchy]	$0.999^{+0.001}_{-0.018}$
$\sin^2(2\theta_{23})$ [inverted mass hierarchy]	$1.000^{+0.000}_{-0.017}$
$\sin^2(2\theta_{13})$	$(9.3 \pm 0.8) \times 10^{-2}$
Δm_{21}^2	$(7.53 \pm 0.18) \times 10^{-5} \text{ eV}^2$
Δm_{32}^2 [normal mass hierarchy]	$(2.44 \pm 0.06) \times 10^{-3} \text{ eV}^2$
Δm_{32}^2 [inverted mass hierarchy]	$(2.52 \pm 0.07) \times 10^{-3} \text{ eV}^2$

The PMNS matrix, U can be expressed as the product of 3 rotation matrices, and a complex phase matrix [27]. In equation 2.14 the complex phase matrix is combined with the middle rotation matrix.

$$U = \begin{pmatrix} 1 & 0 & 0 \\ 0 & c_{23} & s_{23} \\ 0 & -s_{23} & c_{23} \end{pmatrix} \begin{pmatrix} c_{13} & 0 & s_{13}e^{-i\delta} \\ 0 & 1 & 0 \\ -s_{13}e^{i\delta} & 0 & c_{13} \end{pmatrix} \begin{pmatrix} c_{12} & s_{12} & 0 \\ -s_{12} & c_{12} & 0 \\ 0 & 0 & 1 \end{pmatrix} \quad (2.14)$$

where $s_{ij} = \sin \theta_{ij}$ and $c_{ij} = \cos \theta_{ij}$.

The angles θ_{ij} are the mixing angles between the propagation states ν_i and ν_j , they therefore determine what the probable oscillation between these two states is. The mixing between the two states is said to be *maximal* where $\theta_{ij} = \frac{\pi}{4}$. If $\theta_{ij} = 0$ then the oscillation probability is zero, and there is no oscillation between ν_i and ν_j . As of 2012 all of the mixing angles θ_{12} , θ_{23} and θ_{13} have been measured to be non-zero, as shown in table 2.2.

Current neutrino oscillation experiments aim to measure with greater precision the mixing angles, mass splittings, and the mass hierarchy, with a view to measuring the complex phase δ . The complex phase is the parameter which represents the $\hat{C}\hat{P}$ violation (discussed in the following subsection) present in neutrino oscillations. Determining its value is one of the ultimate goals for neutrino physics, as it determines how much $\hat{C}\hat{P}$ violation is present in the lepton sector.

The Matter Effect

Equations 2.12 and 2.14 in the sections above describe the oscillation of neutrinos as they propagate through a vacuum. In order to completely describe neutrino oscillations as terrestrially measured, we must consider the effect of propagation through matter. All flavours of neutrino will interact, but the electron neutrino is the only flavour which can interact via CC interactions, the others can only interact via the NC. This affects the oscillation probability, the full details of which are not presented here. This effect is known as the MSW effect after Mikheyev, Smirnov and Wolfenstein, who worked on the theory [29],[30].

Baryogenesis

In the early universe, immediately following the big bang, there is thought to have been matter and antimatter in equal amounts. This is clearly not currently the case. In 1967, Sakharov postulated that there were three conditions necessary for a matter-antimatter asymmetry to arise; for *baryogenesis*[31].

1. The existence of an interaction which violates baryon number.
2. The existence of \hat{C} and $\hat{C}\hat{P}$ violation. $\hat{C}\hat{P}$ violation is non-conservation of symmetry under the combined operations of charge conjugation (\hat{C}) and parity (\hat{P}). This means that in the baryon-number violating interaction of the first condition, there is, for example, a bias towards creation of baryons, rather than anti-baryons.
3. The existence of a thermal non-equilibrium state, which is necessary for any interactions to proceed at different rates in forward and reverse directions.

There has been some $\hat{C}\hat{P}$ violation observed in the quark sector, first seen in the decay of the K_{Long} and K_{Short} mesons [32], but also subsequently in B decays [33],[34].

The level of $\hat{C}\hat{P}$ violation observed is insufficient to fulfil the condition set by Sakharov. It is therefore important to search for $\hat{C}\hat{P}$ violation in the lepton sector, where evidence for leptogenesis [35], a process analogous to baryogenesis, might be found.

2.1.4 Neutrinoless Double Beta Decay

Since the discovery of neutrino oscillations, discussed in section 2.1.2, we know that at least two of the neutrino masses must be greater than zero, since the existence of

three flavour neutrino mixing in neutrino oscillations necessitates three distinct neutrino mass eigenstates. The absolute mass scale of the neutrinos however, remains unknown, with the current experiments only setting upper limits on the neutrino masses. The neutrino mass can be directly measured using spectrometry as in the KATRIN experiment [36]. The current limit, set by a combination of cosmological measurements is [37]:

$$\Sigma m_\nu < 0.230 \text{ eV}. \quad (2.15)$$

Another gap in our knowledge is the nature of the mass of the neutrino. In the Standard Model, neutrinos interact only via the weak interaction, in which parity is maximally violated. A Dirac neutrino can therefore only interact in this way if it is chirally left handed (similarly an antineutrino must be right handed). Since only left handed neutrinos and right handed antineutrinos have been observed, there is no evidence to disprove the possibility that a neutrino may be its own antiparticle - a Majorana particle.

Double beta decay gives us the opportunity to probe the Majorana nature of the neutrino as well as discover the absolute scale of the Majorana neutrino mass. Double beta decay is a nuclear process which occurs in a small number of isotopes. In double beta decay, two neutrons decay into two protons, each emitting an electron and an antineutrino, according to the formula [5].

$$(Z, A) \rightarrow (Z + 2, A) + 2e^- + 2\bar{\nu}_e \quad (2.16)$$

An analogue of this process has been postulated, in which no neutrinos are emitted during the decay. This doubly lepton number violating process would be possible in the instance that the neutrino is Majorana, and a neutrino could thus be emitted at one decay vertex and absorbed at the other, as illustrated in figure 2.3.

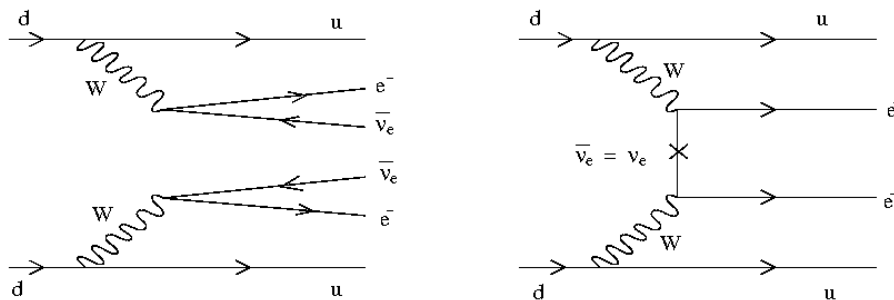


Figure 2.3: Feynman diagrams for $2\nu\beta\beta$ decay (left) and neutrinoless double beta decay (right) from [16]

Measuring neutrinoless double beta decay ($0\nu\beta\beta$) would not only allow us to

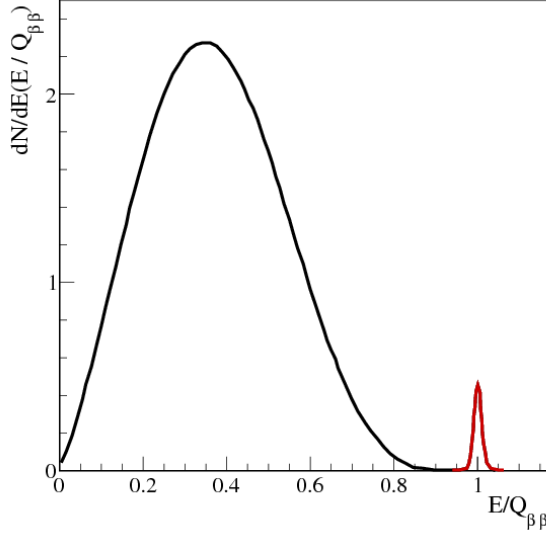


Figure 2.4: The continuous energy spectrum for two neutrino beta decay, and the delta peak from neutrinoless double beta decay, from [38].

determine whether neutrinos are Majorana, and observe lepton number violation, but also to measure the absolute scale of the neutrino masses.

The energy spectrum for the emitted electrons from two neutrino beta decay is a continuous distribution similar to that for beta decay. In the neutrinoless case however, the emission of two electrons from a nucleus at rest would lead to the particles being emitted with a fixed sum energy, therefore the energy spectrum for $0\nu\beta\beta$ is a discrete delta peak. This is illustrated in figure 2.4 (although the delta peak is affected by the resolution of any detector, so is shown as a Gaussian).

In order to measure the mass of the Majorana neutrino, one must measure the half-life of neutrinoless double beta decay, $T_{\frac{1}{2}}^{0\nu}$.

$$\left(T_{\frac{1}{2}}^{0\nu}\right)^{-1} = G_{0\nu}(Q_{\beta\beta}, Z) |M_{0\nu}|^2 m_{\beta\beta}^2 \quad (2.17)$$

where $G_{0\nu}$ is an exactly calculable phase space factor, $|M_{0\nu}|$ is a nuclear matrix element, and $m_{\beta\beta}$ is the effective Majorana mass of the electron neutrino:

$$m_{\beta\beta} = \left| \sum_i U_{ei}^2 m_i \right|, \quad (2.18)$$

where m_i are the mass eigenstates, and U_{ei} are elements of the neutrino mixing matrix in equation 2.14.

The uncertainties on the measurement of the neutrino mass are due to both

the half-life measurement, and the accuracy of the calculation of the nuclear matrix element (NME). The current status and limits set on the Majorana neutrino mass are discussed in section 2.2.2.

2.2 Neutrino Detectors

This section gives an overview of the current neutrino detectors relevant for long baseline neutrino physics and for neutrinoless double beta decay detection physics. It highlights the context in which the detector technology developed in this thesis would sit, and thereby contribute to the knowledge of neutrino physics.

2.2.1 Overview of Detectors in Current Long Baseline Neutrino Experiments

There are currently several long baseline neutrino beam experiments taking place. This section describes the main experiments, and their detectors.

MINOS and MINOS+

The primary aim of the MINOS [39] experiment was to measure θ_{23} and Δm_{23}^2 from the oscillations in the NuMI beam. The MINOS+ experiment, using the identical detectors sits parasitically in the NuMI beam to the NO ν A detectors (see below), and will search for sterile neutrinos.

The MINOS far detector is an 8 m wide tracking calorimeter, weighing 5.4 kton. Its 486 layers are composed of 1 inch thick planes of steel alternating with planes of scintillator strips. Each plane has 192 strips of scintillator, 4 cm wide and 1 cm thick, which are read out by photomultiplier tubes (PMT). Orthogonal strips in readout planes give 3D readout. The entire setup is in a 1.3 T toroidal magnetic field. The near detector has a similar composition, but is smaller, with a mass of 0.98 kton. The magnetisation of the detectors allows the charge of particles to be determined.

Interaction identification uses the distribution of the hadronic energy deposited, and the length of the muon tracks. This allows distinction between ν_e CC, ν_μ CC and NC events. Although these detectors have a large fiducial mass and tracking area, the tracking resolution is of the order of a centimetre, which means that detailed track resolution is not achievable.

MINOS have made the following measurements from muon neutrino and anti muon neutrino disappearance data (quoted for the normal hierarchy): $|\Delta m_{32}^2| = 2.37_{-0.09}^{+0.09} \times 10^{-3} eV^2$, $0.35 < \sin^2(2\theta_{23}) < 0.65$. The MINOS+ experiment started running in 2013 [40].

NO ν A

The NO ν A experiment [41] aims to measure θ_{13} , the mass hierarchy, and has some sensitivity to the $\hat{C}\hat{P}$ violating phase δ . The NO ν A detectors, sitting in the NuMI beam, are fine-grained tracking calorimeters consisting of cells filled with liquid scintillator (a mixture of pseudocumene and mineral oil), each of cross sectional size 6 cm x 4 cm. These planes alternate in horizontal and vertical planes, thus giving the detector some 3D tracking capabilities. Particle identification is aided by the granularity, and the fact that most of the detector is active scintillator.

The far detector is 14 kton, and the near detector 0.3 kton. The detectors can be constructed section by section, and the far detector is currently partially completed, and aims to be completed mid-2014. The near detector will also be completed in 2014, and the first beam measurements should take place before the end of the year.

OPERA

OPERA [42] is one of two neutrino detectors which operated in the CNGS beam. Its aim was to prove the atmospheric oscillation mode is ν_μ to ν_τ by observing the ν_τ , and to measure the mixing angle θ_{23} . The ν_τ CC interaction produces a tau lepton, which has a very short lifetime, before it decays, and therefore a very short path length, 87 μm long. The OPERA experiment was designed to resolve this tau decay kink.

The detector is composed of lead and emulsion bricks; emulsion, for fine grain tracking, and lead to increase the target mass of the detector. Layers of scintillators are inserted between the brick structures to aid with event location and triggering. A tracking resolution of 0.3 μm is attainable. On average 100 bricks per week were removed where events were triggered, and the emulsion developed. These were then scanned by automatic optical microscopes.

On the very small event scale, this detector is ideal; it is able to track any charged particles, and pinpoint decay vertices to extremely high precision, because of its resolution. The areas of high precision measurement are separated by lead, however, which means any event not entirely enclosed within the emulsion part of

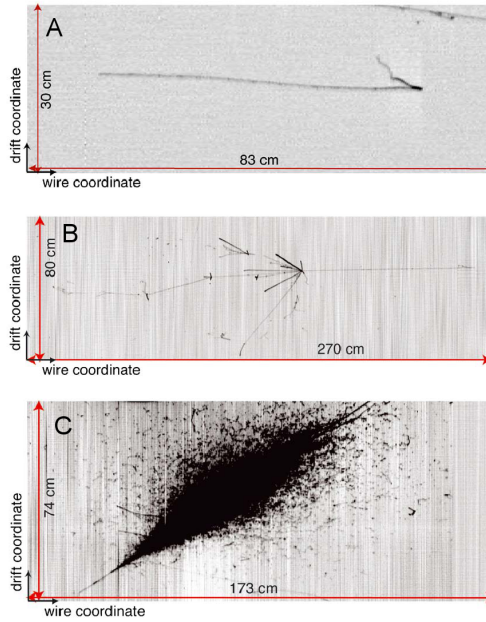


Figure 2.5: Three reconstructed images from the ICARUS test run [44]. Image **A** shows a muon track. Image **B** shows a hadronic interaction. Image **C** shows an electromagnetic shower.

the detector will not be trackable to this precision. It is well suited to its purpose, in that it can distinguish between ν_τ , ν_μ and ν_e in CC and NC interactions.

The OPERA experiment took data between 2008 and 2012. So far in their data analysis, they have found three ν_τ candidates, which excludes the absence of $\nu_\mu \rightarrow \nu_\tau$ oscillations at significance of 3.4σ [43].

ICARUS

Another neutrino detector which was operational in the CNGS beam is ICARUS [44]; a liquid argon TPC (see sections 2.3.3 and 2.4.4) with a mass of 600 tons. It has a readout plane made up of parallel wires, spaced at 3 mm, in three layers, oriented with the wires at angles of 60° to one another. Since the detector volume consists of only argon, there is fine-grained tracking throughout. The readout plane resolution is limited by properties of the detector material, such as the transverse diffusion (see section 2.4.1), but particle identification from the tracks detected is visually possible, as well as being calculable from the measurements of specific energy loss: $\frac{dE}{dx}$, the amount of energy deposited per unit length. Figure 2.5 shows three reconstructed events from ICARUS, illustrating this clarity.

It is evidently possible to distinguish between ν_μ and ν_e CC interactions with

ICARUS, but the ν_τ decay is more difficult to identify, since the τ decay kink is not resolvable. The track resolution allows e and π^0 event separation, hence NC events are distinguishable from CC events. This allows a good selection of a NC sample, and an indirect measurement of ν_τ flux.

The ICARUS detector has a sensitivity limited by statistics, due to its relatively small mass, but it was built as a prototype for a much larger detector, and as such is a significant contribution to neutrino detector technology.

The detector was taking data in the Gran Sasso laboratory from 2010 until 2013.

Super Kamiokande

Super Kamiokande [5] is a water Čerenkov detector, which serves as the far detector in the T2K beam. The T2K experiment aims to improve measurements of θ_{23} , θ_{13} , and Δm_{23}^2 , and have a sensitivity to some of δ_{CP} phase space. The inner detector volume is 50 ktons, whose surface is covered by over 10,000 PMTs, with active light collection from over 40% of the surface. The outer detector is used to distinguish between cosmic ray muon events and neutrino events.

The Čerenkov light cones are used for identifying the charged interaction products, the direction of the incident neutrinos is determined by the shape of the light cones, and the energy distribution of the recoil electrons gives the energy spectrum of the neutrinos.

The T2K experiment has measured electron neutrino appearance at a significance of 7.3σ , with a measurement of $\sin^2(2\theta_{13}) = 0.140_{-0.032}^{+0.038}$ for the normal hierarchy ($0.170_{-0.037}^{+0.045}$ for the inverted hierarchy) [45].

2.2.2 Overview of Current Detectors for Double Beta Decay Experiments

This section gives an overview of the existing and prospective detectors for double beta decay.

An ideal experiment to measure double beta decay would have a detector mass of 100% radioactive isotope, a perfect energy resolution, radiopurity and detection efficiency, and be scalable to large masses. Unfortunately this is not possible in reality, but each of the experiment types aims to optimise as many of these criteria as possible, with different compromises leading to an array of different measuring techniques [46],[47].

A direct comparison of the mass sensitivity of the detectors is difficult, since

Table 2.3: Extracted data from a table in [47], showing the sensitivity of a selection of experiments, using the lower half-life limit after 4 years of data-taking, and resulting range of Majorana neutrino masses from a variety of matrix element models. The quantities in brackets give values with detector upgrades.

Experiment	$T_{\frac{1}{2}}^{0\nu}/10^{25}yr$	$m_{\beta\beta}/meV$
EXO-200	4.2	75-170
NEXT	5.2	70-160
SNO+	0.8	100-240
Kamland-Zen	2.6 (15)	90-220 (40-90)
SuperNEMO	6.9	55-140
CUORE	7.5	50-110
GERDA	3.9 (18)	120-370 (60-170)
Majorana	17	60-170

the way that the measured quantity $T_{\frac{1}{2}}^{0\nu}$ relates to the $m_{\nu_{\beta\beta}}$ differs between isotopes, as shown in equation 2.17. The nuclear matrix element calculation currently gives large uncertainties to the measurement, since the calculation is heavily model dependent. Table 2.3 is an extract from a table in [47] giving comparable values for sensitivity, with the spread of neutrino mass coverage coming from the matrix element value variation. In addition, the phase space factor is much more favourable in some isotopes than others. The sensitivities in the following sections are those reported by the experiments themselves, and any differences may be due to the length of exposure time considered, or the matrix element used.

Xenon Time Projection Chambers

Xenon is a unique element in that it can form not only the active medium of a TPC (see section 2.3.3), but has also a double beta decaying isotope. This allows for almost the entire mass of the detector to be the source. Collection of both charge and scintillation light allows this detector type to have a very good energy resolution. The main drawback of these technologies is the cost; in spite of xenon being a comparatively easy isotope to enrich, the cost and abundance of the element itself limits the size of current detectors. [48]

EXO

The EXO-200 detector [49] is a liquid xenon TPC containing 110 kg of xenon, 80.6% of which is the double beta decaying isotope ^{136}Xe . The ionisation charge deposited in the detector is drifted to wire readout planes at either end of the cylindrical detector, and the scintillation light is read out by arrays

of avalanche photodiodes. The EXO detector has been running since 2011, setting a limit of $T_{\frac{1}{2}}^{0\nu} > 1.2 \times 10^{26}$ years.

NEXT experiment

The NEXT detector [50] is a proposed high pressure gaseous xenon TPC, the first iteration of which (NEXT-100) will contain 100 kg of Xe, enriched at 91% with the isotope ^{136}Xe . The cylindrical detector has PMTs at one end, and a fine wire mesh at the other, behind which there is an array of Multi-Pixel Photon Counters (MPPC). The signals collected by the detector are all optical; photons from the initial excitation due to the energy deposition give a t_0 , and the secondary scintillation light caused by avalanching of the drifted charges at the mesh anode. Due to the gaseous nature of the detector, the double beta decay signal leaves an ionisation track which is resolvable by the NEXT detector. This gives the experiment the distinct advantage of a topological signal, enabling excellent background rejection.

NEXT-100 is currently being constructed, and is expected to begin data-taking in 2015. It has a projected sensitivity to a Majorana neutrino mass of 100 meV after just 5 years of running.

Large Volume Calorimetry

This type of detector consists of a large active volume of liquid scintillator, doped with double beta decaying radioactive isotopes. The scintillation light is collected by light sensors surrounding the volume, and the high precision calorimetry is used to measure the particle decays. This detector type has the potential for a larger mass of isotope than the other detector types, since it is comparatively cost-effective to scale up in size. Background discrimination and energy resolution present more of a challenge in this type of detector, and tracking is not possible.

The SNO+ experiment

The SNO+ detector [51] contains 800 tonnes of the organic scintillator Linear Alkyl Benzene (LAB), in a 12 m diameter acrylic vessel. The scintillation light is read out by an array of 10,000 PMTs surrounding the vessel. Since the study of organic liquid scintillators comprises the main body of this thesis, the theory behind them will be discussed in a separate section, section 2.4.3.

The detector is in the construction and commissioning phase [52], and is currently filled with water. The transition to liquid scintillator will take place in 2015, with a view to loading the double beta decay isotope tellurium 130 at

the 0.3% level into the liquid by 2016. This will give the experiment sensitivity to a neutrino mass of 100 meV after 4 years. Following this demonstration phase, there are plans to increase the percentage of the double beta decaying isotope to improve the sensitivity.

KamLAND-Zen

The KamLAND-Zen detector [53] is composed of a spherical vessel containing 1kton pseudocumene and dodecane mixture (18%/82%), with a nylon film balloon suspended in the centre, containing 13 tons of the same liquid scintillator loaded with roughly 300 kg enriched xenon 136. The scintillation light is read out by PMTs surrounding the vessel. The current limit set by this detector on the neutrino mass is $m_{\beta\beta} < (300 - 600)$ meV, with a projected sensitivity to a Majorana mass of 80 meV at the end of the first stage of running.

Combined with data from EXO [54], an upper limit of $m_{\beta\beta}^{0\nu}$ is set, between 0.115 and 0.339 eV, depending on the choice of NME.

Tracking Calorimeters

The SuperNEMO experiment

SuperNEMO is a tracking detector, currently under construction, [48] which consists of foils of isotope sandwiched between layers of wire trackers, surrounded by a plastic scintillator calorimeter. It has the advantage of having the possibility of several different isotopes in the detector, selenium 82 being the baseline choice, but neodymium 150 and calcium 48 are also under consideration. With a total mass of 100-200 kg, it has sensitivity to $T_{\frac{1}{2}}^{0\nu} > 10^{26}$ years, giving an effective neutrino mass of 50-100 meV after 5 years of running [55].

High resolution Calorimetry

CUORE

CUORE [56] is a bolometer experiment, measuring the temperature change in TeO₂ crystals due to the double beta decay of tellurium 130. The CUORE experiment is currently under construction, and will consist of 988 bolometers, with a total isotope mass of 206 kg. It is the continuation of Cuorecino and CUORE-0 which were similar experiments with smaller isotope mass.

GERDA and Majorana

The GERDA [57] and Majorana [58] detectors are arrays of high purity germa-

nium (HPGe) detectors, enriched to around 86% with the double beta decaying isotope ^{76}Ge .

The GERDA detector is currently in phase I of operation, in which the detector has about 20 kg of enriched germanium. The second phase will roughly double the detector mass, giving it a sensitivity to a $0\beta\beta$ half-life of 1.1×10^{26} yr after 5 years of running. The current limit set by GERDA is $T_{\frac{1}{2}}^{0\nu} > 2.1 \times 10^{25}$ years at 90% confidence limit. In combination with other previous experiments using ^{76}Ge gives $T_{\frac{1}{2}}^{0\nu} > 3.0 \times 10^{25}$ years at 90% confidence limit.

The Majorana demonstrator has a mass of 40 kg, 75% of which will be enriched. Its aim is to demonstrate technology which can be scaled up to a tonne scale experiment without losing the energy resolution or purity.

This detector type has excellent energy resolution and high efficiency, but the isotope enrichment is costly presenting restrictions on the detector size. The ultimate goal of GERDA and Majorana is to merge the experiments to build a 1 tonne detector. [46]

2.2.3 Future Long Baseline Neutrino Experiments

This section describes three prospective neutrino experiments which are currently in the design stages.

Long Baseline Neutrino Experiment (LBNE)

The Long Baseline Neutrino Experiment [59], well described by its name, is an approved project, due to be completed in 2024. It will have the longest baseline to date of any neutrino beamline experiment, with its far detector in the Homestake mine, South Dakota, roughly 1300 km away from a 1 MW beam coming from Fermilab. The detector baseline design is a 10 kton liquid argon TPC, with wire plane readouts, broadly based on those used in ICARUS (see section 2.2.1). Upgrades are planned for both the beam power and the far detector volume (to 2.4 MW and 34 kton respectively), to increase the physics reach of the programme. LBNE is an on-axis detector, which allows it to measure both the first and second oscillation maxima. Because of the long baseline, the MSW effect allows a good sensitivity to the mass hierarchy. A measurement of δ_{CP} can also be made. The LAr TPC gives excellent separation of electron and muon events (see figure 2.5) which facilitates measuring both ν_e appearance and ν_μ disappearance, which allows for precision measurements of θ_{13} , θ_{23} , and Δm_{23}^2 . In addition there is a wide variety of physics

available to study with such a massive far detector - proton decay, supernova neutrino measurements, as well as the possibility of measuring lower energy solar, atmospheric and geoneutrinos.

Large Apparatus studying Grand Unification, Neutrino Astrophysics and Long Baseline Neutrino Oscillations(LAGUNA-LBNO)

LAGUNA-LBNO [60] is a feasibility study for a long baseline neutrino experiment in Europe. The proposed far detector site is in Pyhasalmi with a beam coming 2300 km from CERN. The beam powers would be similar to those proposed in LBNE, with an initial beam power of 600-700 kW, with potential upgrade to 2 MW. Indeed, the physics goals are almost identical to those of LBNE. The sole difference between the two, other than the baseline difference (and thus sensitivity), is the detectors. LBNO plan to also use a liquid argon far detector, with a “LEM-TPC” readout plane - this consists of a two phase detector, with THGEMs (see section 2.3.4) operating in the gas above the liquid argon medium. Two phase readout has so far been demonstrated at the 1 ton scale. The proposed size of TPC is 20 kton. A 35 kton magnetised iron calorimeter (MIND), similar to the MINOS detectors (as described in section 2.2.1) is also envisaged. The combination of these detectors is likewise sensitive to proton decay, supernova neutrinos, solar, atmospheric and geoneutrinos in addition to the beamline neutrinos.

Tokai to Hyper-Kamiokande (T2HK)

Hyper-Kamiokande [61] is a water Čerenkov detector based on the Super Kamiokande detector (as discussed in section 2.2.1) with roughly 25 times its fiducial mass. The detector design consists of two large cylindrical tanks lying side by side, with outer dimensions of 48 m x 54 m x 250 m, and total volume of 1 Mtonne. T2HK will be an off-axis experiment, sitting in an upgraded, 1 MW beam coming from J-PARC. The currently favoured site is roughly 8 km south of the Super-K, and 295 km away from J-PARC. T2HK will not be sensitive to the mass hierarchy as LBNE and LBNO because of the shorter baseline, but it would be more sensitive to δ_{CP} than either of the above experiments. Because of the extremely large volume of the detector, it will be even more sensitive to proton decay, supernova neutrinos, solar, atmospheric and geoneutrinos, as well as proton decay.

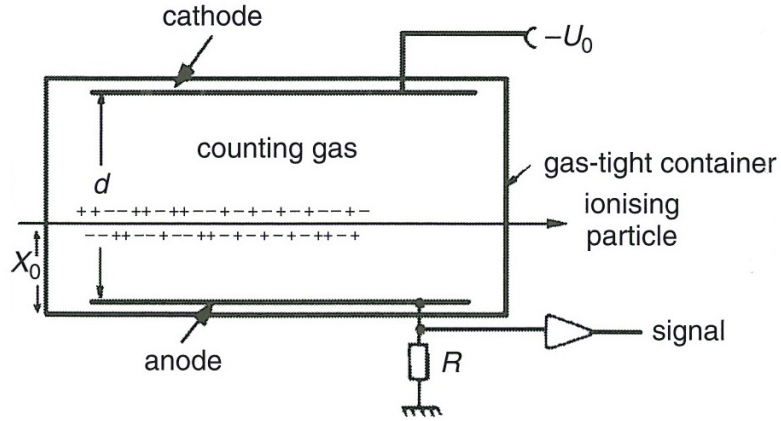


Figure 2.6: Schematic of a gaseous ionisation chamber, from [62], with bias of U_0 and electrode separation distance of d .

2.3 Detector Technology

This section describes various different detector types, and the formalism behind their operation. All of the detectors discussed in this section (excepting section 2.3.4) are drift chambers, for which the active medium can be any solid, liquid or gas capable of transporting charge. This is most typically a gas, usually noble gases and methane, but liquids can also be used for a higher target mass.

2.3.1 Ionisation Chambers

The simplest type of ionisation chamber is a pair of parallel plate electrodes. The amount of ionisation deposited in the active medium between the electrodes is drifted to the electrodes inducing a voltage, which is measured. The electric field is dependent on the voltage applied to the electrodes, according to the following equation:

$$|E| = \frac{U_0}{d} \quad (2.19)$$

where E is the electric field, U_0 is the voltage difference between the electrodes, and d is the electrode spacing, as shown in figure 2.6. The amount of charge deposited is dependent on the properties of the active medium.

Figure 2.6 illustrates the path of a charged particle in a gaseous ionisation chamber.

This type of ionisation chamber has a signal amplitude which is position-dependent, since the induced voltage is dependent on the initial position of the

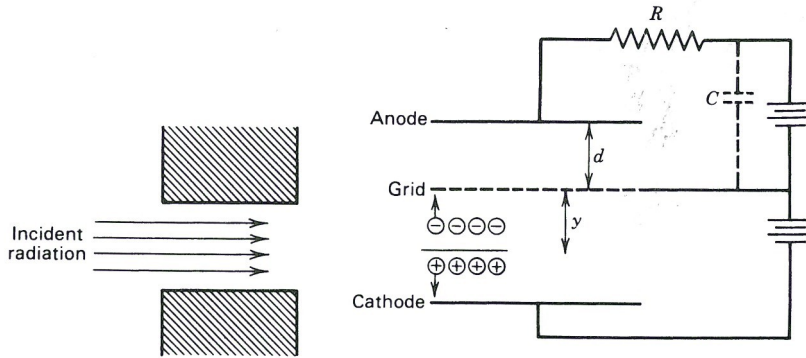


Figure 2.7: Schematic of a gridded ionisation chamber from [63]

charge, and its subsequent motion towards the anode. Position-independence can be achieved by implementing a Frisch grid into the chamber, between the two electrodes, as shown in figure 2.7. The Frisch grid is positioned close to the readout anode, on an intermediate voltage, so that moving charges in the drift space between the cathode and grid will induce voltage only on the grid. Only once charges have passed into the grid-anode space will a signal be induced on the readout anode. This gives position independence in the main detector volume.

In order to avoid charge loss at the grid, the electric fields between the cathode, grid and anode must be held at ratios such that the grid is optically transparent to drifting electrons. This is the case when [64]:

$$\frac{E_A}{E_B} > \frac{(1+x)}{(1-x)} \quad (2.20)$$

where E_B and E_A are the fields before and after the grid respectively, and $x = \frac{2\pi r}{R}$, where r is the wire radius and R is the distance between the wire centres. This equation is an approximation, since the grid is modelled as a wire plane.

In a gridded ionisation chamber, the signal comes only from the electrons, since the slower signal from positive ions induces charge only on the grid.

The maximum pulse amplitude in an ionisation chamber from the creation of n_0 electron-ion pairs is $V_{max} = \frac{n_0 e}{C}$. This typically produces small pulses, with the need for strong amplification.

2.3.2 Multiwire Proportional Counters

Wire proportional counters have the advantage over ionisation chambers in that the signals induced come not only from the initial charge deposited, but also from charge multiplication around the wires.

The electric fields at position r around a single wire, surrounded by a cylindrical cathode are given by the following equation [63]:

$$E(r) = \frac{V}{r \ln(\frac{b}{a})}, \quad (2.21)$$

where V is the voltage between the anode and cathode, a is the anode wire radius, and b is the cathode inner radius.

The electric fields in the immediate vicinity of the wire are very strong, where r is small. The electrons are drifted towards the wire anode, and are accelerated in the electric field. A single ionisation electron will collide with many molecules of the detector medium, and transfer energy in the collision. As the kinetic energy of the ionisation electron increases, due to acceleration in the electric field, the amount of energy transferred in a collision will exceed the energy needed to liberate an electron, and will cause secondary ionisation in the medium. All ionisation electrons continue to accelerate towards the wire plane anode, creating further secondary ionisation in an avalanche process.

The radius at which avalanching occurs is a function of electric field strength, as well as the detector medium, and therefore position-independence in the detector can be achieved by using an E field that confines the amplification to the region immediately surrounding the wire.

A multiwire proportional counter (MWPC) is a plane composed of wire proportional counters. The avalanches form identically to the single wire case, but the electric fields surrounding the wires differ, as shown in figure 2.8. For a plane of wires with separation distance of $2r$, the distance r in the direction perpendicular to the wire plane has non uniform fields. Most of the volume away from the grid has nearly uniform electric fields.

2.3.3 Time Projection Chambers

Time projection chambers [62] are drift chambers capable of three dimensional tracking of charged particles. There is an electric field across the main detector volume, drifting ionisation charge towards a readout plane anode, as shown in figure 2.9. The 3D track is reconstructed from the position and time of arrival of the electrons at the readout plane.

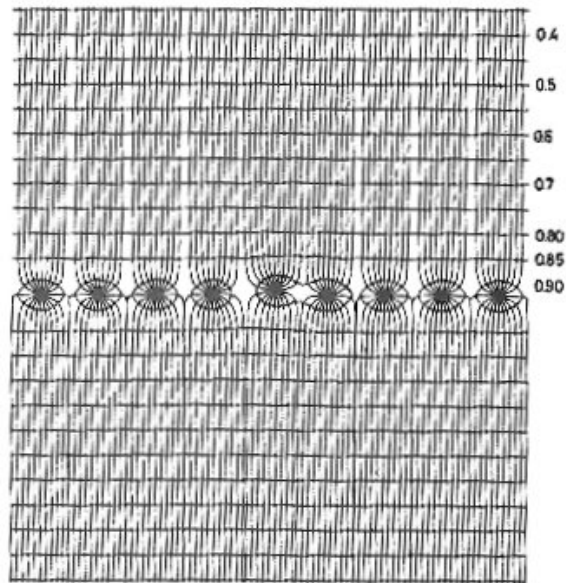


Figure 2.8: A plot of the electric field lines created by a MWPC: a grid of anode wires (perpendicular to the page) equidistant between two parallel cathode plates at the top and bottom of the figure. From [63]

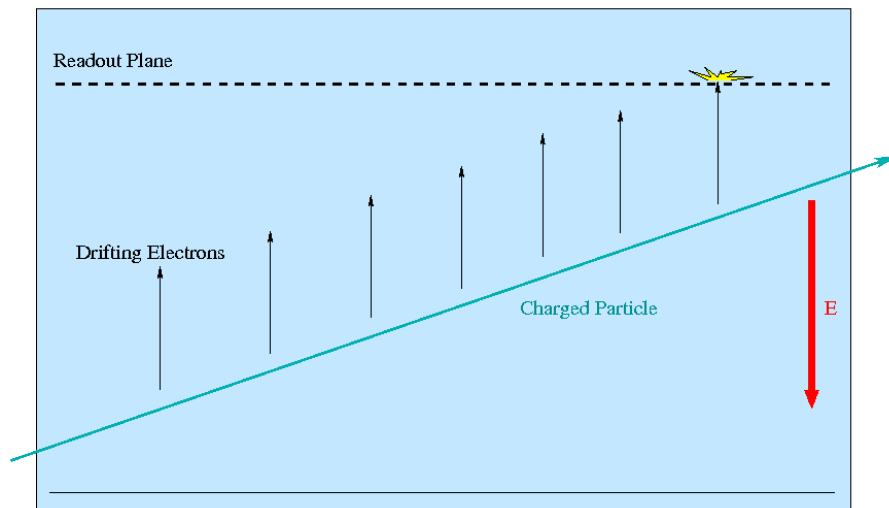


Figure 2.9: Schematic of a time projection chamber. Ionisation electrons from an incident charged particle are drifted to a wire readout plane.

Readout planes for TPCs vary from the traditional wire planes to micropattern gas detectors (see section 2.3.4) and optical readout.

The resolution of the time of arrival is dependent on the signal sampling rate at the readout plane. The primary limitation on the position resolution is the diffusion of the drifted charge. TPCs typically have much larger drift distances than ionisation chambers, or MWPC. Transverse diffusion of the drifting electrons will affect their position measured at the readout plane, and the longitudinal diffusion will affect the time at which they are measured. Since the path of the ionising particle is determined by the drifting electrons, the uncertainty on the measurement increases with diffusion, limiting the resolution. The longer the drift length, the larger the diffusion, and corresponding uncertainty on the measurement.

2.3.4 Thick Gas Electron Multipliers

The THick Gas Electron Multiplier (THGEM) [65],[66], is a robustly-made gaseous electron multiplier with single electron sensitivity, and gain of up to 10^4 . They are part of the class of micropattern gas detectors, commonly used as readout planes in gas TPCs.

The THGEM is manufactured by mechanically drilling holes through printed circuit board (PCB) with copper cladding on both faces. The standard scale of the THGEM varies between a PCB thickness of 0.4 mm and 1.6 mm, with holes of diameter of the same length scale, spaced by fractions of a millimetre. The THGEM holes can be further shaped by etching away a small amount of copper, to smooth any irregularities created by the drilling process.

An electric potential is applied across the copper electrodes of the THGEM, which creates a strong dipole electric field within the holes, and also protruding into the adjacent volume (see figure 2.10). Ionisation electrons drifted towards the THGEM are focused into the holes due to the shape of the electric field.

When operating the THGEM in gas, the electric field within the holes causes rapid acceleration, (hence energy gain) of an ionisation electron entering the hole. As the electron scatters off gas molecules in the THGEM hole, it deposits energy, causing ionisation. Each subsequent ionisation electron is accelerated by the fields in the THGEM hole, and the electric field is chosen such that on average, the energy gained is greater than the ionisation energy of the gas. Typically fields in argon gas are of the order of 2 kVmm^{-1} , for an ionisation energy of 26.4 eV [67]. Further scattering leads to a gas avalanche process, thus the THGEM acts as a charge amplifier.

THGEMs are very versatile devices since their behaviour can be application-

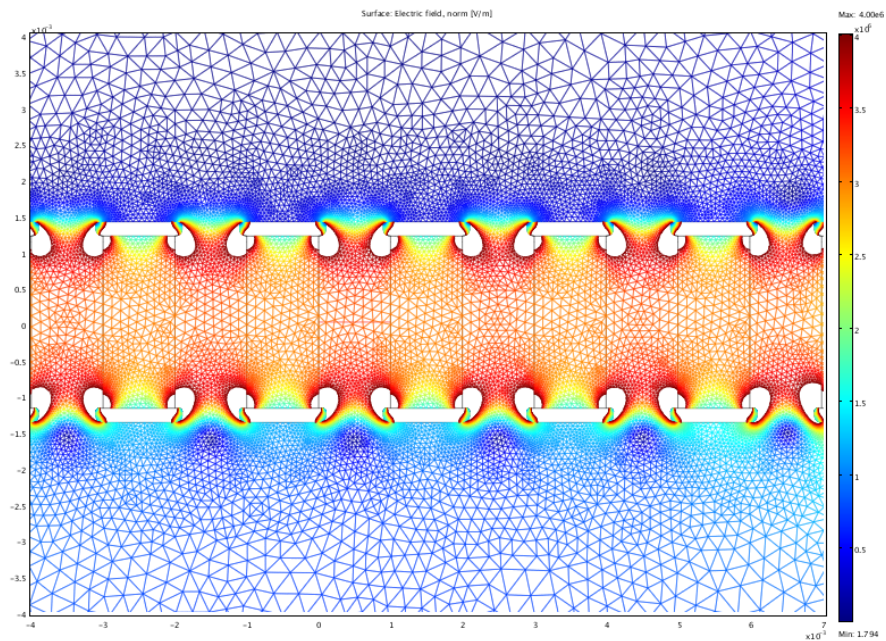


Figure 2.10: A finite element calculation image created using COMSOL, showing the electric field strength surrounding a THGEM, for a cross-section taken through a row of THGEM holes. The colour scale on the right hand side goes from a minimum of 1.8×10^6 to $4 \times 10^6 \text{ Vm}^{-1}$. The uncoloured areas around the corners of the THGEM are areas where the fields are higher than the scale.

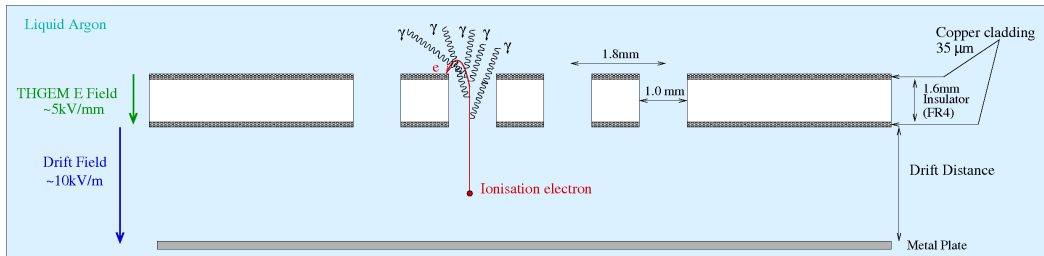


Figure 2.11: A schematic diagram of how a THGEM works in liquid argon.

tailored, choosing appropriate dimensions, operating gas, and pressure to fit purpose. Layers of THGEMs can be cascaded to produce higher gains (up to 10^7 with double THGEM).

A recent investigation [68] has demonstrated the proof of principle for operating a THGEM in liquid argon. As in gas, an electric potential is applied across the copper electrodes of the THGEM, creating a dipole electric field in the holes.

Inside the THGEM holes, the electrons are accelerated by the THGEM electric field, but since the mean free path of electrons in liquid argon is 0.86 nm [69], much shorter than the mean free path in argon gas, the average amount of energy gained by an ionisation electron before it scatters off an argon atom is <23.4 eV [67], which is insufficient to cause ionisation.

The tail-end of the electron energy distribution is greater than 11.55 eV [69], the excitation threshold energy of liquid argon, hence there is a finite probability that there will be excitation, and subsequent photon emission. This provides the possibility for an optical readout, as illustrated in figure 2.11.

2.3.5 Preamplifiers

The raw signal output from a detector is often small, and not impedance-matched to the readout device. The first stage after output from the detector is therefore often an amplification stage, called a preamplifier (or “preamp”). The preamplifier is located as close as possible to the detector, to maximise the signal to noise ratio. The output of the preamp is designed such that it has a low impedance, and is capable of driving the signal the longer distance to the next stage of pulse processing or recording without losses due to the capacitance of a long cable [63].

There are three main categories of preamp: charge amplifiers, current amplifiers, and voltage amplifiers. They take the same input pulse, amplify and shape it according to their characteristics.

Current and voltage amplifiers have the same basic circuit [70], shown in

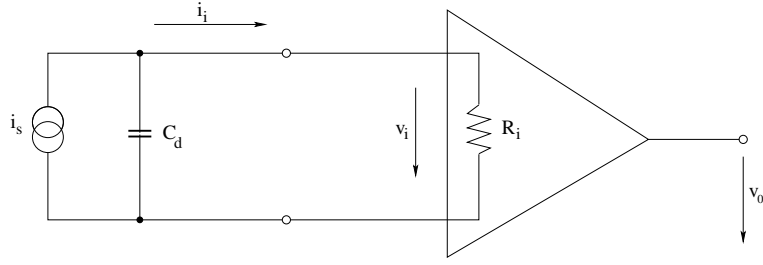


Figure 2.12: Circuit diagram for a current or voltage sensitive preamplifier, copied from [70]. C_d is the detector capacitance, i_s is the current source (i.e. the detector), v_i is the input voltage pulse, R_i is the amplifier input resistance, and v_o is the amplifier output.

figure 2.12. The mode of operation differs based on the ratio of amplifier input parameters to the charge collection time of the detector. For an input current pulse of magnitude i_s and duration t_c , the signal charge is $Q_s = \int i_s(t)dt = i_s t_c$. Whether the preamplifier operates in current mode or voltage mode depends on the time constant, t_c of the detector, and the input time constant $R_i C_d$, where R_i is the amplifier input resistance, and C_d is the detector capacitance.

For a time constant $R_i C_d \ll t_c$, the preamplifier operates in current mode, since the preamplifier capacitance discharges more rapidly than the charge arrives. The output voltage v_o is therefore proportional to the instantaneous current $i_s(t)$.

For a time constant $R_i C_d \gg t_c$, the preamplifier operates in voltage mode, where the signal current is integrated as the capacitor charges, before discharging, since the preamplifier capacitance discharges slowly. The output voltage $v_o = \frac{Q_s}{C_d} \exp \frac{-t}{R_i C_d}$ is proportional to the integral of $i_s(t)$.

A charge sensitive preamplifier [70] is also known as a “feedback” amplifier, since the signal amplification comes from the voltage across a feedback capacitor (shown as C_f in figure 2.13). An input pulse Q_i induces a voltage v_i , which is inverted and amplified by the preamplifier: $v_o = -A v_i$. The voltage is integrated by the preamplifier as the capacitor is charged, thus the output voltage is proportional to the integral of the input pulse.

The preamplifier types discussed all fulfil the same function, although it is necessary to know which mode the preamplifier is being operated in, since the parameters of the output pulses correspond to different things dependent on the preamplifier type. For example, the total amount of charge collected by a current preamplifier is the integral of the pulse, whereas for a charge or voltage preamp, the maximum amplitude of the pulse is proportional to the charge collected.

For ease of reference in the rest of the thesis, I will refer to these as preampli-

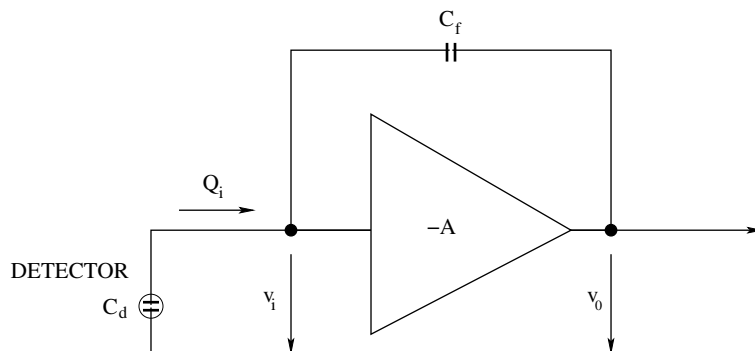


Figure 2.13: Diagram of a charge sensitive “feedback” amplifier copied from [70]. C_d is the capacitance of the detector, C_f is the feedback capacitor, v_i is the input signal voltage, and v_o is the amplified signal output.

fiers type 1,2,3 for current, voltage and charge sensitive preamplifiers respectively, as described above.

2.4 Charge Transport in Liquids

This section gives both the historical and theoretical background to charge transport in liquids, as well as an overview of the organic liquid scintillators used in the experiments in this thesis.

2.4.1 Theory of Charge Transport in Liquids

Charge transport in liquids is a phenomenon which cannot be definitively described by one single theory. When moving through a liquid, charges exhibit properties analogous to aspects of their motion in both gases and solids. Over a short range (roughly 2 orders of magnitude larger than the molecule size), the liquids have a conduction band, identical to that observed in solids, whereas across longer distances, charges move more similarly to in a gas, colliding and scattering off liquid molecules [71].

An electron moving in gas can be thought of as a particle in a vacuum, occasionally colliding with other gas particles. As the density of gas increases, the number of collisions does likewise. Naively, the liquid can be thought of as a very dense gas with a much shorter mean free path.

The ability to transport charge is due to the mobility of the electrons in the medium. The mobility (μ) of electrons with velocity \mathbf{v} in an electric field \mathbf{E} is

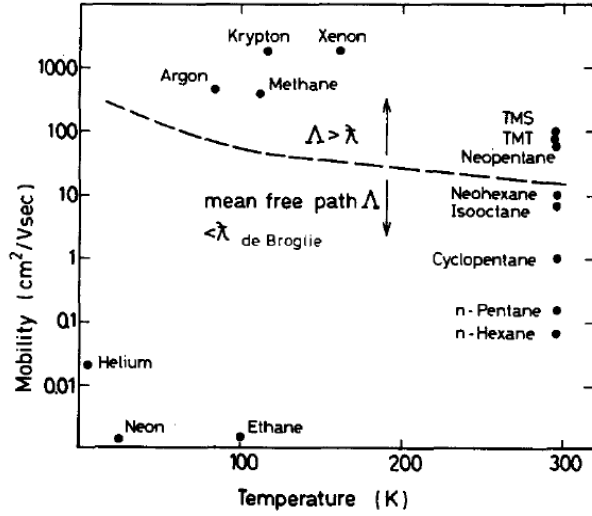


Figure 2.14: Mobilities of various liquids, from [72]. The dashed line separates liquids with a mean free path Λ above and below the de Broglie λ wavelength of thermalised electrons.

defined as follows (p33,[67]):

$$\mu = \frac{v}{E}. \quad (2.22)$$

High mobility is a necessary condition for a medium to transport charge well. The heavier noble liquids have what are considered to be high mobilities, whereas there is a large spread of mobilities in the room temperature liquids, as shown in figure 2.14. Possible reasons for this will be discussed in section 2.4.2.

A suggested condition [72] for electrons to move freely in a liquid is that the mean free path Λ , is greater than the de Broglie wavelength λ of thermalised electrons. In figure 2.14, copied from [72], the line for which the de Broglie wavelength is equal to the mean free path has been plotted as a dashed line, using the relationship between de Broglie wavelength and mobility presented in [73]. Above the line, it is expected that free electrons are present, whereas below it, the electrons should be bound in localised states, which means they can only move slowly.

For a liquid to be able to transport charge well, in the context of a detector medium, there are other important characteristics besides the mobility to be considered.

When drifting charge over a long distance, as is necessary in large volume detectors, it is necessary to consider the rate of diffusion. If diffusion in a liquid is large, the accuracy to which the original position of radiation deposition can be determined decreases. It is therefore preferable to have a liquid which has low

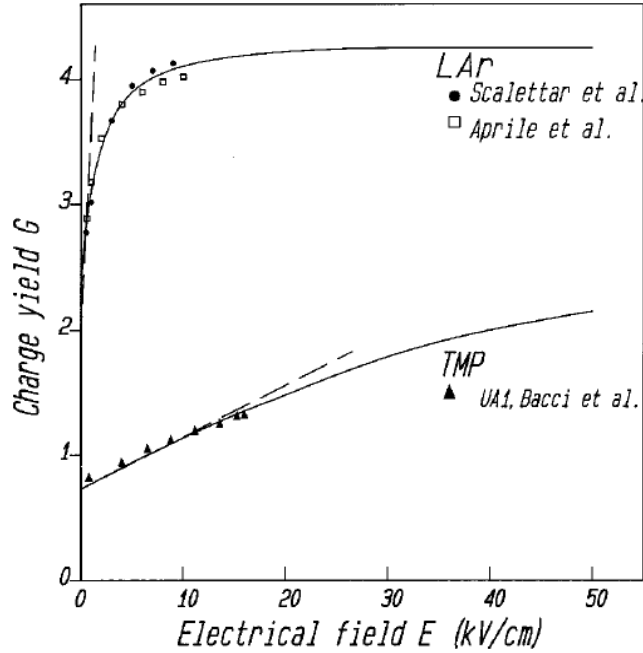


Figure 2.15: The charge yield of tetramethylpentane (TMP), a room temperature liquid and liquid argon (LAr) as a function of electric field, from [74].

diffusion.

Another important characteristic to consider is the number of electron-hole pairs created per unit energy. The W value, or activation energy, is the amount of energy needed to create a single electron-hole pair, and G is the number of electron-hole pairs created with 100 eV , so $W = \frac{100}{G} \text{ eV}$.

The detector signal is determined by the initial number of ionisation electrons created by the deposition of energy in the detector. A higher charge yield therefore increases the sensitivity of the detector. In liquids the electrons ejected from the molecules are much more efficiently thermalised by inelastic scattering than in gases, due to the difference in mean free path. In room temperature liquids the thermalisation times are very short, leading to considerably lower charge yields than in liquid argon for example, as illustrated in figure 2.15.

The ability to transport charge in liquids has been shown [74],[67] to be significantly affected by the presence of impurities in the detector volume. Both in cryogenic liquids, and those at room temperature, impurities of the order of 1 part per million (ppm) can significantly affect the charge transport properties. The electron lifetime will decrease, thereby decreasing the maximum drift length.

Any collision between a drifting electron and electronegative impurity could

lead to trapping of the electron in one of the following ways, where e is the electron, AB is an atom or molecule of impurity, X is a detector atom or molecule, $*$ represents an excited state (p52,[67]).

Radiative attachment:



Dissociative attachment:



Three body attachment (a two stage process):



As well as the electron lifetime, mobility will decrease with the presence of impurities, since some impurity compounds will trap and then detach from the drifting electron, thus increasing drift time [74], for example 1 ppm CO_2 in Tetramethyl silane (TMS) reduces the mobility by roughly a third.

In liquid argon, oxygen has been shown to be the impurity which most affects trapping (p53, [67]). The electron lifetime, τ is given approximately by the following equation (where O_2 is the amount of oxygen impurity)[68]:

$$\tau \approx \frac{300 \mu s}{O_2(ppb)}. \quad (2.27)$$

This means that it would be necessary to have impurities of less than 9 ppb to transport charge over a distance of 10 cm in liquid argon, assuming a drift velocity of $3 \text{ mm } \mu s^{-1}$.

2.4.2 History of Charge Transport in Room Temperature Liquids

Free charge in dielectric liquids first became a topic of interest in the late '60s, when measurements were made of parameters such as the ion electron pair creation energy (W), and the mobility in a wide variety of hydrocarbon-based dielectric liquids [75],[76],[77]. At a similar time, these parameters were being measured in liquid noble gases [67], and there was both experimental and theoretical work going on to try and identify patterns in the widely varying results in different liquids.

The mobility of spherical molecules such as tetramethylsilane (TMS) and

Table 2.4: Charge transport properties for a selection of liquids, extracted from [79] and [67]

Liquid	T (K)	μ ($\text{cm}^2\text{V}^{-1}\text{s}^{-1}$)	W (eV)
Argon	85	625	23.6
Krypton	117	1200	20.5
Xenon	220	8500	16.4
Neopentane	295	65.5	116
Tetramethylsilane	295	99	135
Tetramethylgermane	295	90	159
Tetramethyltin	295	70	161
n-Butane	296	0.4	526
n-Pentane	296	0.16	667
n-Hexane	296	0.09	769
n-Octane	296	0.04	833
n-Decane	296	0.038	833
2,2,4,4 Tetramethylpentane	296	29	120
Cyclopentane	296	1.1	667

neopentane were found to be the highest, with the properties of the liquid changing as a function of molecule length [78]. The mobility and activation energy were shown empirically to be linked to the number of carbon-hydrogen bonds in the molecular chain, with the mobility decreasing, and activation energy increasing with the length of chain. Table 2.4 shows the properties of a selection of liquids, extracted from [79].

It was not until 1983 that room temperature liquids were first used for particle detection, when Engler and Keim built an ionisation chamber using TMS [72], and measured cosmic ray muons. Tetramethylsilane, and tetramethylpentane (TMP) are two of the liquids with highest mobility, making them very attractive detector media. Their charge transport properties were characterised in some detail with a view to use in large volume calorimetry [80]. In 1990 the UA1 hadronic calorimeter was built: a TMP ionisation chamber.

Since then, room temperature liquids have not been in widespread use in drift chambers, but are still being developed for use in medical physics applications [81].

Dark Current

From before the time of the observation of free charge in room temperature liquids, there have been theories suggesting that dielectric liquids will become conductors at a sufficiently high electric field. Reference [82] suggests that dielectrics with low conductivity are merely special cases in a general class of weak electrolytes, thereby

creating a unified picture of conductivity in all dielectric liquids. This would give rise to a leakage current inherent in the liquid, analogous to the dark current in semiconductor detectors.

The mechanism for this process is molecular dissociation. Molecular dissociation [71] is the separation of molecules with zero net charge into free ions. In the presence of an electric field, the ion pair can be separated, but when the surrounding liquid is non-polar they are brought back together by the coulomb force. If there are polar impurities in the liquid, they act as surfactants, causing the ion pairs to remain separated. Ion pairs are more easily separated as the electric field increases, which is why molecular dissociation only happens in the presence of high electric fields.

The evidence suggests multiple causes for the background current in dielectric liquids [83]. As well as molecular dissociation, the background current is also caused by the presence of impurities in the liquid [84],[85]. Any charged molecules, electronegative impurities for example, will travel in a strong electric field, and therefore induce a current. The amount of charge transport in the liquid due to impurities will decrease over time, as the detector cleans itself.

In [84], the background current is described by the following equation:

$$i_f = \frac{i_0}{1 + bt} + C \exp(h\sqrt{E}) \quad (2.28)$$

where i_f is the background current, i_0 is the initial current, E is the electric field, t is time, and $h = \frac{2e^{\frac{3}{2}}}{kT\epsilon^{\frac{1}{2}}}$, where e is the charge of an electron, k is the Boltzmann constant, T is temperature, and ϵ the dielectric constant of the material. The first term in the equation represents the contribution from impurities present in the liquid. The constant b has been evaluated as a first approximation by fitting data empirically. The second part of the equation represents the molecular dissociation, which depends on the liquid. C is a temperature-dependent quantity, which is proportional to the number of dissociated molecules at zero electric field.

Figure 2.16 taken from [84] shows how the background current between two electrodes with 1mm spacing in n-heptane, a room temperature liquid hydrocarbon varies over time, at an electric field of 20kV/cm.

There are other theories [81] such as the bubble effect, which suggest that surface imperfections on the electrodes cause a localised higher electric field, which leads to the formation of “streamers” or vapour bubbles, and hence localised charge multiplication will take place. This is similar to molecular dissociation in that it would occur at a constant rate over time. There is evidence, however, to suggest that

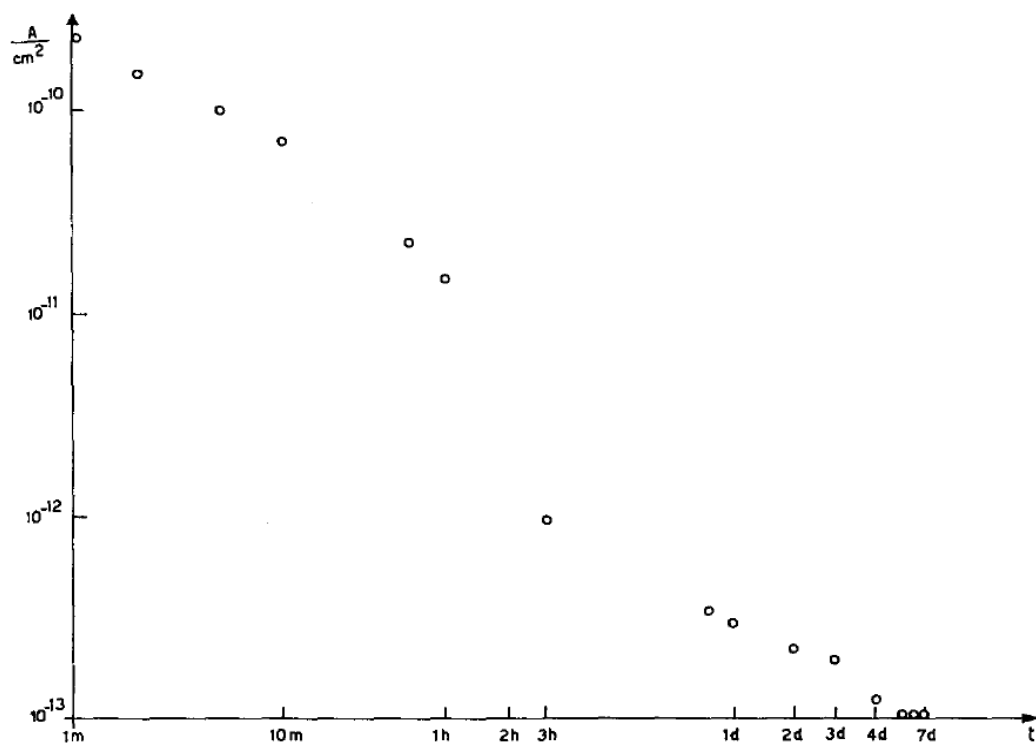


Figure 2.16: Background current density as a function of time in n-heptane, taken from [84].

these imperfections are causing avalanches in the liquid phase rather than the gas phase, since the rate of the threshold electric field for this process has been measured to be pressure independent [86]. In summary, the three hypothesised contributions to the background current come from the molecular dissociation, impurities - decreasing over time, and streamers - produced in extreme field regions.

2.4.3 Organic Liquid Scintillators and Solvents

The process of scintillation occurs when ionising radiation is incident on a scintillating material, depositing energy which causes the material to fluoresce. This fluorescence is caused by the transitions between energy levels of electrons in molecules of the scintillating material. A good scintillator is one that converts a large fraction of the energy deposited into prompt fluorescence.

Scintillators are widely used for radiation detection, and liquid scintillators are particularly used in the life sciences, since they can be mixed with other fluids for detection. Over the past 25 years there have been many scintillation fluids developed for use in the life sciences. These liquids are known as “safe” solvents by many, since they have low toxicity, low vapour pressure, and a high flash point. This contrasts strongly with the liquids discussed in section 2.4.2, and with other organic liquid scintillators such as xylene, toluene and pseudocumene (p657,[87]). The “safe” scintillator cocktails consist of a hydrocarbon solvent, and wavelength shifting fluors. The solvents themselves emit ultraviolet (UV) light, and are transparent to some of their own emitted wavelengths. The UV light is Stokes shifted into the visible light range by the fluors, making the light easier to detect, as well as improving the efficiency.

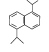
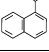
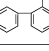

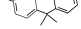
The organic solvents which were studied in this thesis are presented in table 2.5.

Linear alkyl benzene (LAB)

Linear alkyl benzene is the solvent which is most widely used in particle physics for scintillation counting. The detectors in reactor neutrino experiments Daya Bay [88], and RENO [89] both use Gadolinium doped LAB as the active medium for scintillation counting. The SNO+ double beta decay experiment also uses a LAB based detector.

Due to its widespread use, the optical properties of LAB have been well characterised, its purification investigated and the choice of fluors optimised [90]. Its properties are often compared with Pseudocumene (PC), previously the most

Table 2.5: The organic liquids and solvents tested and their molecular structure.

Chemical name	Chemical Formula	Molecule structure
Di isopropyl naphthalene (DIN)	$C_{16}H_{20}$	
Mono isopropyl naphthalene (MIPN)	$C_{16}H_{14}$	
Mono isopropyl biphenyl (MIBP)	$C_{15}H_{16}$	
Linear alkyl benzene (LAB)	$C_6H_5C_{10}H_{21}$ to $C_{13}H_{27}$	
Phenyl xylyl ethane (PXE)	$C_{16}H_{18}$	

commonly used liquid scintillator. The optical properties are similar, but the low flash point of PC makes LAB a better choice with respect to health and safety.

Phenyl xylyl ethane (PXE)

Phenyl xylyl ethane has also been well characterised, despite being less widely used than LAB. It is used in the Double Chooz experiment [91], but was also a strong candidate for use in Borexino [92]. The optical properties, purification methods and compatible fluors have therefore been investigated.

Di isopropyl naphthalene (DIN)

Di isopropyl naphthalene was a solvent which was created in 1985 for use in scintillation counting [93]. It was shown to perform well in comparison to PC optically, and better with respect to permeation into plastics and of course, safety.

DIN has thus far not been used as the active medium for a neutrino detector, but nevertheless, it has been investigated alongside the previous two liquids [94].

Mono isopropyl naphthalene (MIPN) and Mono isopropyl biphenyl (MIBP)

These liquids have no previous history of being used as solvents for liquid scintillator cocktails, however as they have a similar molecular structure to DIN, they were investigated in this thesis.

2.4.4 Liquid Argon

Liquid argon is a heavy noble gas, and therefore has a high stopping power, and a good radiation absorption cross-section [67],[63]. Along with other noble liquids, Ne, Xe, Kr, this makes it an ideal material for a detector. Argon is the least expensive, most abundant noble gas, as it is produced as a by-product of industry, and also makes up nearly 1% of air. This makes it a good choice for the active medium for large volume detectors.

Energy absorbed from incident radiation causes either scintillation light, or ionisation. The average energy needed for scintillation light in liquid argon is 19.5 eV (p16,[67]), and for ionisation is 23.6 eV (p16,[67]).

In noble liquids about 60% of the energy absorbed is converted to ionisation. In the absence of an electric field, all of these electron-ion pairs will eventually recombine to generate scintillation light, but in an electric field, only a small amount of recombination will take place. According to the Jaffe model of recombination, the charge yield, Q is given by the following equation (p19,[67]):

$$Q = \frac{Q_0}{1 + K/E} \quad (2.29)$$

where Q_0 is the total ionisation charge, E the electric field strength and K the recombination coefficient, 0.03 kVcm^{-1} (p22,[67]) for liquid argon. The rate of recombination is increased by the presence of impurities as discussed in section 2.4.1, since the recombination coefficients for non-noble gases are considerably larger.

The energy deposited along the tracks is proportional to the energy of the emission photons and electrons, therefore $\frac{dE}{dx}$ measurements contribute to particle identification.

Liquid argon is commonly used for calorimetry, for example in the ATLAS experiment [95]. In addition to the charge collection, the light emitted can also be used to determine spatial coordinates in the detector volume, or as a trigger for experiments using charge readout for tracking (such as TPCs).

As shown in figure 2.14, liquid argon has a high mobility, and free electrons.

Since liquid argon is both a scintillator and a medium capable of transporting charge, one can build a liquid argon detector which collects both ionisation electrons, and emission photons from deposited energy. The anti-correlation between the two signals gives excellent energy resolution. In addition, a TPC can use the initial photons for event triggering, as well as the possibility of using secondary scintillation as a readout option [68]. Its current drawbacks are the purification process, and the necessity for cryogenic infrastructure.

2.5 A Room Temperature Liquid Time Projection Chamber

The aim of this thesis is to find a room temperature liquid which both transports charge, and is a scintillator. The effectiveness of a detector with such properties was discussed above, in section 2.4.4.

The initial focusing point was on dielectric liquids used for scintillation counting, namely the organic liquid scintillators discussed in section 2.4.3, and the investigation of their charge transport properties. These liquids offer advantages both in their cost-effectiveness and their low toxicity.

Subsequently, the optical properties of room temperature liquids with a proven record of good transport properties were investigated. These liquids have the disadvantage of being somewhat more dangerous to work with.

The motivations behind looking for such a candidate liquid are to give the possibility of creating a detector analogous to a liquid argon time projection chamber, but at room temperature.

As a liquid-based TPC, this type of detector would be ideal for rare event physics, both as a large volume far detector for long baseline neutrino physics, but also for double beta decay. There is a precedence for isotope loading in liquid scintillators, and the scalability of this detector, combined with the charge and light readout would make this a very attractive detector for the field.

Despite the challenges encountered in this thesis, it is clear that there remains a strong motivation for investigating the charge transport and optical properties of room temperature liquids, with a view to finding a suitable candidate detector medium.

Chapter 3

Detector Design and Construction

In order to investigate the charge transport and optical properties of room temperature liquids, several small volume detectors were designed, built and commissioned. This chapter describes each detector setup in detail, along with its purpose, and relates the detectors to the data in chapter 4. The physics details of how the detector types work have been covered in section 2.3, so will not be repeated here.

3.1 Radioactive Sources summary

There were a number of radioactive sources used with the detectors, this section provides an overview of their properties, for reference. The radioactive sources used are shown in table 3.1.

The americium source has the advantage of having a high activity, and a large deposition of energy by the alpha particles. The alpha particles are emitted from the americium at an energy of 5.4 MeV, but the americium is sealed with a thin layer of gold, therefore, the alpha particles emitted from the source are at the lower energy of 3.9 MeV. Unfortunately the amount of charge observed may be considerably lower than the emitted energy, since the alpha quenching factors of the liquids may be as high as 200, analogous to previously measured hydrocarbons ([79],p187). For this reason it is necessary to have other sources emitting non-quenched radiation types, in order to do an absolute calibration, and to measure the alpha quenching.

The thorium source emits also predominantly alpha particles, but has a very low event rate, which means that it can be used in liquids with a slow drift time with minimal pulse-pileup. It also has beta daughters, which contribute to the energy

spectrum, and because of the alpha quenching, the alpha peak is reduced to the point where this source becomes less useful as a calibration source. The source is of unknown age, and from the spectra analysed in section 4.1.2, it is believed to be not in equilibrium. The equilibrium is broken after the initial thorium decay. The entire decay chain of thorium 232 is shown in table 3.2. From this decay chain, the radiation most likely to be observed is included in table 3.1.

The lead 210 source is a beta emitter, with a beta spectrum endpoint energy of roughly an MeV. Since there is minimal beta quenching expected, this source has a larger effective energy deposition. It also has a low event rate, which minimises pileup.

Cosmic ray muons are an extremely useful calibration source. The majority of muons will pass vertically through the detector, giving a sharp peak at the energy corresponding to the depth of the liquid. The amount of energy deposited in each liquid has been calculated for the relative densities of the liquids, and is shown in table 4.1 in the results chapter.

Table 3.1: Summary of radioactive source properties

Source	Emitted particles	Energy	Activity
Americium 241	α	3.9 MeV	37 kBq
	γ	59.5 keV	
Thorium 232 (welding rod)	α	4.0 MeV	uncalibrated
	β	2.18 MeV	
	β	1.7 MeV	
Lead 210	β	1.11 MeV	370 Bq
	γ	46.5 keV	
Cosmic ray muons	β	2 MeVcm	$1 \text{ cm}^{-2} \text{ minute}^{-1}$

Table 3.2: The decay chain for thorium 232, extracted from [96]

Half lifetime	isotopes decay branch, %	α -decay energy, MeV (branch, %)	β -decay energy, MeV (branch, %)	γ -emiss. energy, keV (emiss. prob., %)
1.405×10^{10} y	$^{232}_{90}\text{Th}$ 100 $\downarrow \alpha$	α : 4.012 (77.9) α : 3.954 (22.1)		γ : 63.81 (0.27)
5.75y	$^{228}_{88}\text{Ra}$ 100 $\downarrow \beta$		β : 0.039 (60) β : 0.015 (40)	
6.15h	$^{228}_{89}\text{Ac}$ 100 $\downarrow \beta$		β : 2.18 (10) β : 1.70 (11.6) β : 1.11 (31.0)	γ : 338.32 (11.3) γ : 968.97 (16.2) γ : 911.21 (26.6)
1.913y	$^{228}_{90}\text{Th}$ 100 $\downarrow \alpha$	α : 5.423 (71.1) α : 5.340 (28.2) α : 5.221 (0.44)		γ : 84.37 (1.22) γ : 215.99 (0.28)
3.664d	$^{224}_{88}\text{Ra}$ 100 $\downarrow \alpha$	α : 5.685 (94.9) α : 5.449 (5.1)		γ : 240.99 (4.1)
55.6s	$^{220}_{86}\text{Rn}$ 100 $\downarrow \alpha$	α : 6.288 (99.9) α : 5.747 (0.11)		γ : 549.73 (0.11)
0.145s	$^{216}_{84}\text{Po}$ 100 $\downarrow \alpha$	α : 6.778 (100)		
10.64h	$^{212}_{82}\text{Pb}$ 100 $\downarrow \beta$		β : 0.569 (12) β : 0.331 (83) β : 0.159 (5)	γ : 300.09 (3.25) γ : 238.63 (43.5)
60.55	$^{212}_{83}\text{Bi}$ 35.94 $\alpha \swarrow$ 64.06 $\searrow \beta$	α : 6.089 (27.1) α : 6.050 (69.9)	β : 2.248 (86.6) β : 1.521 (6.8)	γ : 1620.74 (1.5) γ : 727.33 (6.7)
3.053 0.298 μ s	$^{208}_{81}\text{Tl}$ $^{212}_{84}\text{Po}$ $\beta \searrow$ $\swarrow \alpha$	α : 8.785 (100)	β : 1.80 (51) β : 1.52 (21.7) β : 1.29 (22.8) β : 1.52 (3.1)	γ : 583.19 (30.6) γ : 860.56 (4.5) γ : 510.77 (8.2) γ : 2614.53 (35.8)
stable	$^{208}_{82}\text{Pb}$			

3.2 Organic Liquids summary

The organic liquid scintillator cocktails and solvents used in this work are described here for reference. The scintillation cocktails are purchased as pre-mixed liquids, and there is limited information provided by the companies producing them about the wavelength-shifting fluors present in the cocktails. Where possible, the base solvents for these scintillation cocktails have been tested in addition to the cocktails, in order to test any effects due to the presence of the fluors. A list of the liquids used is shown in table 3.3.

Table 3.3: Summary of organic liquids

Liquid name	Organic solvent	Company [Reference]
Optifluor O	Linear alkyl benzene (LAB)	Perkin Elmer [97]
Ultima Gold F	Di isopropyl naphthalene (DIN)	Perkin Elmer [98]
Ecoscint O	Phenyl xylyl ethane (PXE)	National Diagnostics [99]
Di isopropyl naphthalene (DIN)		Fisher Scientific [100]
Phenyl xylyl ethane (PXE)		Dixie Chemicals [101]
Mono isopropyl naphthalene (MIPN)		Ruetgers [102]
Mono isopropyl biphenyl (MIBP)		Ruetgers [103]
Tetra methyl pentane (TMP)		Alfa Aesar [104]
Cyclopentane (C5)		Sigma-Aldrich [105]

3.3 Wire Proportional Counter

The purpose of this detector was to conduct preliminary investigations into a wide variety of organic liquid scintillators and solvents. This detector type was therefore chosen to maximise the possibility of detecting small amounts of moving charge in low mobility liquids.

A wire proportional counter (WPC) with a very small drift distance was implemented, giving high electric fields at moderate input voltage, with the possibility of charge multiplication at the anode wire. Avalanching around the anode wire gives a large signal from a small amount of charge collected, giving a better sensitivity than achievable in a drift chamber of the same size. The non-uniform geometry doesn't allow for precise measurement of charge transport properties, but

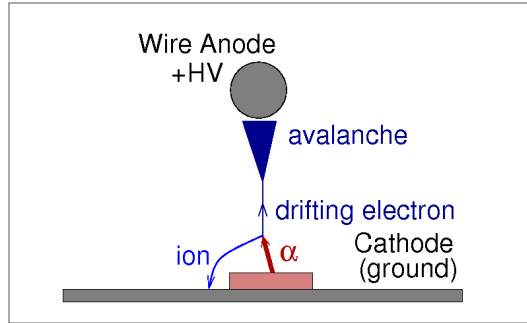


Figure 3.1: Schematic of the wire proportional counter.

allows to distinguish between liquids which show no signs of charge transport, and those which show promise.

This detector consisted of a single anode wire of diameter 0.4 mm mounted at a distance of 7 mm from a grounded cathode plane (see figure 3.1). The americium 241 alpha source was mounted at the cathode, and the charge read out from the anode wire. The energy spectrum in argon gas is shown in figure 3.2.

The detector chamber is 1 ℓ in volume, and the detector infrastructure is mounted on metal bars attached to the lid, with the high voltage anode wire well separated by insulating material. The detector chamber was custom-made in the Warwick Mechanics Workshop, and the electrical feedthroughs on the lid are Baseplate feedthroughs, from the Kurt J. Lesker Company. These are vacuum grade feedthroughs which are screw-connected to specially sized holes in the detector lid.

A positive high voltage was applied to the anode wire via a 10 M Ω bias resistor. The high voltage was input to the detector using an SHV feedthrough, from an SRS PS350 single channel power supply with maximum output of 5 kV.

The signal from the anode was first amplified and impedance-matched before leaving the detector via a BNC feedthrough. For this purpose a custom-made preamplifier was mounted inside the detector volume in close proximity to the anode wire. This high gain preamplifier with wide bandwidth input is necessary as the pulse shapes coming from charge transport in these liquids is completely unknown.

The preamplifier is a voltage-sensitive integrating preamplifier (type 2, as discussed in section 2.3.5), with a 100 MHz bandwidth input, and a gain of 200. The circuit diagram for this device is given in figure 3.3, and the calibration in figure 3.4. In order to prevent a high frequency feedback oscillation in the preamplifier, a damping resistor of 22 k Ω is attached at the input stage. The preamplifier is AC-coupled to the wire anode via a 1nF capacitor rated to 15 kV. This preamplifier requires ± 6.5 V power supply, which is supplied via a 4 channel power supply made

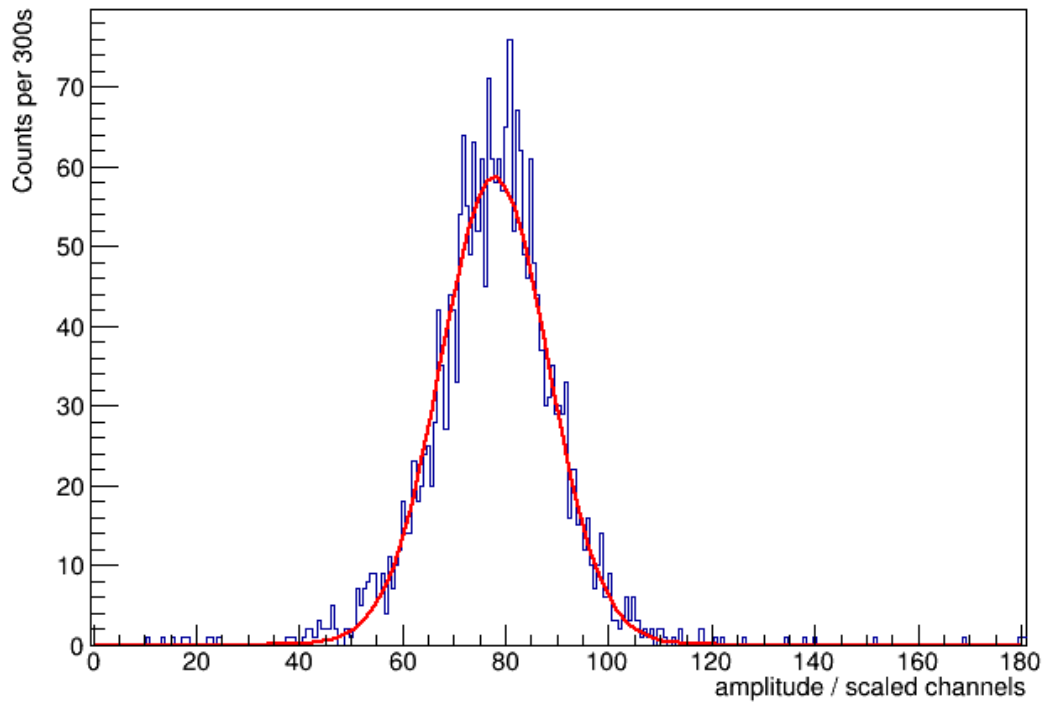


Figure 3.2: Americium 241 alpha spectrum in argon gas, taken using the Wire Proportional Counter with the source collimated and pointing along the direction of the wire. The red line shows a Gaussian fit, with mean value 77.7 ± 0.2 and standard deviation 10.3

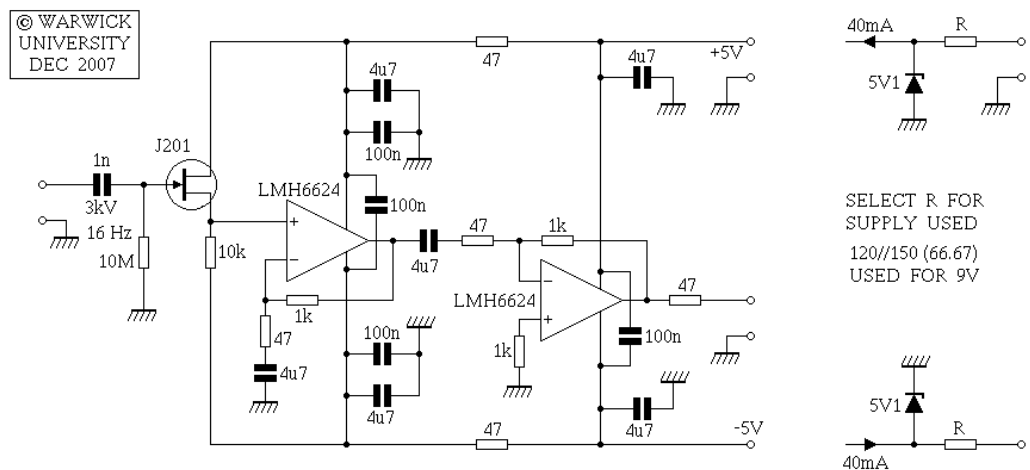


Figure 3.3: The initial circuit diagram for a custom-made voltage-sensitive pre-amplifier, (type 2, as discussed in section 2.3.5).

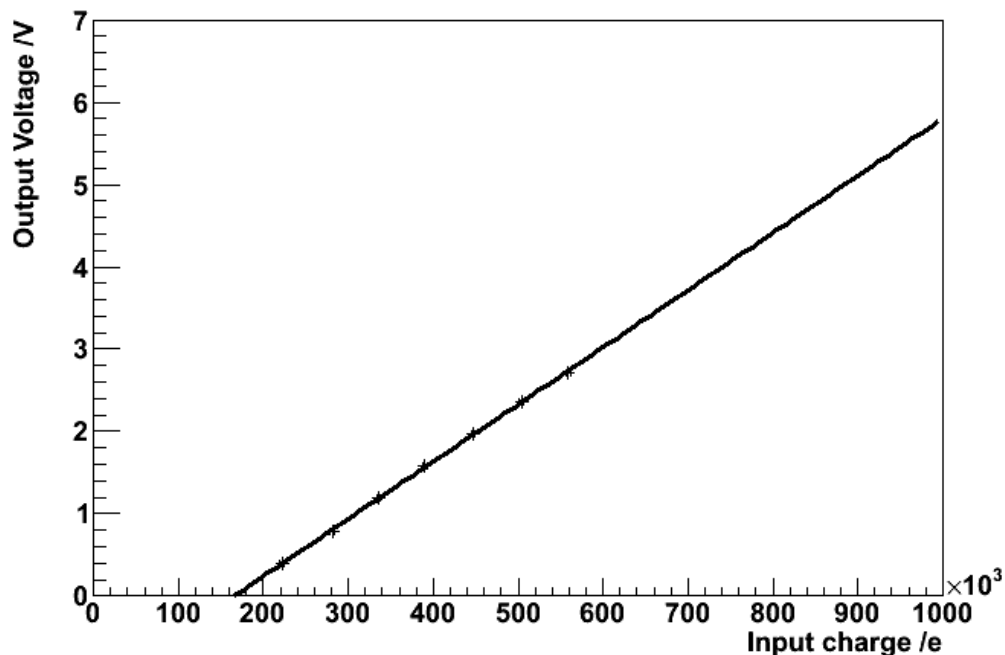


Figure 3.4: Calibration curve for voltage-sensitive preamplifiers, created by inputting delta pulses across a 1.6 pF capacitor.

by the Warwick Electronics Workshop. Initially, off-the-shelf DC power supplies were used, but the switch mode power supply unit within them created a large amount of noise at 50 Hz, necessitating the design and creation of a quieter power supply. The circuit diagram for the power supplies used is shown in figure 3.5.

Selected pulses from this detector are shown in figure 4.20 in section 4.2.1.

3.4 Gridded Ionisation Chamber

The purpose of this detector was to make more precise measurements of the liquids shown by the WPC to have signs of charge transport, whilst still using a fairly simple and well understood detector type. The uniform fields throughout make drift speed measurements in particular much more straightforward than in the single-wire geometry of the previous detector.

The detector consisted of an anode and cathode plate with a Frisch grid between them, as shown in figure 3.6.

A source was mounted at the cathode: both the Am 241 source, and the Th 232 source were used, since the two sources have vastly different activities, and it is useful to observe pulses with a smaller likelihood of pileup. Measurements were

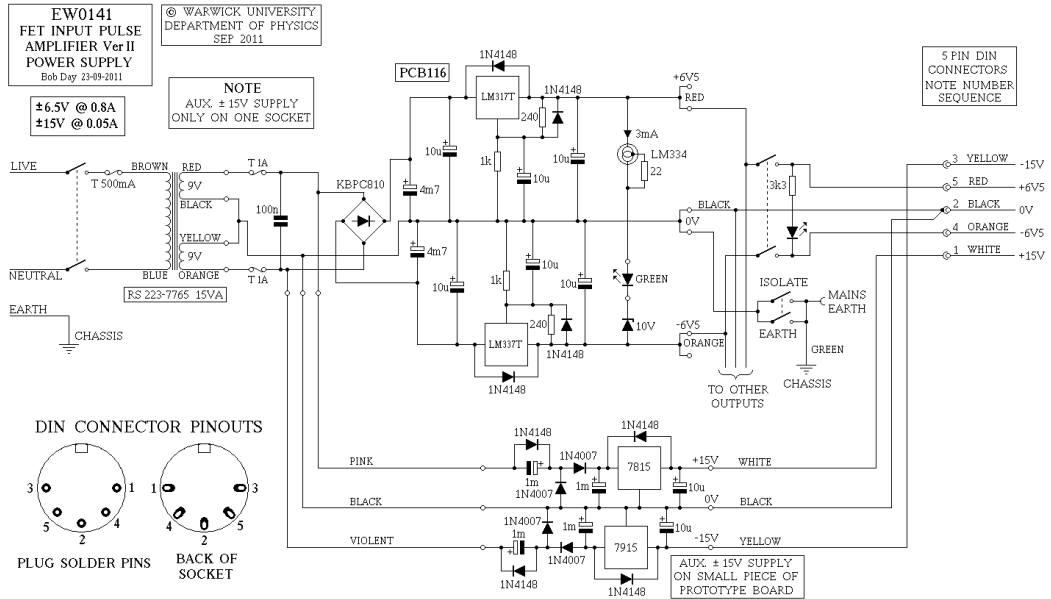


Figure 3.5: Circuit diagram for the 4 channel DC power supply which outputs $\pm 6.5\text{ V}$ on channels 1-3 and $\pm 15\text{ V}$ on channel 4.

taken in a selection of liquids as a function of drift voltage.

The initial setup of the detector had a drift distance of 22 mm, and the Frisch grid 7 mm from the readout anode. Positive high voltage was applied at the anode and split using a voltage divider, applying the high voltage to the plates in a ratio of 53:50, fulfilling formula 2.20 to keep the grid optically transparent to drifting electrons.

The detector chamber is 2.5 litres in volume, and was custom-made by the Warwick Mechanics Workshop. The chamber is not designed to be used in vacuum conditions, therefore the electrical feedthroughs are simply attached to the lid by screw connection. A schematic of the lid is shown in figure 3.7. The holes in the outermost section of the lid are for screw connection to the chamber, and the inner holes are for the threaded bars which hold the main detector infrastructure. Most of the connections on the lid are positioned peripherally to maximise distance from the high voltage plate inside the detector. The high voltage connectors are midway between the detector and the grounded outer detector, to prevent breakdown. The banana plugs and BNC connectors in the centre of the lid were initially intended for SiPM power input and signal output respectively, for devices mounted at the cathode. This was not implemented due to sparking from the high voltage planes to the grounded metal SiPM casing, although they are present in the photograph in figure 3.6. The gas inlet / outlet are 6 mm metal pipes, with a rigid plastic hose

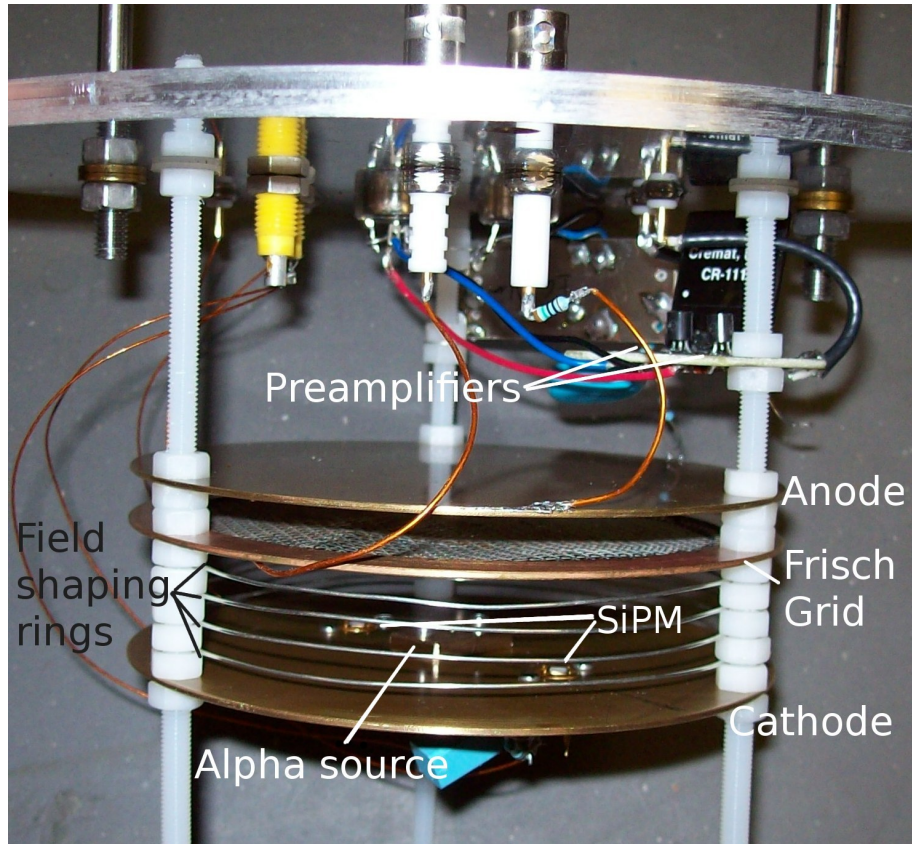


Figure 3.6: A photo of the gridded ionisation chamber in its initial configuration.

attached on the inside of the inlet. This was used for putting argon gas into the detector, as well as for cleaning the liquids by bubbling gas through them. The plastic hose takes the gas to the bottom of the detector, so that it passes through more of the liquid, giving a more uniform purity.

The voltage-sensitive preamplifier described in section 3.3 above was used for some of the measurements, AC-coupled to the anode, and a Cremat CR110 charge sensitive preamplifier (type 3, as discussed in section 2.3.5) mounted on a circuit based on the CR150 base board was also used, also AC-coupled to the anode (when in use). Using a combination of these two preamplifiers allowed for easier diagnosis of detector problems - coupling one of the preamps to the grid, for example, and the other to the anode, allowed to determine which pulse populations at the anode were capacitively induced from the grid, rather than drifting charges in the grid / anode section of the detector. The use of two different preamps also made it easier to diagnose problems with the preamplifiers themselves. The charge sensitive preamplifier, in some respects was more reliable than the voltage-sensitive device,

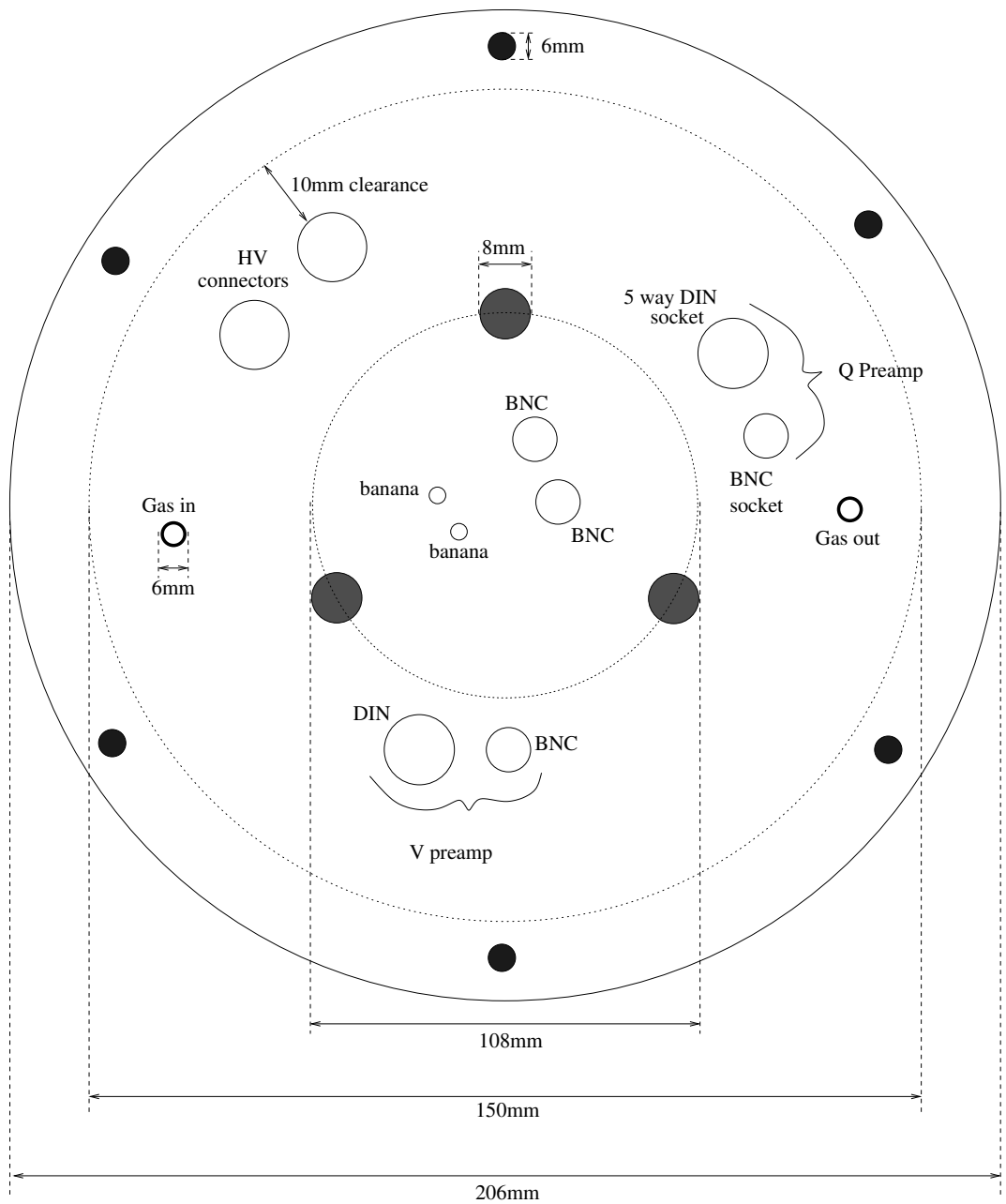


Figure 3.7: A schematic diagram of the view from above of the gridded ionisation chamber detector lid with all dimensions, holes, and connections. The high voltage connectors changed as the detector developed, and were variously SHV5 connectors, HV LEMO connectors, and simply holes with a cable and washer. This diagram is not to scale.

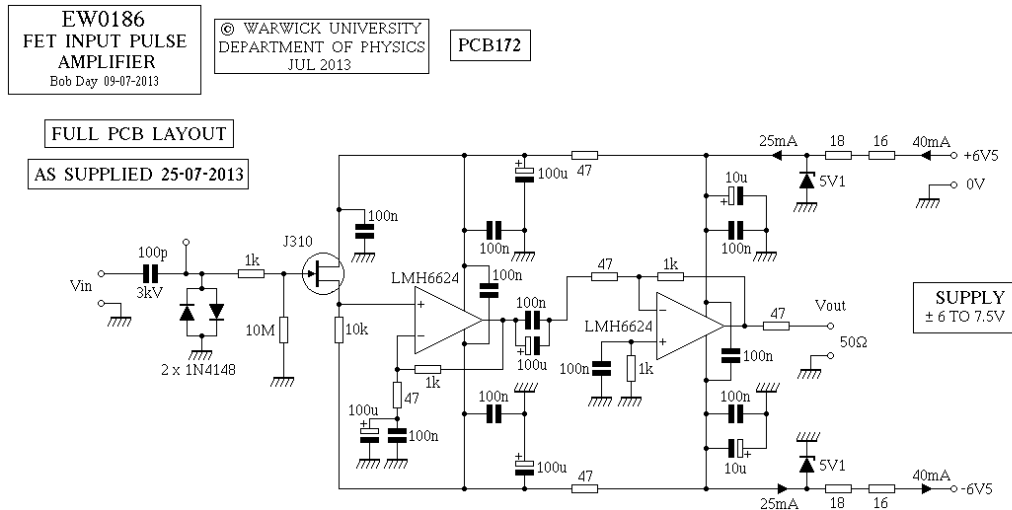


Figure 3.8: The circuit diagram for the modified voltage-sensitive preamplifier. This version has protection diodes on the input, and a longer time constant. For the original version see figure 3.3.

however it was more susceptible to damage. The response of the voltage-sensitive device to slow pulses (of the order of $500 \mu\text{s}$) initially gave a response pulse which was heavily altered by the time constant of the preamp, i.e. with a large negative under-swing following each pulse. This was identified as an electronics problem (rather than physics) by the features not being present using the other preamplifier. Since the voltage-sensitive preamplifiers are custom-made in the Warwick Electronics Workshop, it was possible to modify the electronics to accept a wider range of pulse risetimes. The modified circuit diagram is shown in figure 3.8.

The single high voltage channel comes from a 15 kV power supply, made by the Warwick Electronics Workshop. A low pass filter with a time constant of 1 s was attached to its output to damp the 50 Hz and 100 Hz oscillations from the power supply.

The detector is mounted on Delrin (polyoxymethylene) threaded bars, and was designed to have an extensible drift distance to allow an extended measurement programme. The detector was initially mounted on nylon threaded bars, but after lengthy exposure to the organic liquid scintillators, the properties of the nylon bars changed, and they were no longer stably insulating to high voltage. This meant they broke down under application of high voltage. Delrin was chosen for its strong resistance to permeability, and its stiffness for ease of machinability.

The electric field from grid to cathode is kept uniform by 4 field-shaping rings, made of 0.7 mm diameter wires, held at 5 mm separation by nuts on the threaded bars. They form part of the resistive divider, and are each separated by a $10\text{ M}\Omega$ resistor, each rated to 3 kV. This field cage was chosen for ease of manoeuvrability, allowing for alteration of the drift length.

The initial detector layout had the anode readout plane closest to the top of the chamber, close to both the high voltage input, and the preamplifiers, mounted near the signal feedthroughs. This meant the cathode was at the bottom of the detector, and extension of the drift distance could happen, up to a length of 10 cm, by removing the cathode plane, and adding more field-shaping rings, before replacing the cathode further down.

After the detector was rebuilt using Delrin, several earlier problems were addressed, and alternative possibilities explored by altering the detector layout. The decision was made to put the cathode at high voltage, and have the anode on a much less high positive high voltage, with a grounded grid. This minimised problems with breakdown of capacitors on the high voltage anode input. Since the capacitors were directly connected to the preamplifier, a tiny breakdown in any component was highly amplified, creating an undesirable background. The revised layout is shown in figure 3.9.

The revised setup necessitated two high voltage power supplies, but has the advantage of separating the two electric field variables, anode-grid and grid-cathode. This gives a lot more flexibility both for testing the detector and in the measurement programme. It enables testing of the detector sections separately, as well as the option to decrease the drift field whilst maintaining a constant anode-grid field for seeing pulses. The two high voltage power supplies for the detector necessitated two complete, independent current paths, which is why the grid and last field-shaping ring are both grounded, but not connected directly to one another. The static charge on each, caused by the electric fields to the anode and cathode are not equal, due to the differing field strengths, but with the grounded field-shaping ring close enough to the grid, the electric fields appear analogous to those in the voltage divider setup. The voltage ratios necessary to keep the grid optically transparent to drifting electrons were calculated using formula 2.20. The anode voltage relative to cathode voltage is kept at $V_{ANODE} > 0.643 \times V_{CATHODE}$.

The other major alteration was the orientation of the detector. The cathode, now on negative high voltage, was placed at the top, closest to the high voltage inputs. This necessitated mounting the preamplifiers below the anode, for proximity to the readout plane.

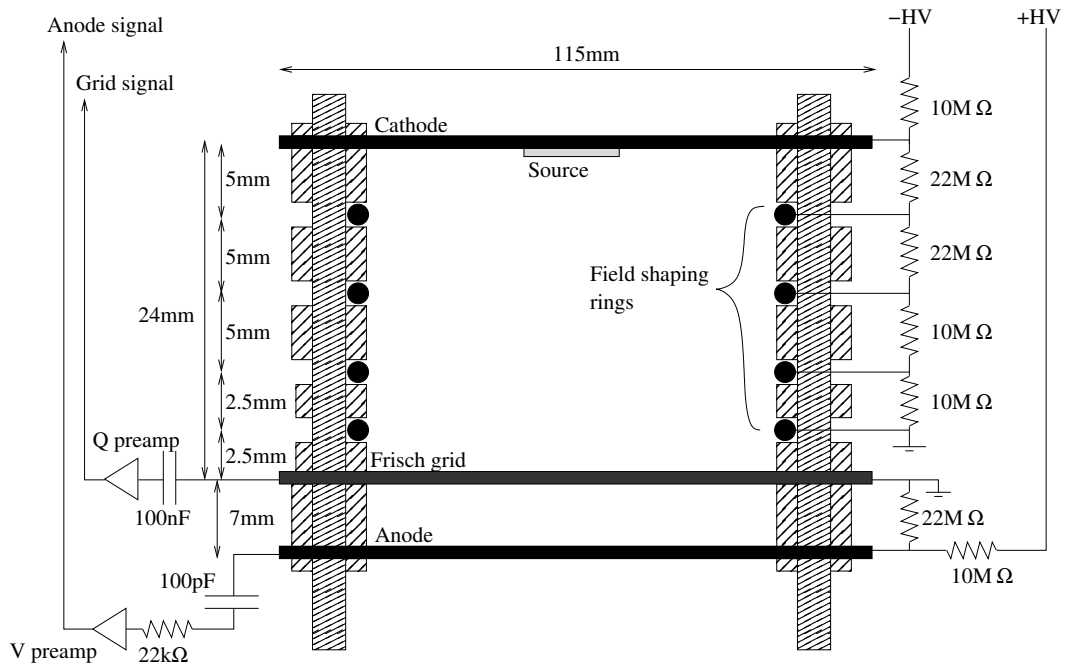


Figure 3.9: A schematic diagram of the rebuilt gridded ionisation chamber, with the anode and grid at the bottom of the chamber, with two power supply circuits. The charge (Q) and voltage (V) preamplifiers are arbitrarily shown as being connected to the grid and anode, respectively. This diagram is not to scale.

The implementation of a detector with the cathode above the drift volume also allows the possibility of a two phase detector, with the source in gas above the detector. This gives the possibility of measuring longer tracks as well as the point source depositions of the α sources in the liquid. In addition, it is possible to use the detector to measure cosmic ray muons, varying the depth of the liquid to measure different amounts of muon deposition energy.

Each variant of the detector was characterised and tested in argon gas. Figure 3.10 shows the energy spectrum of the americium source mounted at the cathode, in the initial detector setup, with an anode voltage of 100 V. The slight tail to the left is due to not all of the alphas being contained within the drift volume. The path length for 3.9 MeV alpha particles in argon gas is roughly 3 cm, and since the source emission is isotropic, not all of the energy was deposited in the detector.

Data taken from this detector in organic liquids forms part of section 4.2.

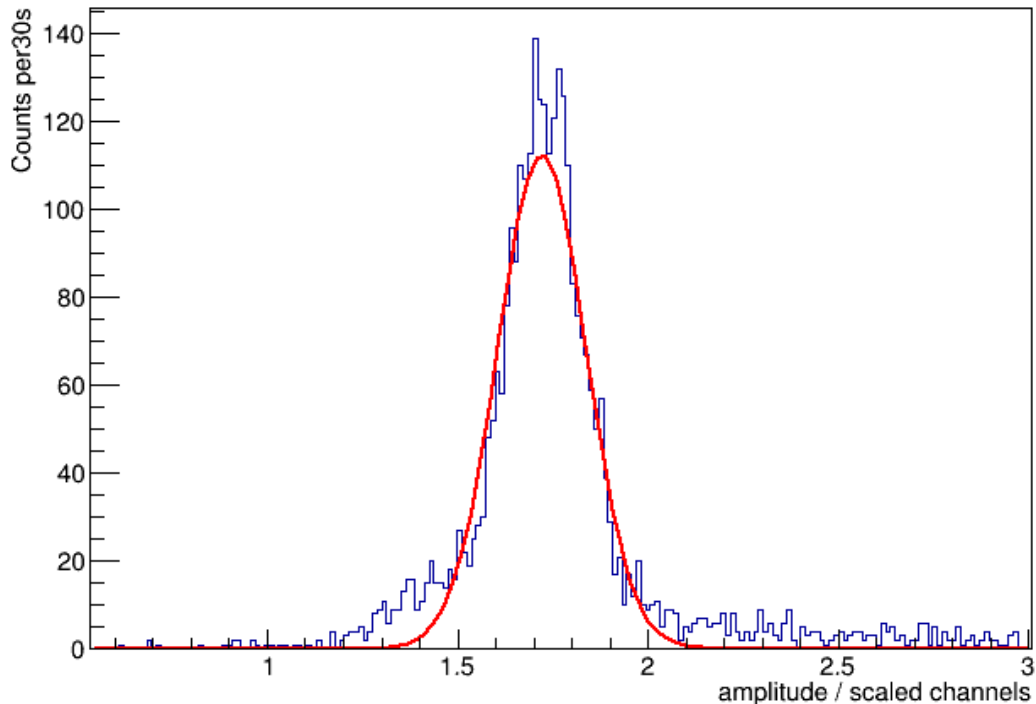


Figure 3.10: The energy spectrum from an americium 241 alpha source in the gridded ionisation chamber in argon gas at an anode voltage of 100 V. The red line shows a Gaussian fit of the data, with mean 1.72 ± 0.01 and standard deviation 0.12.

3.5 Multiwire Proportional Counter

A multiwire proportional counter (MWPC) was implemented in the detector chamber described above, in section 3.4. The detector type was changed primarily to increase the signal to noise ratio of the detector. This improved both due to the decreased capacitive coupling between the anode and cathode, and the charge amplification due to the high electric fields surrounding the wires. A MWPC was, again, chosen for its simplicity, and because its behaviour is well understood, albeit not in the chosen liquids. The drawback of this detector type is the potential for space charge created by any avalanching, which decreases the effective electric field in the drift space. An alternative detector with charge multiplication, but no space charge effects is a drift chamber with THGEM readout. This was not implemented because of the comparative simplicity of the MWPC.

The purpose of this detector was to make the measurements intended to be made by the previous detector. The electron drift speed measurement, however, cannot be made in the same way, since the signal pulse induced in a MWPC is mostly

due to the acceleration of the charge very close to the wire, in the highest electric fields, therefore the risetime of the pulse does not correspond to the motion of the charge across a well-defined detector space (i.e. grid to anode), therefore the speed cannot be measured in this way. An image created using COMSOL Multiphysics [106], showing the electric fields present in the detector is shown in figure 3.11.

The detector consists of an array of $50\ \mu\text{m}$ diameter wires at 5 mm spacing, all connected in series, and a metal mesh cathode, positioned at a variable distance above the wire plane. A lead 210 β source is placed above the mesh cathode. The signal is taken from the grounded wire plane. Due to the variable cathode distance, and the small minimal drift distance, the field-shaping rings are not implemented in the detector configuration. The drift distance is much smaller than the diameter of the detector space, so the electric fields in the centre of the detector, where the source is placed, are uniform. This source was chosen to maximise the possibility of seeing large pulses. The alpha sources, despite having a larger energy deposition are likely, based on the behaviour of other hydrocarbons [79], to have a large quenching factor, and therefore, give a smaller signal. The Pb 210 source has the disadvantage of having a beta emission spectrum, rather than a single energy peak.

The wire plane was constructed by threading a wire through a specially constructed metal holder, hence the wires all being connected in series. This maximises the signal but means the detector plane cannot be used for tracking.

The preamplifier used is the voltage-sensitive device described above, only it is DC-coupled to the readout plane, which gives a lower baseline noise for the device, without degrading the signal. On the output of the preamplifier, there is a low pass filter, with a time constant of roughly 10 ns, which cuts out very high frequency background noise above 10^8 Hz, but does not effect the signal. A schematic of this is shown in figure 3.12.

The high voltage power supply used is the same -15 kV supply described in section 3.4, but the feedthrough to the detector caused many problems with breakdown, so the high voltage cable is fed directly into the detector through a grommited hole.

Figure 3.13 is a photograph of the detector.

This detector was tested using the Th 232 source in argon gas, giving the alpha energy spectrum shown in figure 3.14. The testing in argon gas cannot be considered to be a proper calibration of the detector, since the alpha tracks were not fully contained in the detector: The range of 4.0 MeV alpha particles in argon gas is roughly 2.5 cm, whereas the detector depth is 1 cm. The amplitudes of the pulses shown in figure 3.14, are therefore smaller than those measured in the gridded

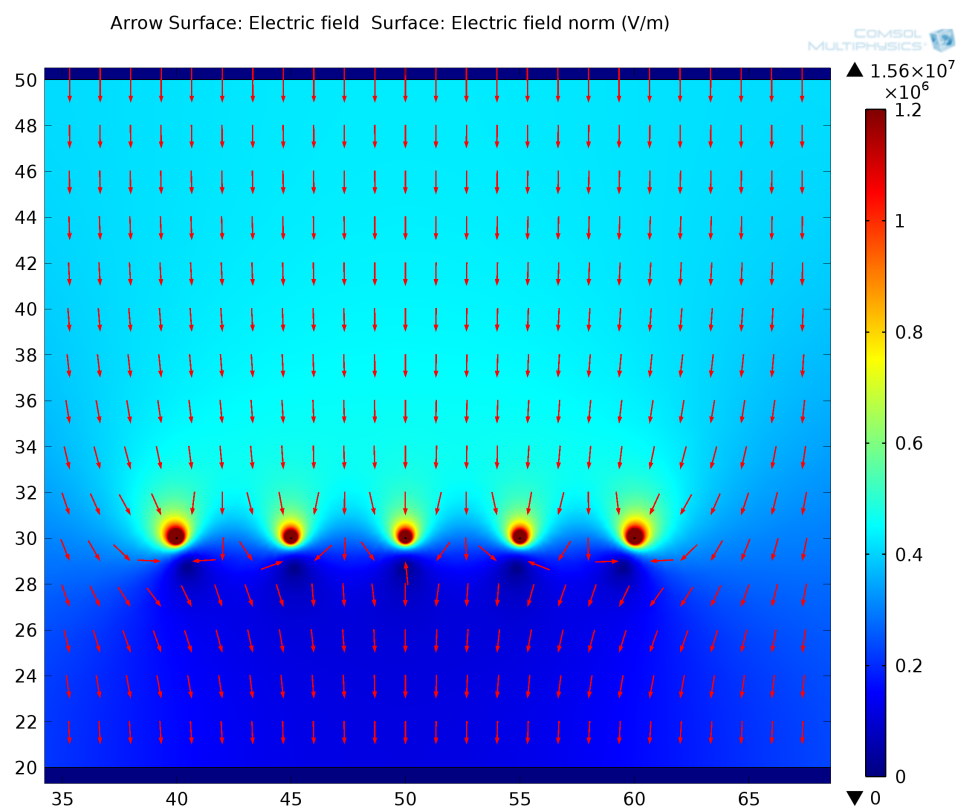


Figure 3.11: A COMSOL image showing a cross-section through part of the MWPC detector. The axes on the left and bottom give the position in mm. At the top of the image is the cathode, and 5 wires out of the wire plane are 20 mm below it. A grounded metal plate is 10 mm below that, at the bottom of the image. The arrows show the direction of the electric field, and the colour shows the absolute value of the electric field, for a cathode potential of 10 kV.

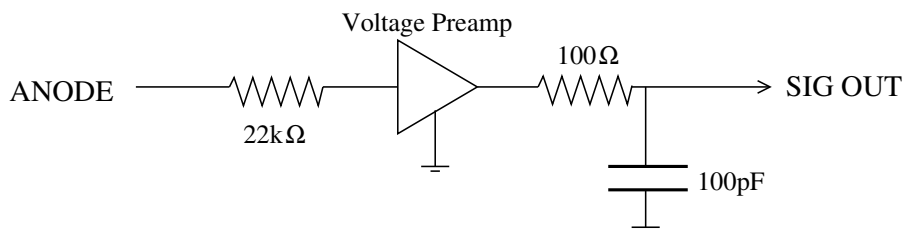


Figure 3.12: A schematic showing the signal path in the MWPC. The anode is directly coupled to the preamp and filtered before leaving the detector chamber.

ionisation chamber. In liquid, the entirety of the energy will be deposited in the detector, which gives the potential for much bigger pulses.

Data taken with this detector forms part of section 4.2.

3.6 Optical Readout Test Stand

Certain organic liquids under investigation were not conventionally used as scintillators, or were typically used in scintillation cocktails, rather than as pure solvents. It was therefore necessary to obtain the emission and absorption spectra of these liquids, and to test their response to a radioactive source.

The emission spectrum was measured using a FP 6500 Spectrofluorometer, and the absorption spectra were measured using a Jasco V 660, in the University of Warwick Chemistry department.

For investigation of the scintillator response to radiation, an optical readout test stand was built. This consisted of two photomultiplier tubes (PMT) sealed looking into a light tight container, containing a Polytetrafluoroethylene (PTFE) dish of diameter 130 mm, and height 34 mm, filled with the scintillating liquid. The PTFE dish has good light reflection properties, as well as being resistant to permeability from the liquids.

The PMTs used were 2" PMTs made by Electron Tubes, with a glass window. The exact characteristics of the PMTs used are somewhat unknown, since the devices used are 9954KA, a custom specification variant of the model 9954B. The typical quantum efficiency response curve for 9954B is shown in figure 3.15 for reference.

The three devices used for data-taking are of the same type, although they have been found not to behave identically. This is unsurprising, as they are devices which are being reused whose last use was a little over thirty years ago! The PMTs have been modified by fitting a BNC connector to the back end, connected to the grounded final dynode, which gives the largest signal output from the device.

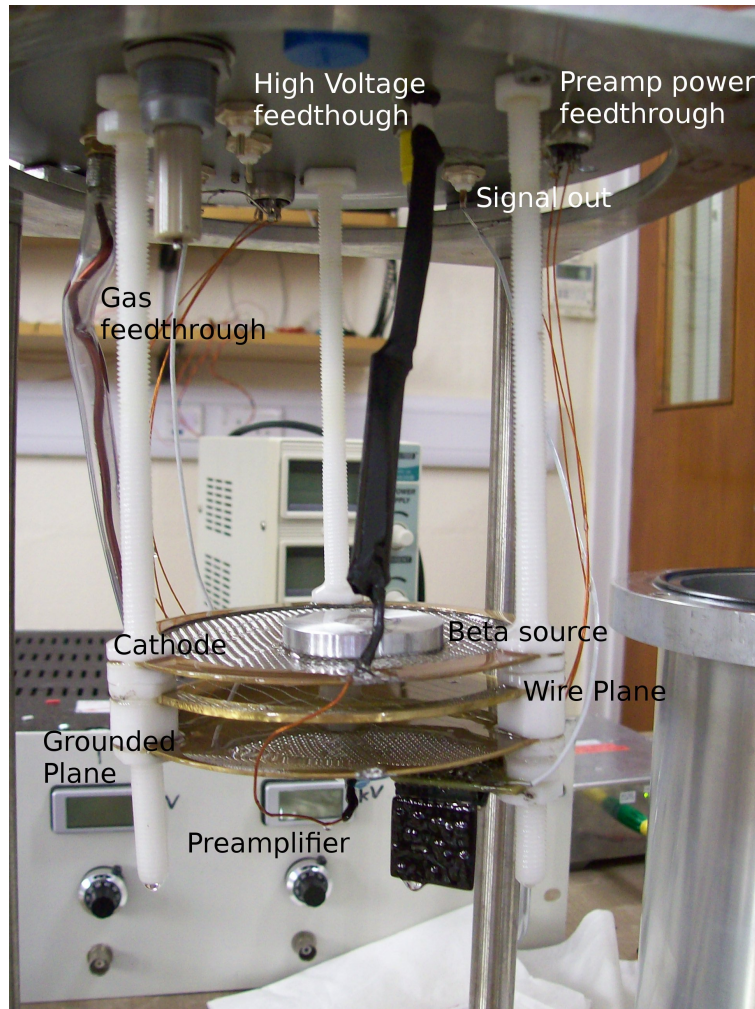


Figure 3.13: The multiwire proportional counter.

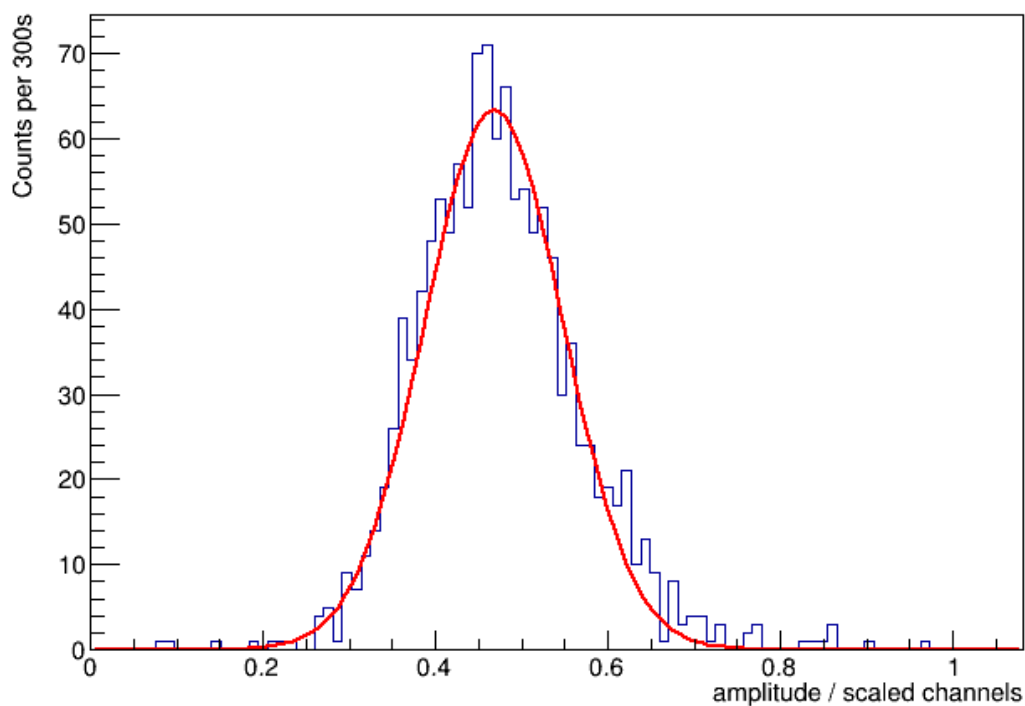


Figure 3.14: The α energy spectrum from the multiwire proportional counter for the thorium 232 source in argon gas at a cathode voltage of 2000 V. The red line shows a Gaussian fit to the data, with mean 0.471 ± 0.003 and standard deviation 0.082.

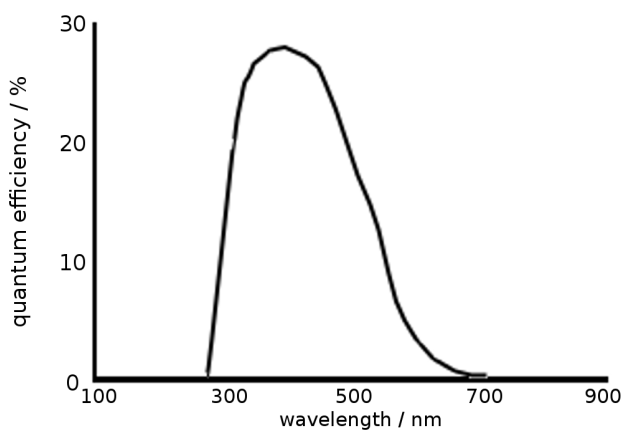


Figure 3.15: Quantum efficiency as a function of incident light wavelength for the PMT type 9954B, copied from [107].

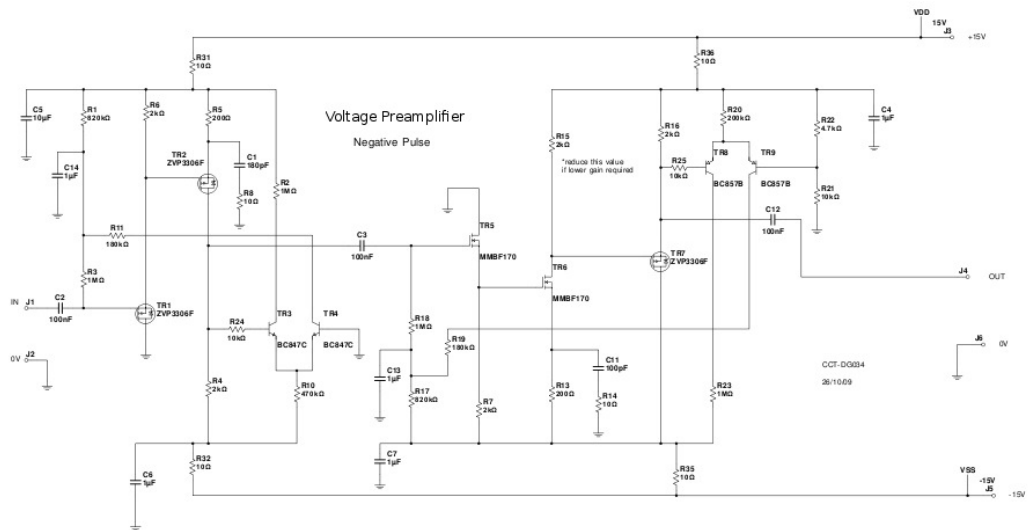


Figure 3.16: Circuit for the custom-made voltage preamplifiers used for the PMTs. The gain is a factor of 14.

The PMT signals are impedance matched and amplified by voltage-sensitive preamplifiers (type 2 as described in 2.3.5, see figure 3.16 for circuit diagram), and are passed through a NIM LRS 620BL discriminator module into a LeCroy 465 coincidence unit to reduce background from the PMT dark count rate.

The random coincidence spectrum was measured by outputting the discriminator signals from both channels into a Time to Amplitude Converter (TAC) Ortec 566 NIM module. The TAC spectrum with no source in the detector is shown in figure 3.17. It shows a flat distribution of random coincidences, as expected for no light present in the detector. The TAC spectrum with a light source present in the detector is shown in figure 3.18. The detector contained the liquid scintillator cocktail Ecoscint O, with the thorium source. The peak in the spectrum where time is 63 bins corresponds to the true coincidence from the light source. The time spectrum has a 16 ns delay inserted between the two signals. This provides a timing calibration for the TAC spectrum of 4 bins per nanosecond.

Two alpha sources, Am 241 and Th 232 were separately submerged within the liquid, and cosmic ray muons were also measured. For calibration purposes, two different muon measurements were taken, with different amounts of liquid scintillator within the dish, such that different amounts of radiation were deposited by the minimum ionising particles into the liquid.

For these muon spectrum measurements, the detector setup is placed between two plastic scintillator paddles read out by PMTs. A coincidence trigger is taken

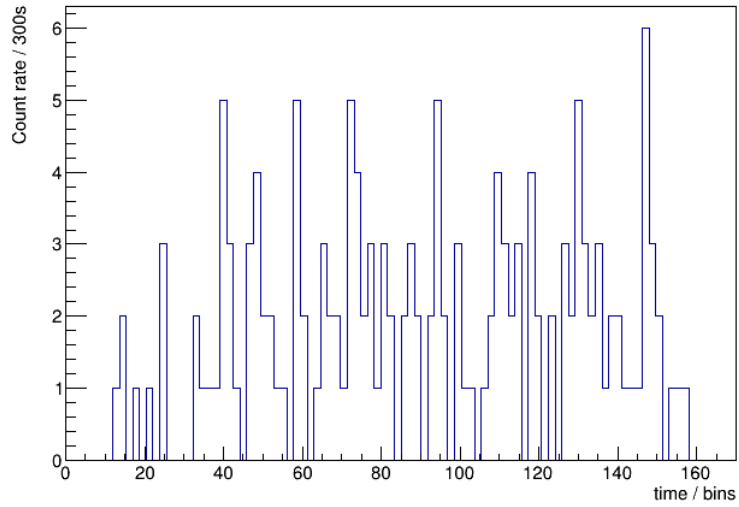


Figure 3.17: The TAC spectrum for the two PMTs, with no source present in the detector. The flat distribution shows that there are only random coincidences present.

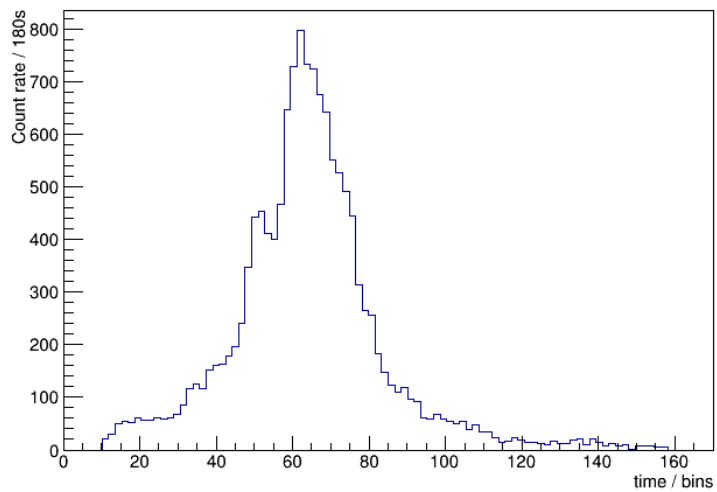


Figure 3.18: The TAC spectrum for two PMTs looking at the dish containing the liquid scintillator cocktail Ecoscint O, with the thorium source. The peak in the spectrum can be attributed to the light source. There is a 16 ns delay inserted in the system for timing calibration.



Figure 3.19: The optical readout detector system: Left, the PMT power supply, data acquisition system, and NIM crate, and Right, PMT power supply, the detector, and two muon paddles.

from the scintillator paddles, using a LeCroy 465 NIM module, so that a muon has passed through both paddles, and therefore (with a certain probability) the detector. The muon paddles each cover an area of roughly 0.2 m^2 , which is much larger than the detector area, and so are positioned orthogonally to each other, giving a smaller vertical overlapping area, and therefore a lower coincidence rate - increasing the fraction of detector events. Since a large fraction of the muon flux is vertically downwards (due to the positioning of the muon detectors), the energy deposited in the detector will form a peak at the energy proportional to the depth of liquid in the detector. The detector system is shown in figure 3.19.

This detector was commissioned using the organic liquid scintillator cocktails, whose energy spectra are given in section 4.1.2. The data taken using this detector are also presented in this section.

Following these measurements, the scope of the optical readout test stand was extended, by implementing a Thick Gas Electron Multiplier (THGEM) in the setup. The aim of this was to measure optical signals (both primary and secondary scintillation) in combination with a charge readout signal from the THGEM. This leads back to the primary purpose of the thesis - to investigate room temperature liquids with a view to finding a liquid suitable for both light and charge readout. The secondary purpose of this detector was to try and determine the origin of various pulse populations observed in the gridded ionisation chamber and MWPC with the aid of dual readout, and well-understood light signals in this detector.

An 0.8 mm thick THGEM manufactured by Cleveland Circuits¹ with 0.8 mm holes at a spacing of 1.2 mm was held a distance of 10 mm from a wire mesh cathode by Delrin threaded bars and spacers. This apparatus was submerged in liquid in the PTFE dish as used in the original optical readout setup. The detector was oriented such that the THGEM was below the mesh cathode, so that any light produced in the detector volume was visible to the PMTs mounted on the lid. The setup was kept as similar as possible to the measurements taken without THGEM, in order to keep the light yield results comparable.

A voltage-sensitive preamplifier (described in section 3.4) was AC-coupled to the back side of the THGEM to take the charge signal. A negative high voltage was applied to the cathode, the front of the THGEM was grounded, and the back side on positive high voltage.

Two baseplate feedthroughs were attached to the detector lid, for the two high voltage channels and the preamplifier signal and power. It was not possible to show light tightness with a flat TAC spectrum in this instance, due to failure of one of the PMTs.

As this experimental setup was implemented very late on in the experimental work, there was insufficient time to fully complete the intended experiment. There were problems with noisy preamplifiers, and a failed PMT, and therefore charge signals and coincident light signals from within the detector were not possible. It was also not possible to show the light tightness of the adapted lid with feedthroughs using a TAC spectrum, since both PMTs are needed for this. The PMT dark count rate with no source is sufficiently low that the detector was considered to be light tight.

For the experiment, the dark count rate from the single PMT was considerably higher than the event rates with coincident trigger, which made external triggering the most favourable option. The detector chamber was set up between

¹www.pcb.co.uk

Table 3.4: Parallel plate distances in the dark current detector, and corresponding E fields

Distance (mm)	E field (kVmm ⁻¹) at V = 3kV
1.0± 0.1	3
2.0± 0.2	1.5
3.0± 0.2	1
4.0± 0.2	0.76
5.8± 0.2	0.52
9.6± 0.2	0.32
19.7± 0.3	0.152

the muon paddles, and cosmic ray muons were used as a source, with a triple coincidence signal between the two muon detectors, and the detector chamber PMT. The coincidence signal from the muons was taken first, and then fed into a second module of the coincidence unit with the PMT pulse. This allowed the coincidence window for the muon paddles to be much narrower than the second coincidence window, since the muon paddles pulses are much faster than the other PMT pulses, since the detector PMT pulses are lengthened by the preamplification.

The scintillation light observed for a cosmic ray muon source by the single PMT incident on the detector was measured as a function of drift voltage, and the results are shown in section 4.3.

3.7 Dark Current Measurements

A test stand was constructed to measure the dark current in the liquids. The current can be measured across a small drift chamber, consisting of two parallel plates etched onto two pieces of single-sided PCB. There is no radioactive source present in this detector, as its only purpose is to measure the background current from the liquid itself.

Since the dark current varies as a function of time as well as electric field, as discussed in section 2.4.2, it was decided to make several measurements in parallel. The detector was constructed in a small diecast box, with seven drift chambers, as described above, each with a different drift distance, but connected to the same bias voltage, hence giving an array of different electric fields. The inside of the detector is shown in figure 3.20, and the detector system is shown in figure 3.21.

The parallel plate distances and corresponding electric fields are listed in table 3.4.

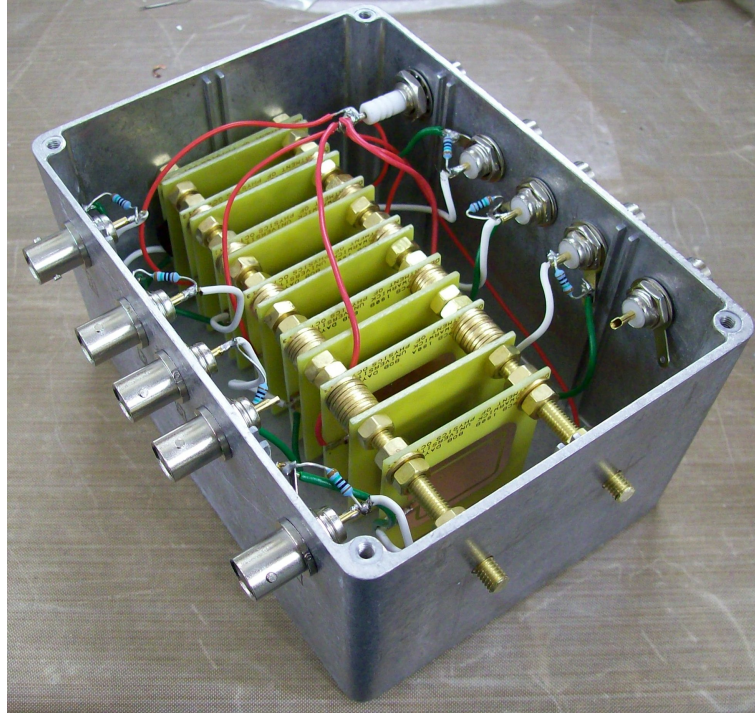


Figure 3.20: Dark current detector comprising seven drift chambers of varying drift distances.

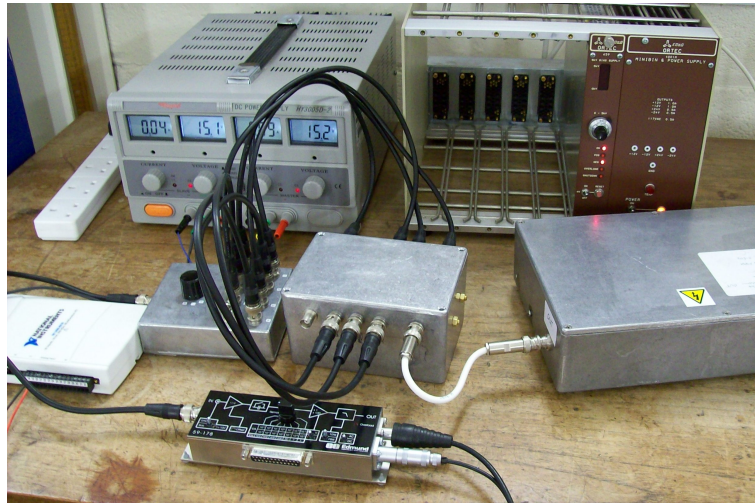


Figure 3.21: Dark current detector system. From right, power supply filter, NIM crate with power supply module, current detector box, current sensitive preamplifier, preamplifier power supply, detector channel switch and USB datalogger.

Each signal output plate has a central area surrounded by an unconnected guard ring. Both of these are grounded, but the guard ring is grounded directly, whereas the central area is DC-coupled to the preamplifier. The biased plate has a square with rounded corners, extending to the outside of the parallel guard ring. This means that the signals collected will correspond to the motion of charges in the uniform electric field in the central area of each drift chamber.

The signal output is connected to a FEMTO DLPCA-200 variable gain low noise current amplifier (type 1 as described in section 2.3.5), with a low pass filter at 10Hz. Since we have only a single preamplifier of this type, the outputs from the detector are fielded into a multi-way switch, and the output can be varied without any physical contact with the detector. This reduces the noise present in the system when it is moved.

The high voltage power supply is an Ortec 659 5 kV bias NIM module, connected to the detector via a low pass filter (described in section 3.4) to decrease noise from the power supply.

The data was taken constantly at a rate of 1Hz on the channel with the highest electric field, with data points taken daily on the other channels. For each of the non-continuous channels, data was taken for one minute, and the average calculated. The shape of the distribution will be the same for all of the channels, so can be estimated from the constant channel.

The results from this detector are shown in section 4.2.3.

3.8 Data Acquisition Systems

The data acquisition system (DAQ) used with the detectors described in sections 3.3, 3.4, 3.5 and 3.6 is a National Instruments crate NI PXI-1042, with embedded controller unit NI PXI-8101. The modules used were an 8 bit 100 MHz digital oscilloscope module, NI PXI-5112, and a 12 bit digitiser module NI PXI-5124 sampling at 200 MSamples per second.

The software interfacing these modules is a custom written LabVIEW code (shown in figure 3.22), which can sample pulses of specified length in up to two channels, for a set duration. The triggering mechanism is based on behaviour of a single selected channel, or external trigger, which can be set to trigger on an analogue pulse edge, or immediate rolling trigger.

The programme has also been developed to include a time delay loop, allowing the user to sample for a set amount of time, at a certain time interval, indefinitely. This is useful for monitoring the change in liquids over a lengthy period of time.

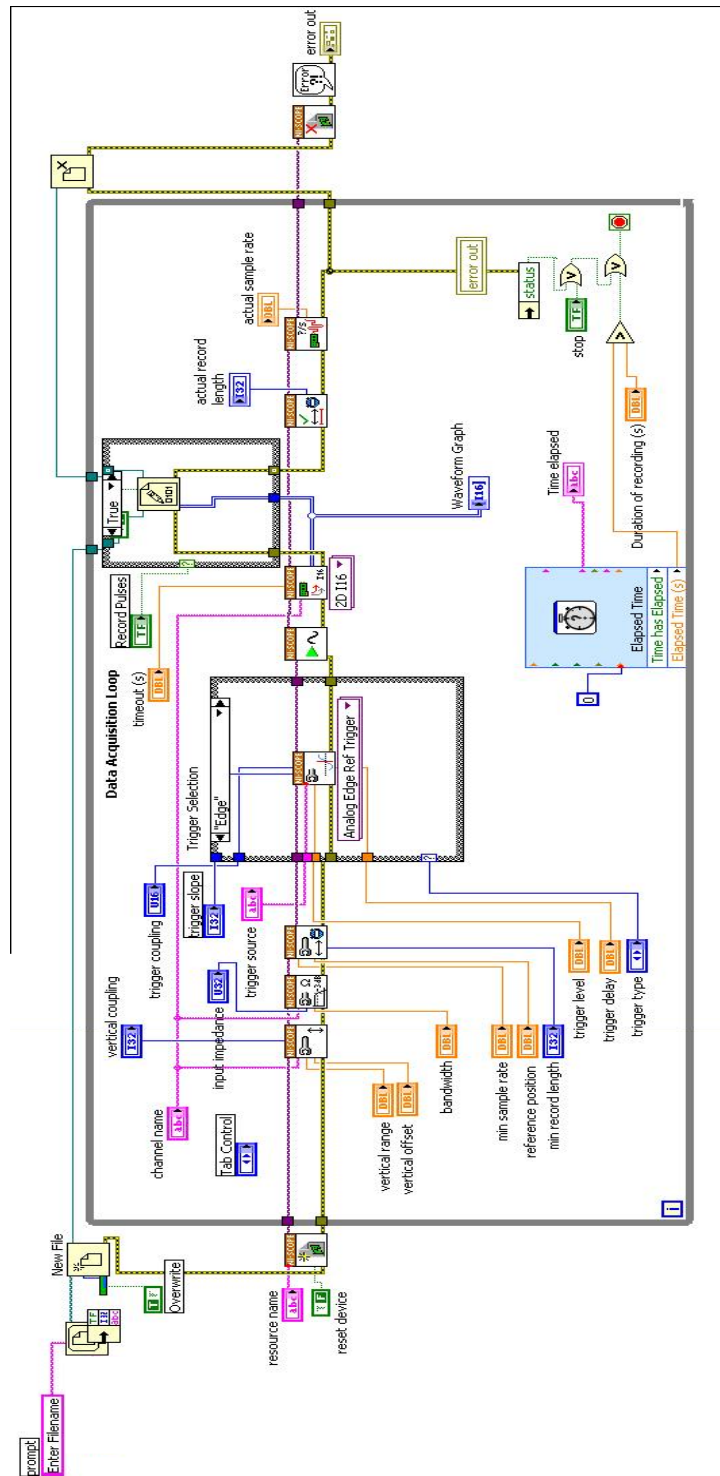


Figure 3.22: The Block Diagram for the LabVIEW data acquisition code. The main part of the programme runs inside a while loop, which can be ended manually, or by a predefined time. The triggering mechanism, and the option to write pulses to disk, are within separate case structures. These are manually set at the programme front end.

The data is written to disk in binary format. The binary files are extremely space efficient, as well as being effective at interfacing a LabVIEW data acquisition system with C++ data analysis tools.

The data acquisition system used for the measurements made by the detector in section 3.7 was much more simplistic, since a high sampling rate is not needed. The signal from the current preamplifier is logged to a text file using a 16 bit 250 kSamples per second National Instruments USB datalogger NI USB-6210, and NI Signal Express running on a Windows 7 computer.

3.9 Data Processing Tools

The binary data written to disk by the primary DAQ system is in either 8 bit or 12 bit format. In the binary files, the pulses are written back to back, so it is necessary to know what the sampling window from the DAQ was in order to correctly separate the binary file into pulses. In the first data processing programme, the data is first split into pulses, and each pulse waveform is converted into a ROOT [108] TH1I object, with one histogram bin per sample. The TH1I histograms form a branch of a TTree. If two channels are being simultaneously written to disk, the histograms are sorted into separate branches. Since the amplitude of the pulses is all relative to the number of bits (256 bins, or 4096 bins), the amplitude is scaled to the range on the DAQ system, which makes the amplitude scale comparable between different sampling ranges. This code also has the functionality to reverse the polarity of the pulses, for ease of analysis.

In the second data processing programme the ROOT histograms are used to calculate characteristic parameters of each pulse. Firstly, the pulses are smoothed, using a moving average filter. Since the first and last few bins cannot be averaged, they are flagged as being unsmoothed. Different pulse parameters are calculated depending on whether the input pulses are from a charge or voltage-sensitive preamplifier, since the parameters have different physical meanings in each case (see section 2.3.5).

Firstly the baseline is calculated, by averaging the first 5% of the sampling window, excluding the initial unsmoothed bins. If the baseline is higher than a defined threshold, the pulse is flagged as a failed pulse.

The highest value bin in the sample is taken to be the position, and the pulse amplitude is calculated by subtracting its value from the baseline. If this is in the unsmoothed bins, it is flagged up as a failed pulse, similarly if the amplitude is very small, this is flagged as having low signal to noise.

For multiple channels, the amplitude values are added together to make a summed-amplitude parameter.

The onset of the pulse is the first bin which has 30% of the amplitude of the pulse. The risetime is then calculated as the time between 30% and 70% of the pulse height. If the onset is found to be after the position, this is flagged as a failed pulse.

The decay time of the pulse is taken as the time between the position of the pulse, and the bin at which the value equals twice the exponential decay time: $\text{amplitude} \times e^{-2}$.

For charge pulses, the average induced voltage can be calculated, by calculating the gradient of the risetime.

For voltage pulses, the integral of the pulse can be calculated, which is equal to the charge collected, for some types of voltage preamplifier as discussed in section 2.3.5. This is the sum of all of the bins between the onset and the end of the decaytime. Where the integral of the pulse is negative, the pulse is flagged as a failed pulse. As mentioned previously, this code has been developed to deal with a single polarity of pulse - inversion is possible in the primary conversion stage, if necessary. The risetime of the charge is also calculated, as the sum of all of the bins between the onset and the position.

In spite of some of these parameters having no physical meaning with respect to the output of the different preamplifiers, they can be useful for differentiating between pulse populations.

These parameters are calculated for each pulse, and the values put into parameter histograms in a branch of a TTree object. For multiple channels, the parameter histograms are all in the same branch, but are labelled according to channel (i.e. baseline0, baseline1). This is the most logical structure to incorporate multi pulse cuts and the summed amplitude parameter in the two channel case, although for larger numbers of channels it would be better to have a tree for each channel and use a TFriend object to link the trees.

The pulse waveform data output from the initial data processing programme is also included in this histogram, which makes it possible to view pulses after cuts have been applied, and visually identify the characteristics of different pulse populations.

The waveform pulses, and the parameter histograms are viewed and analysed using ROOT. A summary of the functions of these parameters is shown in table 3.5.

In addition to the parameter calculation, a pulse fitter has been applied to some of the data pulses. This allows selection of a given population of pulses

from a data sample, containing any number of different pulse populations. The pulse template is created by applying harsh cuts to a data sample to select a small number of pulses with the desired appearance.

This fitter code takes a ROOT file containing a TTree of TH1I template pulse histograms, and averages these to create a pulse template. It then takes the ROOT file containing TH1I data pulse histograms, and relates each data pulse to the template pulse, and outputting the fit parameters, as described below.

For each TH1I pulse, the fitter iteratively compares the template. The scale factor for the amplitude of the pulse is determined, using a least-squares fit. The scale factor, and the mean square deviation from the template are the fitter results. In the context of pulse comparison, the logarithm of the deviation from the pulse template is more useful, therefore it is calculated and output. Vector objects are filled with the pulse values for each of the outputs, which are stored in a TNtupleD.

These two parameters are examined alongside the parameter histograms described above, and used for making data cuts. A summary of the pulse fitter outputs is included in table 3.5.

Table 3.5: The calculated pulse parameters, and their functions.

Parameter	Description	Charge or Voltage
<i>baseline</i>	average of first 5% of sampling window (excluding unsmoothed bins)	Charge and Voltage
<i>amplitude</i>	value of highest value bin with baseline subtracted	Charge and Voltage
<i>summedamplitude</i>	amplitude of all channels summed	Charge and Voltage
<i>position</i>	bin number of highest value bin	Charge and Voltage
<i>onset</i>	first bin number at which value is 30% of amplitude	Charge and Voltage
<i>risetime</i>	number of bins between and the bins with 30% (onset) and 70% of amplitude	Charge and Voltage
<i>decaytime</i>	number of bins before the bin value is $\frac{amplitude}{e^2}$.	Charge and Voltage
<i>chargeamplitude</i>	sum of values of all of the bins between onset and bin with height $\frac{amplitude}{e^2}$.	Voltage
<i>chargerisetime</i>	sum of values of all bins between onset and end of risetime	Voltage
<i>voltage</i>	the gradient of the risetime	Charge
<i>failflag</i>	present (1) for bad pulses with: high baseline low amplitude to baseline ratio position in unsmoothed bins position before onset 0 value otherwise	Charge and Voltage
<i>scaleresult</i>	the pulse fitter scale result	Charge and Voltage
<i>logms</i>	the log mean square deviation of the pulse from the template	Charge and Voltage

Chapter 4

Results

The aim of this research was to find a room temperature liquid with both good charge transport properties and good optical properties. This has been approached from two perspectives: transport of charge in dielectric liquids with previously demonstrated optical properties (or those showing promise), and optical readout of liquids with previously demonstrated charge transport properties.

4.1 Optical Readout

The first results presented are those investigating the optical properties of the liquids. Each of the scintillator cocktails, base solvents, and “non-scintillator” liquids has been investigated to compare and contrast the results.

4.1.1 Absorption and Emission Spectra

The light emission (red) and absorption (black) spectra were measured in each of the liquids DIN, PXE, MIBP, MIPN, C5 and TMP using the apparatus described in section 3.6 of the previous chapter, and are shown in figures 4.1-4.6. For the absorption measurement, the spectrofluorometer was first calibrated by measuring the spectrum with no vessel, and then with a completely opaque cuvette in place of a sample. The measured spectra are scaled to the range given by these measurements. A background measurement of the cuvette containing water was taken to ascertain the cleanliness of the vessel.

The absorption is measured as a logarithmic ratio between the incident radiation (I_0), and the radiation transmitted through the material (I). For values of $\log \frac{I_0}{I}$ larger than three, the amount of light passing through the material is less than one percent of the incident light, and is therefore negligible. The fluctuations

which occur in some of the plots above this level is due to the inaccuracies in the instrument, since the error is larger for low light detection.

The emission spectra are from an incident light source of wavelength 300 nm, with emission measurements starting at 310 nm, above the light source threshold. Two other incident wavelengths were also tested, 220 nm and 250 nm, but in the majority of cases the emission spectrum remained identical in shape, but with lower amplitude.

The bandwidth of wavelengths being measured at any one time can be altered, to give a lower light yield, but higher accuracy measurement. The measurements presented in this section all have the same bandwidth, except figure 4.6. This liquid had a high light yield, and so the bandwidth was adjusted to compensate. The absolute difference between the two has not been calculated, since these measurements were made predominantly for the pulse spectrum shape rather than absolute light output comparison, and the bandwidth calibration is non trivial.

The emission spectra from an incident monochromatic light source will give an indication of the emission spectra for the liquids, but is not expected to result in the same spectrum as ionising radiation from a source.

This is because the excitation of the liquids by photons with energy 4.13 eV differs from excitation by ionising radiation. The ionising radiation has the potential to excite higher energy states which are not available to the lower energy excitation from the photons. Nevertheless, the difference between the two methods of excitation can give an insight into the excitation states of the liquid.

For Di-isopropyl naphthalene, the liquid is completely absorbent to any light below the wavelength of 340 nm, at which point it sharply changes to being optically transparent. The emission spectrum, shown in figure 4.1 appears to have a fairly simple structure with a double peak at 355 nm, and 365 nm. The spectrum extends into the visible light region. The sharp rise in emission at 340 nm suggests that the liquid is self absorbing, therefore any emitted light below this wavelength would not be detectable in this measurement. The single emission wavelength of the liquid means that the de-excitation of the molecules happens in predominantly the same way, producing a monochromatic light emission.

Mono isopropyl naphthalene has a similar structure to DIN, the absorption drops gradually from 310 nm, and more sharply at 340 nm to transparency. The features on this spectrum might also be attributed to the sensitivity of the spectrometer at low light levels. The emission spectrum is much wider than that of DIN, but with a similar simplicity in structure. There is a shoulder at 340 nm, as the liquid stops self-absorbing. The main peak is just into the visible light at around

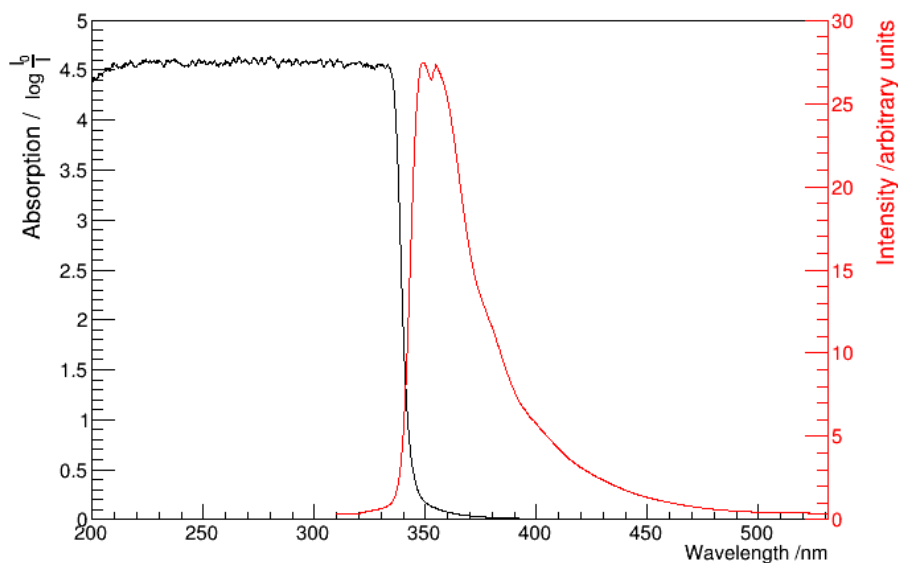


Figure 4.1: The light emission (red) and absorption (black) spectra for Di isopropyl naphthalene.

400 nm. The absolute intensity of emission is much lower than that of DIN. This was the case for all of the incident wavelengths of light tested, 220 nm, 250 nm and 300 nm. The spectra are shown in figure 4.2.

Mono isopropyl biphenyl has an almost identical structure to DIN, with a sharp drop off in the absorption at 330 nm. There is a single emission peak, which cuts off very sharply at 350 nm. This suggests that most of the light is self-absorbed. Despite this, the light yield is much higher than DIN. The simplicity of this spectrum, and the relative amplitude of the light yield suggest that this liquid should behave as a good scintillator. The spectra are shown in figure 4.3.

Phenyl xylyl ethane has a very similar structure to DIN and MIBP, but with a lower self absorption limit at 295 nm. The emission peaks sharply at 305 nm, with a comparable intensity to that of MIBP. Again, the simplicity of the structure in the emission spectrum suggests that this liquid is a good scintillator, and indeed, it is used as one. The spectra are shown in figure 4.4.

The absorption spectra of Cyclopentane are somewhat different from those of the liquids discussed above, in that it appears to have a much more gradual change in absorbance, with complete opacity below 240 nm, less than 10% of the light passing through below 285 nm, decreasing to near optical transparency at 320 nm. Unlike the other liquids, the emission spectrum has very little self-absorption. There is a double peak structure with peaks at 330 and 345 nm, and a shoulder at 320 nm.

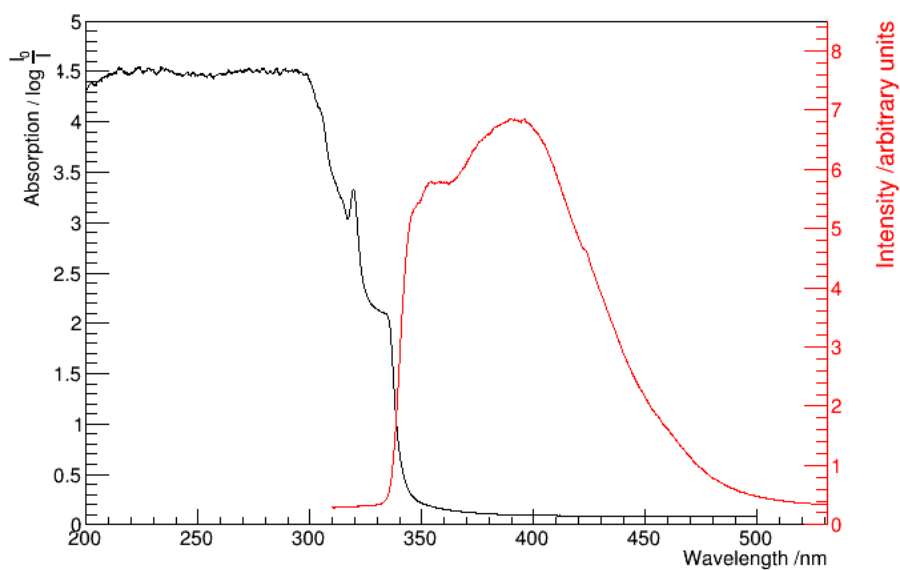


Figure 4.2: The light emission (red) and absorption (black) spectra for Mono isopropyl naphthalene.

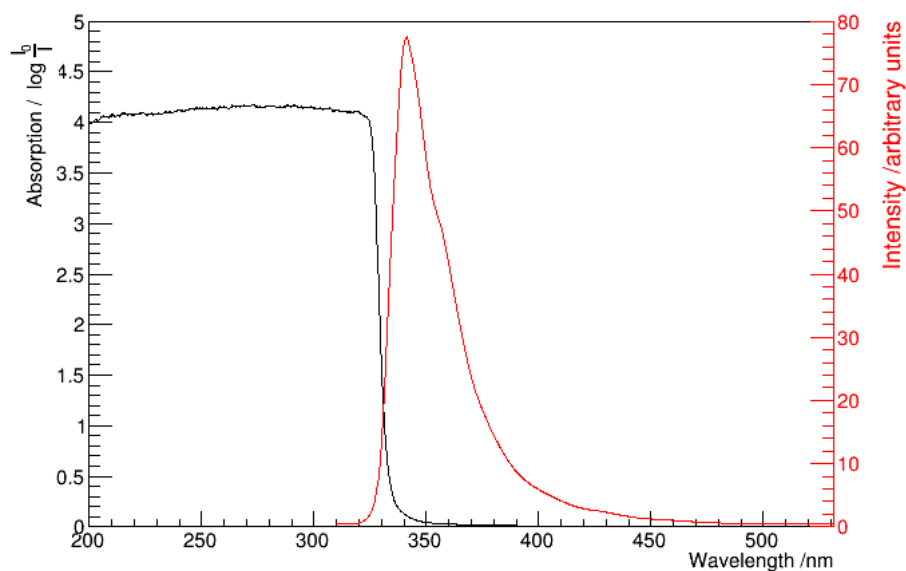


Figure 4.3: The light emission (red) and absorption (black) spectra for Mono isopropyl biphenyl.

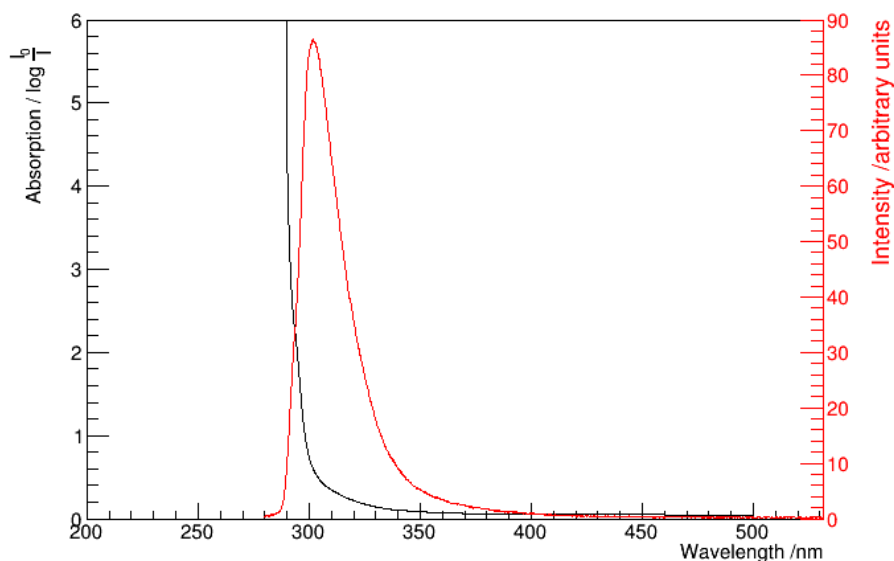


Figure 4.4: The light emission (red) and absorption (black) spectra for Phenyl xylyl ethane.

It was shown from the lower wavelength incident light samples that the emission spectrum decreases to zero around 290 nm, as would be expected from the absorption spectrum shown. The structure of the emission spectrum suggests that there are several modes of excitation of the liquid. The intensity of the light measured is roughly an order of magnitude higher than that measured in PXE and MIBP, most likely due to the lack of self absorption. The spectra are shown in figure 4.5.

Tetramethylpentane is again, rather different from the other samples. The absorption spectrum is very similar to DIN, PXE and MIPN, with a sharp drop in absorbance at 285 nm marking the distinction between opacity and transparency. The emission spectrum appears to be predominantly non-self absorbing, and has been shown (using lower wavelength excitations) to decrease to zero emission below 290 nm. The striking difference between the TMP emission spectrum and the other liquids is the complexity. There are at least 3 peaks in the spectrum, at 340 nm, 365 nm, and 380 nm, with maximum emission at the central peak. This difference in structure reflects the different ways of exciting the liquid. The large number of peaks suggests that the scintillation response is complex, and there are many different excitations. The emission spectrum, shown in figure 4.6 is non-comparable with the other spectra with respect to intensity of light emitted, since the intensity of emission necessitated decreasing the bandwidth - the amount of light emitted by TMP is therefore higher than all of the other liquids.

The emission and absorption spectra allow us to compare and contrast the

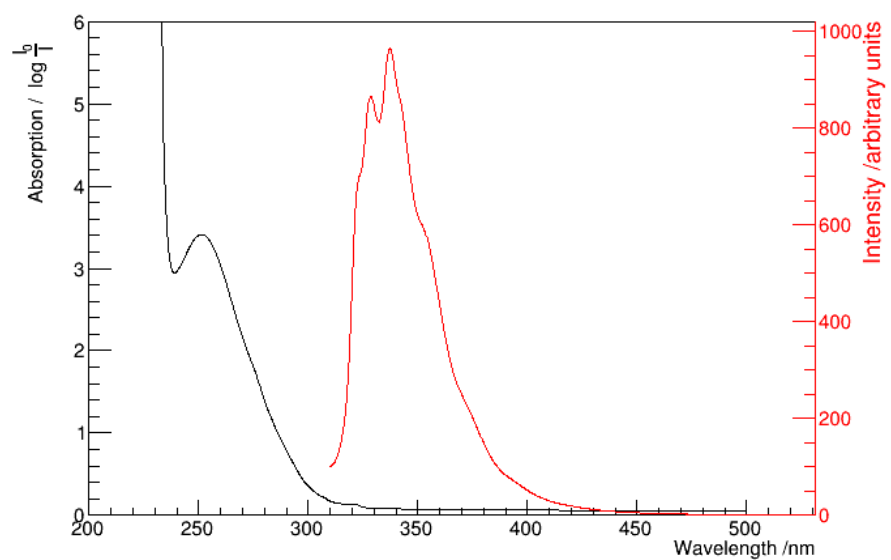


Figure 4.5: The light emission (red) and absorption (black) spectra for Cyclopentane.

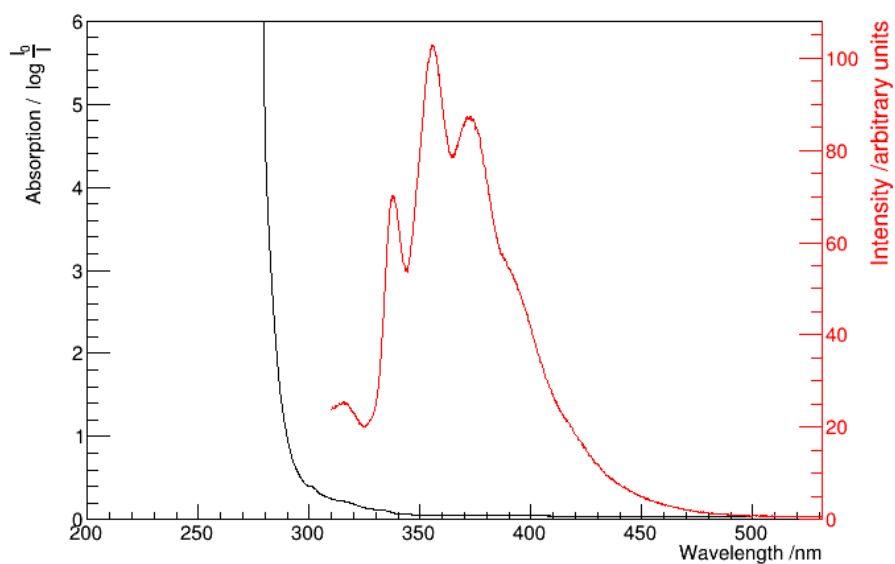


Figure 4.6: The light emission (red) and absorption (black) spectra for Tetramethyl pentane.

structures present in the light emission from each liquid. A simple, single peak structure suggests monochromatic light emission, such as one would expect from a good scintillator. This is found in the liquids DIN, PXE and MIBP. For DIN and PXE, this is expected, since they are commonly used base solvents for liquid scintillator cocktails.

A slightly more complex structure, such as the double peak structure found in C5, and the wider emission spectrum found in MIPN gives an indication that the liquid may not work as well as the liquids with a single peak.

The complex structure found in TMP suggests that it is unlikely to produce a monochromatic light output for a consistent source, which makes for an inefficient detector. This liquid does not, therefore exhibit properties of a good scintillator in its emission spectrum.

4.1.2 Alpha and Beta spectra

Energy spectra are presented from the liquids Ecoscint O, Optifluor O, PXE, DIN, MIPN, MIBP, TMP and C5 with a selection of incident radiation sources. Measurements were taken using the apparatus described in section 3.6 of the previous chapter. The initial five liquids used a consistent setup, with a PMT failure necessitating a device change, and system re-calibration prior to the final three liquids. The system is not calibrated absolutely; the liquid scintillator cocktail Ecoscint O is taken as a standard candle to which the other liquids are compared.

The data were taken using the Am241 α source, cosmic ray muons, and the Th232 source. The energy resolution for each of these sources is presented, as is, where possible, the alpha quenching factor. A summary table of these results is shown in table 4.3. Details of the muon measurements and an overview of the thorium source analysis are presented below.

Cosmic ray muon source

Since the cosmic ray muons triggered on by the detector are travelling approximately vertically, the amount of energy deposited in the detector varies as a function of liquid depth and density, with roughly 2MeV deposited per gcm [63]. For the liquids used, the density, and the calculated amount of energy deposited is shown in table 4.1.

Thorium source analysis

As discussed in section 3.1, the thorium 232 source is not in equilibrium, but is old enough to have a measurable contribution from both alpha and beta emissions in the decay chain.

An analysis has been done on the decay times of the pulses present in the sample, from which it is possible to split the thorium source spectrum up into alpha and beta contributions. The decay time spectra in americium and muon samples are first inspected, and a cut on the decay time made based on maximising the efficiency of selection. The efficiency and purity of the cut are defined as follows, for alpha pulses:

$$\text{efficiency} = \frac{\text{number of } \alpha \text{ pulses in selection}}{\text{total number of } \alpha \text{ pulses}} \quad (4.1)$$

$$\text{purity} = 1 - \frac{\text{number of muon pulses in selection}}{\text{total number of pulses in selection}}. \quad (4.2)$$

The muon tracks produce an electron-like response from the detector, and so are considered as β pulses. Figure 4.7 shows the decay time spectra from the americium source and cosmic ray muon pulses in Ecoscint, averaged across both PMTs. The clear distinction between the peaks shown is not present in all of the liquids, but it is still possible to make a cut with a lower efficiency and purity in most of the liquids where the spectra overlap. The average decay time was shown in figure 4.7 purely for illustrative purposes, and is not used in the cuts themselves; the cuts are applied separately to each of the two coincident PMT pulses, and the pulse is only included in the selection if both pulses pass the cut. This improves the pulse selection.

Once the cuts have been selected, they are applied to the thorium spectrum, distinguishing alpha pulses from beta pulses. The majority of the events, as expected, are the initial Th 232 decay via a 4.0 MeV α , although the alpha spectrum will also include small contributions from the other alpha decays further down the chain. The higher energy selection plateau comprises the multiple beta contributions. They are indistinguishable at the low event rates present. Figure 4.8 gives the emission spectra in Optifluor for thorium before (blue) and after cuts. The cut selection in red is the alpha spectrum, and the cut selection in green is the beta spectrum.

There is additional evidence of decays further down the thorium decay chain, in that there are a small number of double pulse events present in the sample, which could correspond to the decay of Bi 212 followed by Po 212. The polonium has a half life of 298 ns, which is well within the sampling window. An example of one of

Table 4.1: The Muon energy deposited in each liquid

Chemical / Cocktail Name	Density (gcm^{-3})	Muon energy deposited (MeV)	
		1 cm depth*	2 cm depth*
Optifluor O	0.86	1.72	3.44
Ecoscint O	0.91	1.82	3.64
Ultima Gold F	0.96	1.92	3.84
DIN	0.96	1.92	3.84
PXE	0.985	1.97	3.94
MIPN	0.98	1.96	3.92
MIBP	0.98	1.96	3.92
Tetramethylpentane	0.72	1.01	2.02
Cyclopentane	0.75	1.50	3.00

*depths in Tetramethylpentane are 7 mm and 14 mm respectively, with corresponding energy deposition values included in the table

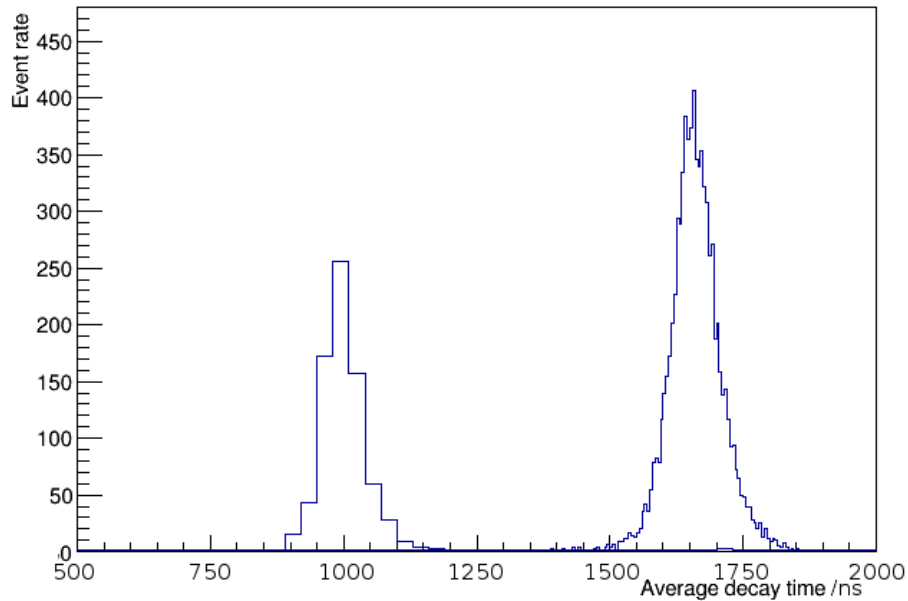


Figure 4.7: The average decay time (over both PMTs) in Ecoscint for americium α (right) and muon (left) pulses. In this case, the distributions are well separated, and making a distinction between alpha and beta decay times is possible with high efficiency and purity.

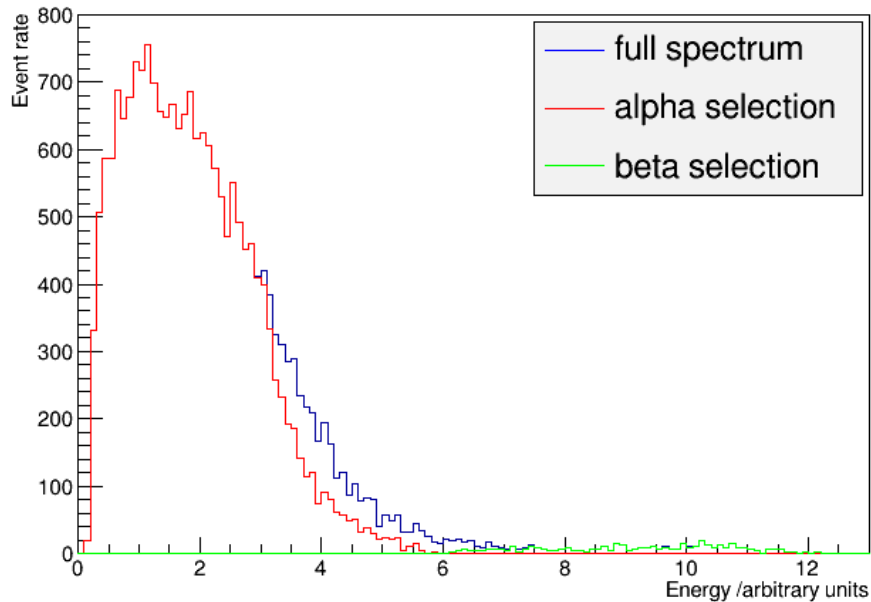


Figure 4.8: The thorium energy spectrum in Optifluor O, without cuts (blue) and with alpha (red) and beta (green) selections.

these double pulses in DIN is shown in figure 4.9. There are very few of these pulses in the entire sample, as is expected from the broken equilibrium of the source. This means that no further analysis can be done using the BiPo pulses.

Standard candle - Ecoscint O

The liquid scintillator cocktail Ecoscint O is taken as an example of a liquid with good scintillation properties, and therefore is used as the comparison standard for the other liquids.

As such, it is used to set the achievable standard in energy resolution for the detector setup. The energy resolution of commercial liquid scintillator in an optimised setup is roughly 20-25% [87]. This is due to the small fraction of the kinetic energy of an incident particle that is converted to light, rather than heat and lattice vibrations. In addition to this, large amounts of energy (several 100 eV) are needed to produce a scintillation photon.

The energy resolution in the unoptimised setup used for these experiments is therefore expected to be much worse than 25%. The light has two additional surface interfaces which depreciate the resolution; that between the liquid and air, and the air and PMT glass.

The following cuts were applied to each Ecoscint sample: $failflag_{PMT1} < 1$,

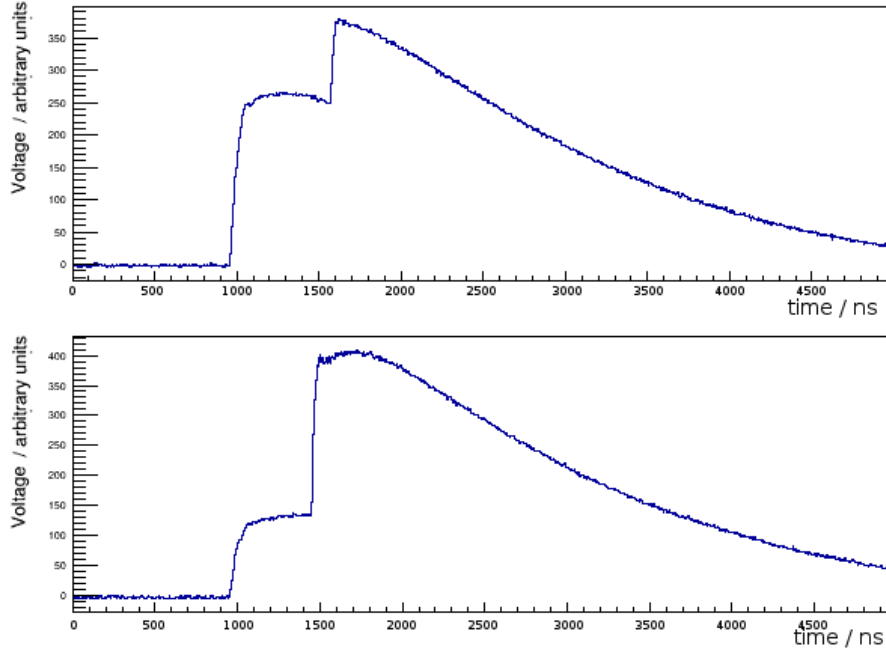


Figure 4.9: A double pulse observed in DIN, in PMT 1 (upper) and PMT 2 (lower): possible evidence of the Bi 212 and Po 212 decays in the thorium decay chain.

$failflag_{PMT2} < 1$, $|position_{PMT1} - position_{PMT2}| < 50$ ns. This removed any non-pulse samples, and gave a more stringent cut on the coincidence of the pulses. For reference, all of the pulse parameters are summarised in table 3.5.

The energy spectrum for Ecoscint O (with PMTs 1 and 2) is shown in figure 4.10. The americium alpha peak (red) has an energy resolution of 71%. The thorium source energy resolution (light green) is much worse, at 233%. The reason for the striking difference is twofold. The main contribution to the difference is the shape of the sources. The thorium source is cylindrical, and emitting over 4π . Since there is a large amount of variation in the efficiency of the detector for different angles of emission, this broadens the spectrum. The other aspect of the difference is that there are multiple peaks present in the thorium decay chain, and whilst analysis has been done to separate the alpha pulses from beta pulses, introducing an uncertainty, there are multiple alpha peaks in the spectrum, as shown in figure 3.2. The muon peak with 1 cm liquid depth, (light blue) shows the optimum energy resolution possible, with an energy resolution of 18%. The thorium beta spectra (dark green) are indistinguishable, but extend to roughly the energy of the 1 cm muon peak, which corresponds to the endpoint of the highest energy beta emitted, at 2.25 MeV.

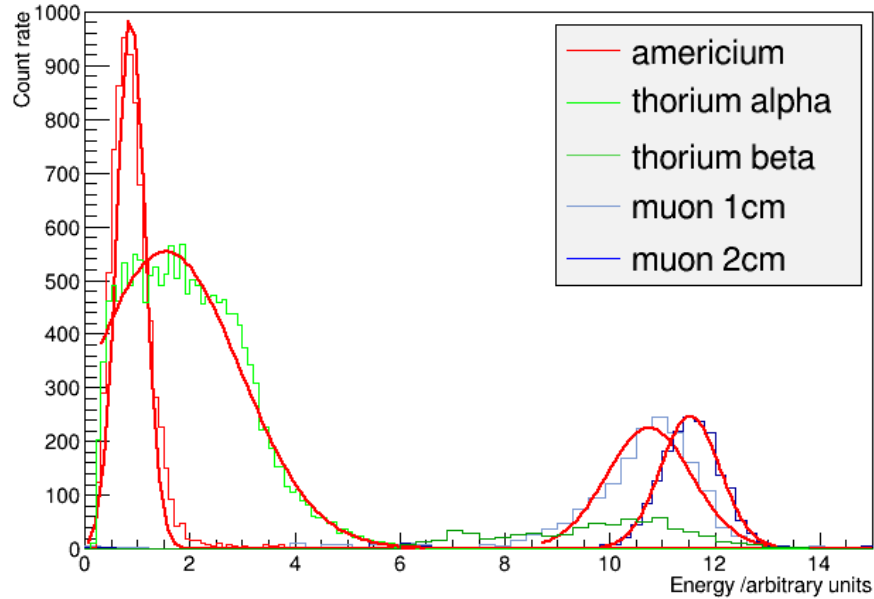


Figure 4.10: The energy spectrum for Ecoscint O, showing the americium alpha (red), thorium alpha contributions (light green), thorium beta contributions (dark green), and the muons (light and dark blue). The smooth red lines show the Gaussian fit of the distributions, the results of which are shown in table 4.3.

The muon peak at 2 cm liquid depth (dark blue) has apparent width of 12%, however the measurement itself must be reconsidered in light of the electronics, as discussed below.

The thorium source data sample has been split into alpha and beta contributions with a decay time cut at $1.5 \mu\text{s}$. The thorium alpha selection cut has 99.3% purity and 98.5% efficiency. The thorium beta selection cut has 99.9% purity and 93.6% efficiency.

Taking the value of the smaller muon peak, with energy 1.82 MeV as 10.76, and the value of the americium alpha peak of 3.9 MeV as 0.886, gives a value for alpha quenching of 26.0.

The input of the preamplifier used for the PMT signals has crossed diodes on the input (see figure 3.16), in order to protect the preamplifier from large voltage pulses at the input stage. The threshold for this is 860 mV, much lower than the 1.1 V anticipated (given the maximum output constraint of 15 V, and the amplification factor of 14). This means that any input pulses larger than 860 mV have been artificially scaled down in amplitude.

The largest pulses input to the preamplifier were from cosmic ray muons passing through 2 cm of liquid scintillator cocktail. These large light pulses form

Table 4.2: Comparison of the performance of PMTs 1 & 2 and 2 & 3

		PMTs 1 & 2	PMTs 2 & 3
Number of events	Americium	7915	6395
	Muon 2 cm	1801	1285
Mean energy	Americium	0.886 ± 0.005	0.663 ± 0.003
	Muon 2 cm	11.54 ± 0.01	11.02 ± 0.02
Energy resolution	Americium	71%	84%
	Muon 2 cm	12%	14%

the dark blue spectrum shown in figure 4.10. The energy deposition in 2 cm of liquid is expected to be twice that deposited in 1 cm of liquid, as shown in table 4.1, therefore one would expect the position of the light blue peak in figure 4.10 to be a factor of two smaller than the dark blue peak. This is evidently not the case in either of the liquid scintillator cocktails. This suggests that the largest PMT pulses, coming from the deposition of energy in the 2 cm liquid configuration, are affected by the preamplifier input protection diodes, and scaled to a smaller pulse amplitude, hence moving the peak towards lower energies on the spectrum.

Since the other liquids measured have smaller light outputs than the LSCs, they are predominantly unaffected by this, and in fact, the deviation from the factor of two between the 1 cm and 2 cm peak positions on each of the energy spectra is less than 1σ . The peak like structure around 11.5 in figure 4.13 can also be attributed to the higher energy tail being scaled down in amplitude by the input diodes, thereby creating an artificial peak with the saturated pulses being superimposed on the tail.

The dark blue spectra in figures 4.10 and 4.12 have been included for completeness, but have not been included in the summary tables, or used for the alpha quenching factor, since the data is meaningless.

After the failure of PMT 1, it was replaced with another (PMT 3). The detector was then characterised again by taking data (in Ecoscint) with the americium source, and the higher energy muons. The replacement PMT performed poorly in comparison to the original pair. With identical cuts, there are 20 - 39% fewer events in the PMT 2 & 3 sample, the mean energy is between 5 and 25% lower, and the energy resolution is between 4 and 13% worse. A comparison of the performance of the two detector setups is given in table 4.2, and the energy spectra are contrasted in figure 4.11.

The difference in behaviour of the two PMTs is put down to the age and the condition of the PMTs. It is unfortunate that the liquids whose characterisation was most critical were examined using the inferior setup, but this can be taken into

consideration in the data analysis.

Optifluor O

Another scintillation cocktail, this liquid illustrates again the properties of a good scintillator. For this reason the energy spectra of Optifluor and Ecoscint are very similar.

The selection cuts applied to each sample were the following: $failflag_{PMT2} < 1$, $failflag_{PMT1} < 1$, $|position_{PMT2} - position_{PMT1}| < 50$ ns. These cuts are identical to those for Ecoscint, removing any samples not containing a pulse, and making a more stringent cut on the coincidence of the pulses.

The energy spectrum for Optifluor is shown in figure 4.12. The energy resolution is very similar to the Ecoscint cocktail, in that the americium peak has an energy resolution of 90%, the thorium alpha peak is much wider, at 233%. The energy resolution for the muons appears to be slightly worse than in Ecoscint, at 21% and 16%. The main difference in structure is the detection of the lower energy muons, whose event rate is much lower than the corresponding event rate of higher energy muons. The thorium beta spectra, similarly to the Ecoscint spectrum, extend to roughly the position of the smaller muon peak, at 2.25 MeV. As above, the position data for the 2 cm muon peak is meaningless, due to electronics, but has been included for completeness.

The thorium source data sample has been split into alpha and beta contributions with a decay time cut at $1.5\mu s$. The thorium alpha selection cut has 99.9% purity and 99.6% efficiency. The thorium beta selection cut has 90.6% purity and 97.1% efficiency.

Taking the value of the smaller muon peak, with energy 1.72 MeV as 10.518, and the value of the americium peak of 3.9 MeV as 0.683, gives a value for alpha quenching of 34.9.

DIN

The energy spectra for DIN are similar in some aspects to those of the scintillator cocktails (LSC), although there are marked differences.

The following cuts were applied to each sample: $failflag_{PMT2} < 1$, $failflag_{PMT1} < 1$, $|position_{PMT2} - position_{PMT1}| < 50$ ns. These are identical to those used for the LSC.

The energy spectrum for DIN is shown in figure 4.13. The americium (red) and thorium (light green) alpha peaks are of similar shape to those of the LSC, however this is where the similarities end. The peak emission of DIN, as shown

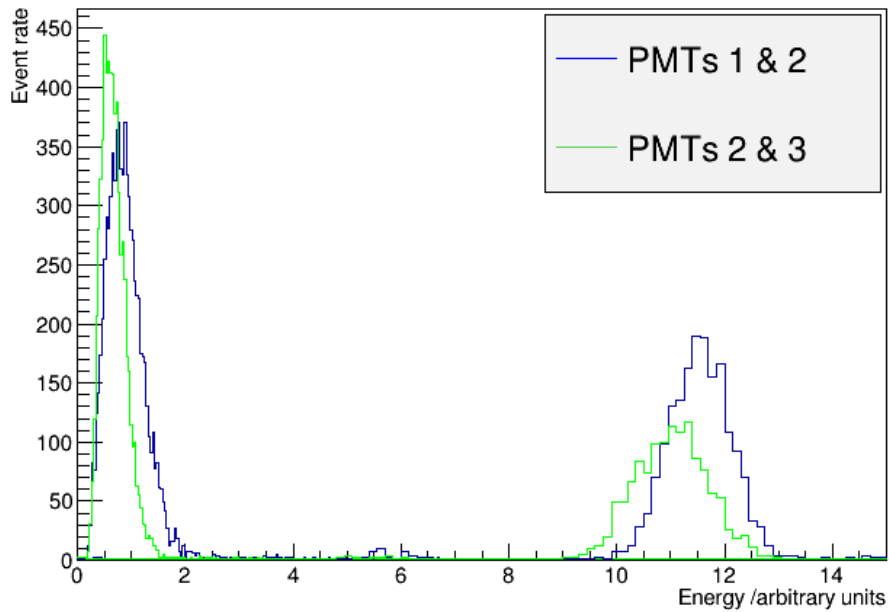


Figure 4.11: The energy spectra for americium (left) and 2 cm muon depth (right) in Ecoscint O, with PMTs 1 & 2 (blue), and PMTs 2 & 3 (green). The binning and sampling times are equal for each source in each liquid.

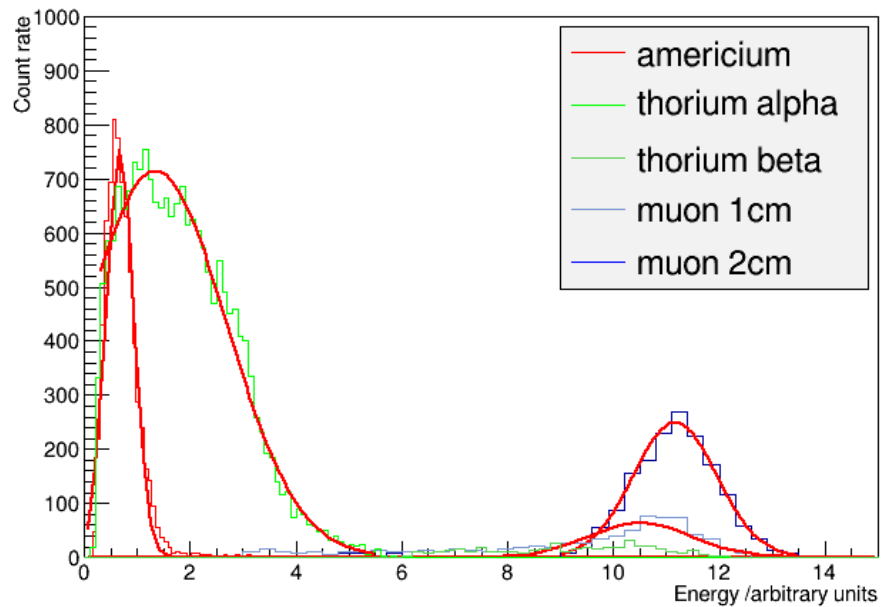


Figure 4.12: The energy spectrum for Optifluor O, showing the americium alpha (red), thorium alpha contributions (light green), thorium beta contributions (dark green), and the muons (light and dark blue). The smooth red lines show the Gaussian fit of the distributions, the results of which are shown in table 4.3.

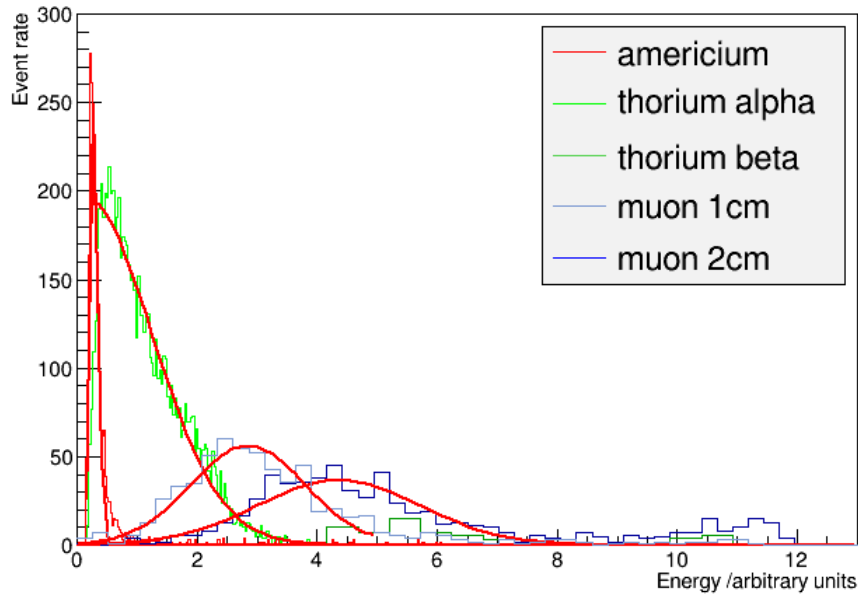


Figure 4.13: The energy spectrum for DIN, showing the americium alpha (red), thorium alpha contributions (light green), thorium beta contributions (dark green), and the muons (light and dark blue). The smooth red lines show the Gaussian fit of the distributions, the results of which are shown in table 4.3.

in figure 4.1, is 360 nm, although the emission peak does extend beyond this into the blue. The efficiency of the PMT peaks at around 400 nm, and drops sharply to 300 nm, as shown in figure 3.15. This means that at the peak emission wavelength of DIN, not all of the light is being collected. This means all of the peaks are shifted to the left on the spectrum. Whereas the shape of the alpha sources are broadly consistent with the LSC, the energy resolution for the muon peaks is significantly degraded, due to both the width of the peaks, and through moving the peak to the left. They are at 79% and 73% respectively. The thorium alpha peak has likewise changed, with an energy resolution an order of magnitude larger, at 2388%, despite an almost identical width in the LSC. This is partially due to the poor fitting of the energy spectrum. The americium source on the other hand has a better energy resolution, at 53%. This is most likely due to the amplitude of the lower energy pulses not making the hardware cut at the discriminator - there are a factor of 3 fewer pulses for the same acquisition window. This means that the distribution is being shaped by the hardware.

The thorium source data has been split into alpha and beta contributions with a decay time cut at 1.8 μ s. The thorium alpha selection cut has 75.5% efficiency and 86.8% purity. The thorium beta selection cut has 54.6% efficiency and 86.8%

purity. The decay time peaks were much less distinct than in the LSC cases, but nevertheless, separable with an adequate level of purity and efficiency.

The alpha quenching factor can be estimated, with the caveat that the mean value of the alpha peak is being shaped by the hardware cut off, and therefore should be considered an upper limit on the alpha peak. Taking the value of the 3.84 MeV muon peak as 4.37, and the 3.9 MeV americium alpha peak as 0.290 gives a value for alpha quenching of 15.3. This value can therefore be considered to be a lower limit for alpha quenching.

The solvent DIN clearly behaves as a good scintillator, with the detector quality degraded only by the quantum efficiency of the PMTs. This gives a slightly degraded energy resolution and lower event rate. Nevertheless, the alpha/beta discrimination is still possible with a high efficiency. The PMT inefficiency is normally solved by the addition of wavelength shifting fluors, to produce a LSC.

PXE

PXE is another pure solvent, and is used as the basis of the Ecoscint LSC.

The pulse selection was made using the following cuts: $failflag_{PMT2} < 1$, $failflag_{PMT1} < 1$, $|position_{PMT2} - position_{PMT1}| < 200$ ns. This cuts out any non-pulse samples, and has a slightly less stringent cut on the relative position than used in the LSC. It was found that cutting below this did not affect the shape of the spectra, only the number of pulses present in the sample.

The PXE energy spectra are even more affected than DIN by the drop in efficiency of the PMT, since the emission spectrum has a sharp peak around 305 nm, and the emission beyond 350nm is of very low intensity, as shown in figure 4.4.

For this reason, the left hand side of the energy spectrum is very crowded, as all of the energy spectra have been smeared towards lower energies. A small number of events have maintained high light output, including some of the beta emissions from the thorium source.

All of the energy spectra have been fit with a Landau distribution, rather than a Gaussian, since they are heavily asymmetric, due to both the long tail towards the higher energies, and the hardware cut-off at low energies. This gives an artificially low energy resolution for the peaks, considering the sharper edge of the distribution. These can be considered as a lower limit for the energy resolution in this setup. The americium peak is the sharpest, at 46%, the thorium wider, at 77%. The muon peaks, in spite of being fit with a Landau, have poor energy resolutions of 89.5% and 74.1%.

The thorium source data has been split into alpha and beta contributions

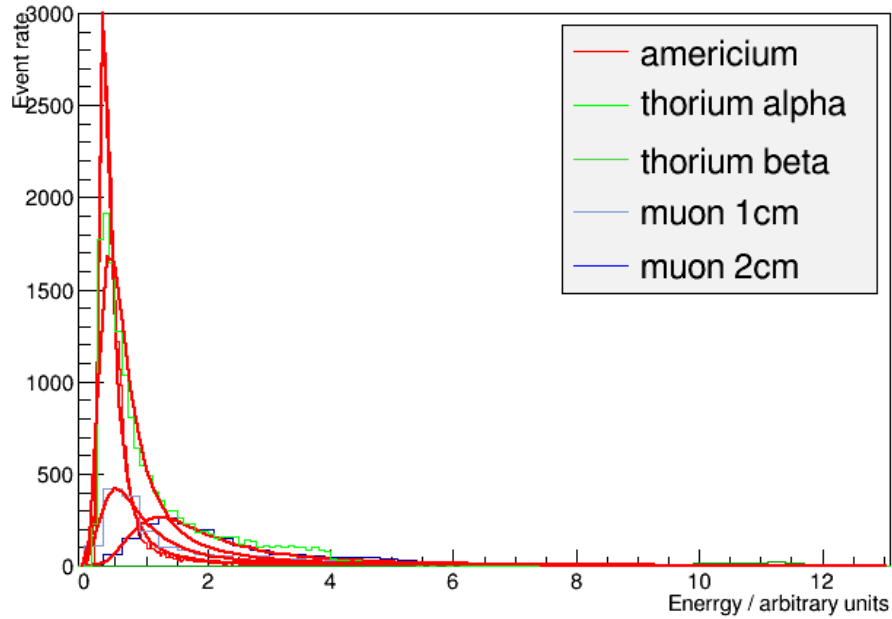


Figure 4.14: The energy spectrum for PXE, showing the americium alpha (red), thorium alpha contributions (light green), thorium beta contributions (dark green), and the muons (light and dark blue). The smooth red lines show the Gaussian fit of the distributions, the results of which are shown in table 4.3.

with a decay time cut at $1.35\mu\text{s}$. The thorium alpha selection cut has 89.1% efficiency and 95.8% purity. The thorium beta selection cut has 67.8% efficiency and 99.5% purity. The decay time peaks are not so well separated as in the LSC case, but are better separated than in DIN.

A lower limit estimation for the alpha quenching, taking a value of 1.316 for the 3.94 MeV muon, and a value of 0.314 for the 3.9 MeV alpha, is 4.15.

Similarly to DIN, PXE shows evidence of good scintillation properties, in spite of the emission wavelengths. The PMT inefficiency has a much worse effect on the energy resolution in PXE than in DIN, due to the relative positions of maximum emission. The alpha/beta discrimination is still possible with considerable efficiency. Again, this liquid is normally combined with wavelength shifting fluors to make a LSC.

MIPN

MIPN is one of the liquids which has not previously been used as a scintillator.

The pulse selection for MIPN was made using the following cuts: $failflag_{PMT2} < 1$, $failflag_{PMT1} < 1$, $|position_{PMT2} - position_{PMT1}| < 125$ ns. The stringency of the cut on

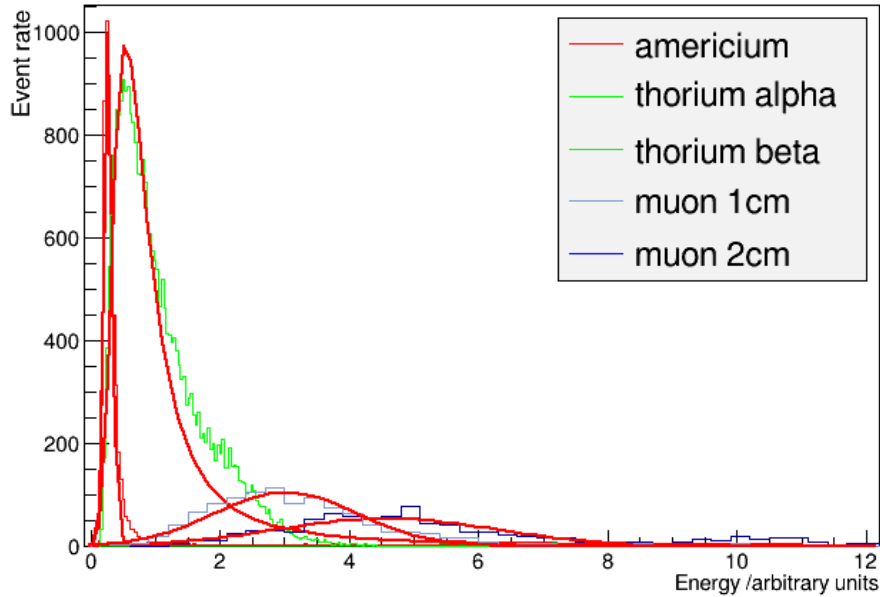


Figure 4.15: The energy spectrum for MIPN, showing the americium alpha (red), thorium alpha contributions (light green), thorium beta contributions (dark green), and the muons (light and dark blue). The smooth red lines show the Gaussian fit of the distributions, the results of which are shown in table 4.3.

relative position was again, determined by when the cut improved the shape of the spectra.

Mono isopropyl naphthalene has a wider emission peak than any of the other organic solvents tested. Its emission peak is around the peak emission for the PMT, however, as is shown in figure 4.2, the absolute light yield is low for this liquid.

The americium has an excellent energy resolution, at 50%, but this is partially due to the hardware cut off. The thorium alpha distribution was fitted with a Landau rather than a Gaussian, due to the lower edge cut off, giving 70% energy resolution as a lower limit. The muon peaks for MIPN are of similar amplitude to the corresponding peaks in DIN, but due to the lower light yield of MIPN, the peaks are wider, making the energy resolutions worse, at 85% and 86%. These muon energy resolutions give a much more accurate representation of the energy resolution of the liquid.

The thorium source data sample has been split into alpha and beta contributions with a decay time cut at $1.7\mu\text{s}$. The thorium alpha selection cut has 49.4% efficiency and 74.6% purity. The thorium beta selection cut has 36.3% efficiency and 78.5% purity. The two peaks are poorly separated, which lowered the efficiencies of the cut.

A lower limit estimation for the alpha quenching, taking a value of 4.59 for the 3.93 MeV muon, and a value of 0.282 for the 3.9 MeV alpha, is 16.2.

Whilst this liquid shows some signs of being a good scintillator, its behaviour is less scintillator like than PXE and DIN. The absolute light yield is low for this liquid, and the energy resolution is poor. This may be linked to the excitation of the liquid; the spectrum is wide, and there are hints of a second peak in the spectrum (see figure 4.2). This could reduce the amount of detectable light, and therefore deteriorate the energy resolution, pulse amplitude, and event rate. The alpha/beta separation is also less efficient than in those liquids classed as good scintillators.

MIBP

MIBP is another liquid which has not previously been used for scintillation counting, and has therefore not had its optical properties tested. The simplicity of the emission and absorption spectra in section 4.1.1 indicate that this liquid shows promise as a scintillating liquid.

Mono isopropyl biphenyl is the liquid at which one of the PMTs failed, consequently there are two comparative sets of data, one with data sets with americium, thorium and 2 cm muon, and the other with all of the data sets.

The energy spectra from the first data are shown in figure 4.16, and are first described, in order that the difference between the two PMTs can be discussed.

The cuts on these pulse samples are as follows: $failflag_{PMT1} < 1$, $failflag_{PMT2} < 1$, $|position_{PMT2} - position_{PMT1}| < 150$ ns, for identical reasons to discussed above.

The emission peak of MIBP is below the most efficient part of the PMT, but above that of PXE, and consequently the pulse amplitudes, of the muons especially, are higher than those observed in PXE. The americium and thorium alpha peaks, in fact, resemble the shapes observed in the LSC, at lower amplitudes, and have similar energy resolutions, at 60% and 192% respectively. The muon peak is very smeared out across the energies, and has a resolution of 42%, this is most likely due to the inefficiency of the PMT. The thorium beta spectra extend to a similar energy to the muons.

For the thorium source data sample to be split into alpha and beta contributions, a decay time cut was made at $1.53 \mu s$. The thorium alpha selection cut has 90.3% efficiency and 97.0% purity. The thorium beta selection cut has 76.9% efficiency and 98.9% purity. The peaks are very well separated, hence the good efficiencies on the cut. The beta efficiency was lowered by a tail on the distribution towards longer decay times, possibly due to inefficiencies in light transmission.

Taking the value of 9.29 for the 3.92 MeV muon, and 0.439 for the 3.9 MeV

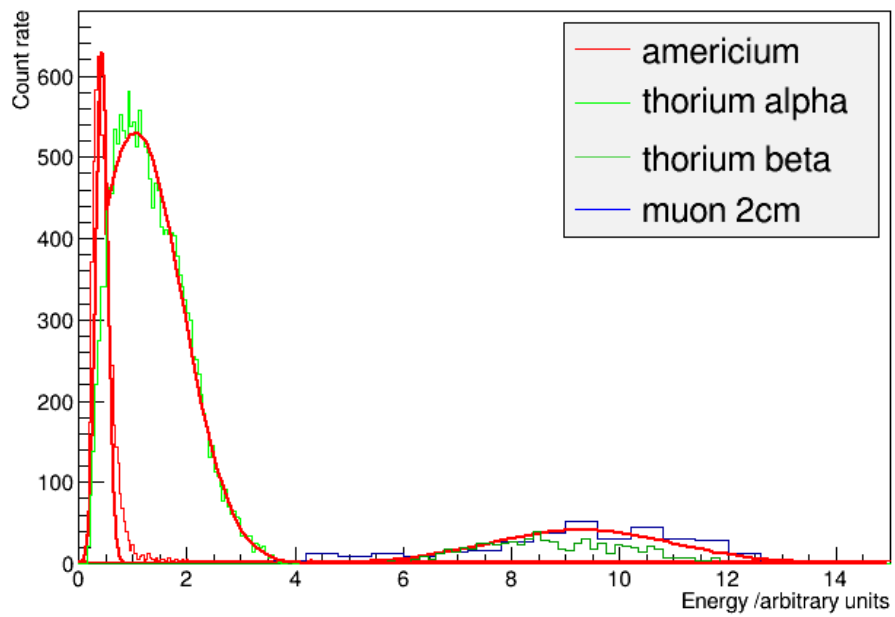


Figure 4.16: The energy spectrum for the initial MIBP measurement, using PMTs 1 and 2. The americium alpha (red), thorium alpha contributions (light green), thorium beta contributions (dark green), and the higher energy muons (dark blue) are shown. The smooth red lines show the Gaussian fit of the distributions, the results of which are shown in table 4.3.

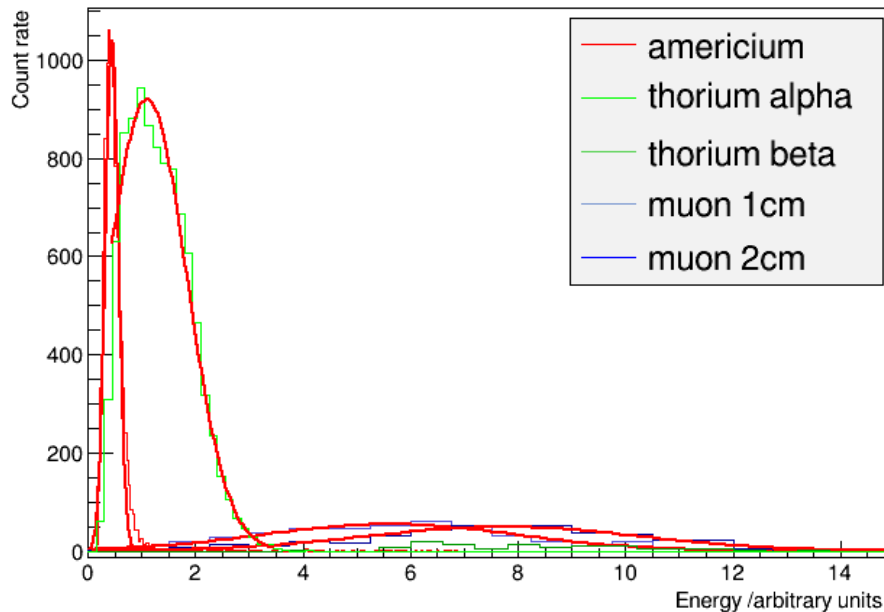


Figure 4.17: The energy spectrum for the repeat MIBP measurement, using PMTs 2 and 3, with the same cuts applied as to the previous sample. The americium alpha (red), thorium alpha contributions (light green), thorium beta contributions (dark green), and the higher energy muons (dark blue) are shown. The smooth red lines show the Gaussian fit of the distributions, the results of which are shown in table 4.3.

alpha gives a lower limit for the alpha quenching factor of 21.1.

The repeat sample of MIBP is also shown, for reference of the 1 cm muon sample. This was taken using the setup with PMTs 2 and 3, and consequently has poorer energy resolution, and lower light collection. Applying the same cuts to this pulse selection as to the previous selection gives the energy spectra shown in figure 4.17.

MIBP shows promise of being an excellent scintillator. The measurements showed had good event rates, and relatively good energy resolution in spite of the degradation due to PMT inefficiency. The strong selling point for this (previously untested) liquid is the excellent alpha/beta discrimination, with cuts at the same levels of purity and efficiency as the LSCs. This liquid, therefore, has a lot of potential as the base solvent of a LSC.

TMP

Although TMP produced scintillation light under incident radiation, it can not be described as a good scintillator. In the cases with moderate to low event rate, the

liquid responded with timely light emission, both from highly localised ionisation from the thorium alpha source, and from more spread out charge deposition from minimum ionising particles. In the case of the high rate (americium) alpha source however, the liquid did not respond as a good scintillator. The light output did not correspond to pulses with measurable properties, more to a high amplitude noise. Since the response of this liquid to a lower rate alpha source produced a measurable result, it is reasonable to suggest that the rate is the problem for this liquid. The observed light with the high rate source was consistent with pulse pileup from scintillation pulses, with additional after-pulsing.

The energy spectra for the measured sources with this liquid are shown in figure 4.18. The only cuts made were to remove non-pulses from the sample; $failflag_{PMT2} < 1$, $failflag_{PMT3} < 1$. The wavelengths of light output from this liquid are predominantly below 400 nm, which explains to an extent why the measured light output is very small for all of the sources. The energy spectra are fitted by a Landau distribution, for the same reasons as used for the liquid PXE.

Since there was no comparative alpha decay time spectra to dictate the cuts for the thorium source, the decay times of pulses from the thorium source itself were compared with the muon decay times. The muon decay time was fitted with a Gaussian with a mean value of $2.284 \pm 0.005 \mu s$ and standard deviation = 0.171. The thorium peak was fitted with a Gaussian with mean value = $2.308 \pm 0.003 \mu s$ and standard deviation = 0.1404. Since the thorium peak is predominantly composed of alpha particles, this suggests that finding an efficient cut would not have been possible even with a distinct alpha source, due to the large overlap of the two decay time fits.

The thorium spectrum in figure 4.18 is assumed to have a negligible contribution from the beta particles when calculating the energy resolutions. The energy spectra are fitted by a Landau distribution, for the same reasons as used for the liquid PXE. The thorium spectrum has a lower limit of energy resolution of 54%. This is due to hardware shaping the lower end of the spectrum. The muon peaks have resolution of 80% and 82%. The mean values of the muon peaks are expected to be at lower energies than in all the other liquids, since the depth of liquid in the dish was less as shown in table 4.1, as only a small amount of the liquid was available.

Since the data was taken with PMTs 2 and 3, this will have had a detrimental effect on the amount of light collected, and the energy spectrum.

Since the alpha peak of the thorium source is wide, and the peak position is compromised by the hardware trigger, it cannot be relied upon to give a 4.0 MeV

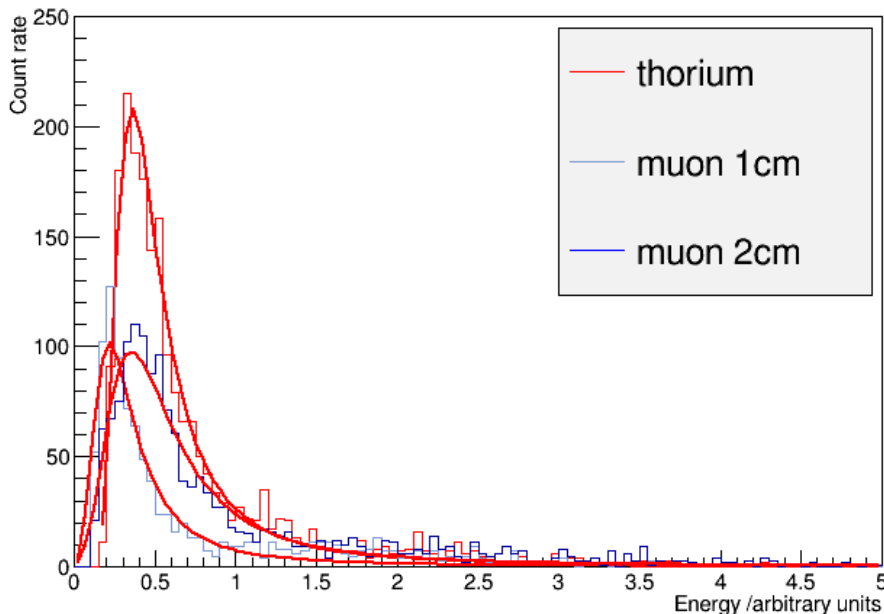


Figure 4.18: TMP, showing the thorium source (red), and the muons (light and dark blue). The smooth red lines show the Gaussian fit of the distributions, the results of which are shown in table 4.3.

peak with any accuracy. The alpha quenching factor, therefore, has not been calculated.

From the emission spectrum (shown in figure 4.6) it is clear that TMP has a very different molecular structure from the other liquids, and that its excitation is complex, as opposed to the simple, single excitation peak in DIN, PXE and MIBP. TMP, as discussed above, does not show appropriate properties in terms of event rate, energy resolution, or alpha/beta discrimination, and in addition, it cannot cope with high event rate sources. Therefore it would not make a good active medium for a scintillating liquid detector.

C5

The scintillation properties of Cyclopentane are more appropriate to scintillation counting than those of TMP, however, the absolute light yield for C5 appears to be much lower than the other liquids, in spite of the intensity of light emission being measured to be much higher than PXE and MIBP. The emission peak is at 350nm, in a wavelength range at which the PMT is less efficient, but the pulse amplitudes are smaller than in PXE, which has the peak emission wavelength around 300nm, i.e. lower than C5. Some of this can be attributed to the experimental setup - this

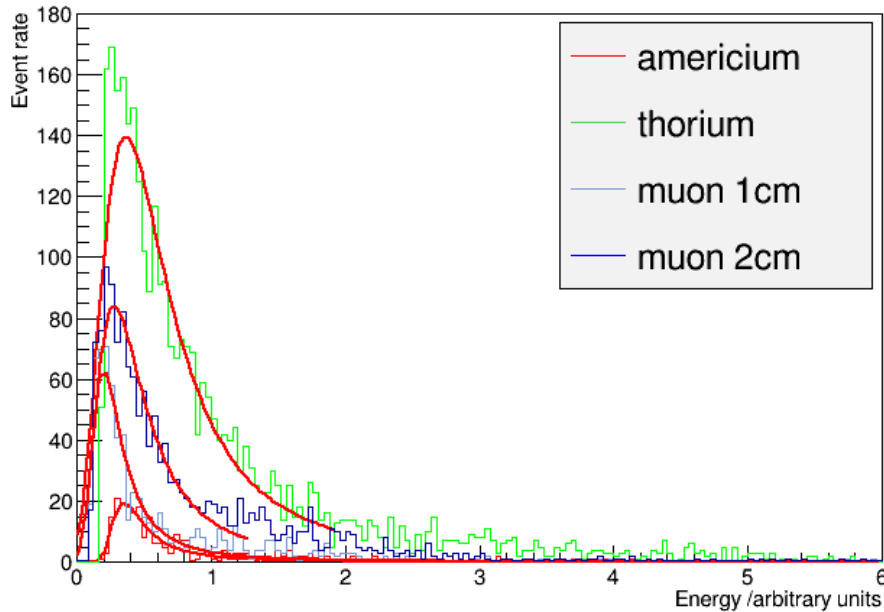


Figure 4.19: C5, showing the americium alpha (red), thorium source (dark green), and the muons (light and dark blue). The smooth red lines show the Gaussian fit of the distributions, the results of which are shown in table 4.3.

data was taken with PMTs 2 and 3. The effect is larger than can be attributed to this one cause, however.

The difference in pulse amplitude is particularly evident in the americium case; the event rate is much lower than all of the other liquids, which suggests that the peak was cut off by the hardware trigger, and is, in fact at lower energies than shown on the plot.

Since the lower light yield is also evident in the muon peaks, it cannot be attributed only to a larger value of alpha quenching.

Despite the small number of events overall, the peaks which are formed are fairly narrow, necessitating few cuts; only cutting out non-pulse samples, and a wide cut on position to cut out any random coincidences. The cuts were $failflag_{PMT2} < 1$, $failflag_{PMT3} < 1$, $|position_{PMT2} - position_{PMT3}| < 500$ ns.

The energy spectrum, shown in figure 4.19 shows all of the pulse populations fitted by Landau distributions, due to the hardware cutoff making a sharp lower edge to the distributions. This makes the distributions artificially narrow, giving lower limits to the energy resolutions. The americium (red) has an energy resolution of 47%, the thorium (green) 93%, and the muon peaks (light blue, blue) 74% and 87%, with the lower energy muons having a smaller width due to the low energy

cutoff.

The thorium spectrum shown in figure 4.19 is for the combined alpha and beta pulses. The decay times for the americium and muon samples, fit with Gaussians, had mean values of $2.36 \pm 0.01 \mu\text{s}$ and $2.34 \pm 0.01 \mu\text{s}$ respectively. Discrimination between these with a large enough efficiency was not possible, therefore a cut was not made on the thorium sample. The fit to the thorium sample has been made with a cut on the energy range, which gives a better fit than with the entire range, due to excluding any high energy betas in the sample.

The alpha quenching factor cannot be accurately calculated, since the position of the americium peak cannot be accurately determined.

Cyclopentane appears from the emission spectra to have the potential of being a good scintillator, with a high light yield, and relatively simple peak structure, however when exposed to ionising radiation, the amount of light observed was extremely low, compared to most other liquids. This can only partially be attributed to the efficiencies of the PMT. The difference between exposing the liquid to radioactive sources and an incident light source is the number of energy levels accessible to the electrons. The high intensity of light emission comes from energy states excited by energy of 4.13 eV and below. This suggests that there are higher energy states, which do not emit visible light, which are filled by the large amounts of energy deposited by the ionising radiation.

The lack of alpha/beta discrimination in this liquid, combined with the low event rate mean that this liquid has less potential to be a good liquid scintillator.

4.2 Charge Readout

The main proportion of this research concerned the investigation of charge transport properties of room temperature liquids. The choice of liquids was primarily motivated by the optical properties and “safe” to handle nature of the liquids. This section details the results relating to charge transport properties of the liquids DIN, PXE, MIPN, and MIBP, as well as DIN-based, PXE-based and LAB-based liquid scintillator cocktails. The charge transport properties of C5 and TMP were not investigated, but they have been shown [79] to be appropriate media for transporting charge.

4.2.1 Initial Experiences

The initial sets of data were taken using the wire proportional counter and gridded ionisation chamber (see sections 3.3 and 3.4 for detector details). In these experi-

Table 4.3: Summary table for optical measurements

Liquid	Source	Mean Energy	Standard Deviation	Energy Resolution (FWHM)	Alpha quenching factor
Ecoscint	Americium alpha	0.886 ± 0.005	0.268	71%	26.0
	Thorium alpha	1.54 ± 0.024	1.41	233%	
	Muon 1 cm	10.76 ± 0.03	0.816	18%	
	Muon 2 cm				
Optifluor	Americium alpha	0.683 ± 0.004	0.263	90%	34.9
	Thorium alpha	1.357 ± 0.022	1.342	233%	
	Muon 1 cm	10.518 ± 0.091	0.963	21%	
	Muon 2 cm				
DIN	Americium alpha	0.290 ± 0.003	0.065	53%	15.3
	Thorium alpha	0.112 ± 0.078	1.136	2388%	
	Muon 1 cm	2.857 ± 0.052	0.953	79%	
	Muon 2 cm	4.367 ± 0.069	1.360	73%	
PXE	Americium alpha	0.314 ± 0.001	0.0611	>46%	>4.15
	Thorium alpha	0.448 ± 0.003	0.146	>77%	
	Muon 1 cm	0.563 ± 0.001	0.214	>89.5%	
	Muon 2 cm	1.316 ± 0.021	0.414	>74.1%	
MIPN	Americium alpha	0.282 ± 0.002	0.0593	50%	16.2
	Thorium alpha	0.586 ± 0.003	0.173	>70%	
	Muon 1 cm	3.031 ± 0.044	1.100	85%	
	Muon 2 cm	4.588 ± 0.069	1.673	86%	
MIBP	Americium alpha	0.439 ± 0.003	0.112	60%	21.1
	Thorium alpha	1.06 ± 0.02	0.865	192%	
	Muon 1 cm*	4.90 ± 0.09	1.99	96%	
	Muon 2 cm	9.29 ± 0.01	1.67	42%	
TMP	Thorium alpha*	0.381 ± 0.005	0.0880	54%	
	Muon 1 cm*	0.236 ± 0.007	0.0803	80%	
	Muon 2 cm*	0.385 ± 0.008	0.134	82%	
C5	Americium alpha*	0.370 ± 0.001	0.0752	>47%	
	Thorium alpha*	0.406 ± 0.008	0.162	>93%	
	Muon 1 cm*	0.213 ± 0.006	0.0669	>74%	
	Muon 2 cm*	0.308 ± 0.008	0.114	>87%	

* indicates measurement with PMT 2 & 3 setup. All other measurements were taken with the PMT 1 & 2 setup.

ments, the data was taken a short time (the order of minutes) after applying the high voltage to the detector.

Figure 4.20a shows an example of the pulse shapes observed in DIN in the wire proportional counter. Figures 4.20b and 4.20c are examples of two pulse populations observed in the gridded ionisation chamber.

The data taken using the gridded ionisation chamber, for the liquids DIN,

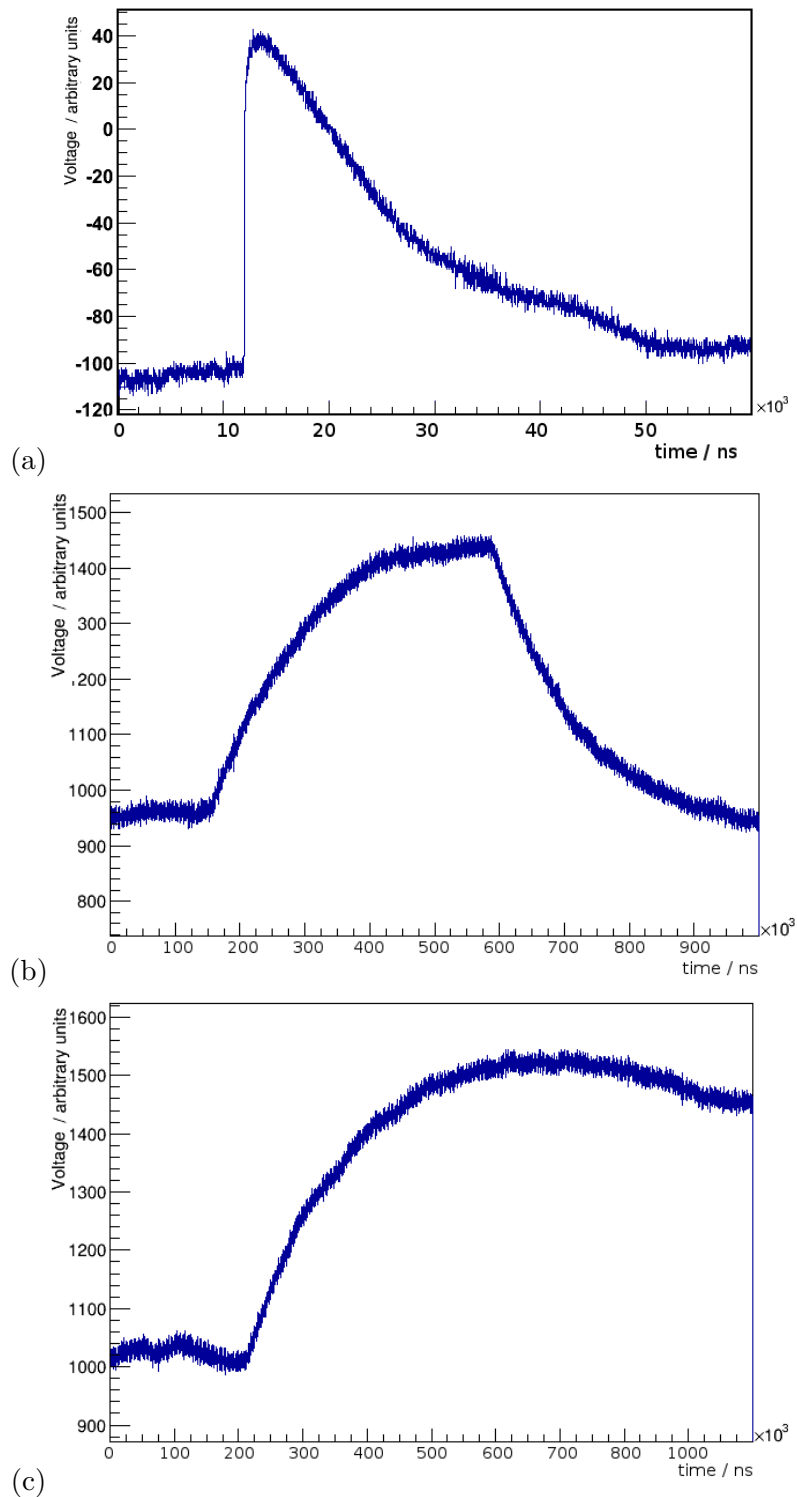


Figure 4.20: Pulse (a) is an example of a pulse shape typically observed in the DIN-filled wire proportional counter. Pulses (b) and (c) are two pulse populations observed in the DIN-filled gridded ionisation chamber. The time binning is 10 ns per bin for figure (a), and 5 ns per bin in (b) and (c).

MIPN, MIBP, and LAB, PXE, and DIN-based LSCs was presented in [2]. This data has been re-evaluated in the context of the subsequent measurements of a dark current in the liquids, analogous to that historically observed in dielectric liquids, as discussed in section 2.4.2.

The raw data taken with these liquids contained many background pulse shape populations, which have possible relevance to the dark current subsequently identified. This will be discussed later on in this chapter.

Data was taken at a range of electric field values with the initial measurement taken at the highest voltage required, and subsequent measurements taken after decreasing the high voltage. The liquids were found to be more stable during measurements with decreasing electric field, and gave more reproduceable results than taking measurements starting with the lowest voltage, hence the decision to make the measurements in this order.

This could support the hypothesis of a dark current being present in the liquids. Considering equation 2.28 for this situation, the impurities present in the liquid would cause a higher current initially for an application of electric field, but would decrease as a function of time. As the electric field is decreased, the rate of dark current will decrease; both due to increased time, and due to the change of the electric field. By contrast, increasing the electric field will cause both an increase in the dark current, due to the molecular dissociation being stronger at higher fields, and a change in the dark current component attributed to impurities, for which the relationship to E field and time is not well understood. The more stable behaviour of the detector in this configuration is therefore compatible with theoretical predictions.

4.2.2 Event Rates

The total event rate for each liquid is presented, with cuts made only to remove “failed pulses”, namely noise triggering, (for a full explanation, see section 3.9) but with no further pulse shape discrimination. The number of pulses present gives an indication of the dark current as a function of drift field. The values of electric field quoted are for the region of the detector for which anode pulses are detected: the anode-grid region.

In this instance DIN was the only solvent for which samples were available with and without fluors present in the liquid. The event rates are shown in figure 4.21.

In both of the liquids, the event rate seems to plateau around an electric field of 4.5 kVcm^{-1} , however there is a difference of roughly a factor of two between the

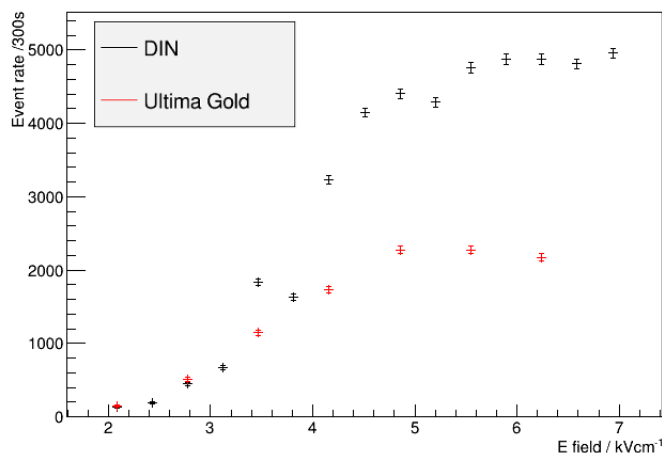


Figure 4.21: Event rate as a function of electric field in DIN solvent (black) and Ultima Gold F cocktail (red).

event rates. For fields below 3.5 kVcm^{-1} , the rates are very similar, however. For higher electric fields, it appears that the presence of fluors in the liquid is detrimental to charge transport. The difference between the two liquids is further examined and discussed in section 4.2.3, where the current has been measured in both liquids.

The event rates for the solvents MIPN and MIBP are shown in figures 4.22 and 4.23 respectively. MIPN has comparatively little pulse activity at drift fields below 6 kVcm^{-1} . The shoulder at the higher electric fields measured may be leading up to a plateau at around an event rate of 3500 pulses. Alternatively, the rate may not plateau, and the shoulder may be leading up to the breakdown of the liquid. The electric field was limited to this level by the output range of the high voltage power supply.

The event rate for MIBP is likewise at lower event rates than DIN for the electric fields lower than 5 kVcm^{-1} , although the rate sharply increases between 5 and 6 kVcm^{-1} , after which point the event rate is higher than all of the other liquids measured.

LAB was only obtained as a scintillation cocktail, Optifluor O. It was found that the liquid could not sustain a high voltage, and the lead-up to breakdown at voltages above 5 kV can be seen in the total event rate, shown in figure 4.24. The dark current in LAB has also been measured, and is discussed in section 4.2.3.

The dielectric strength of this liquid is too poor for it to be considered as the active medium of any detector requiring high electric fields. Any characterisation of the mobility of the liquid was impossible, since the electric fields required to transport charge were not sustainable. Linking back to the historical theoretical

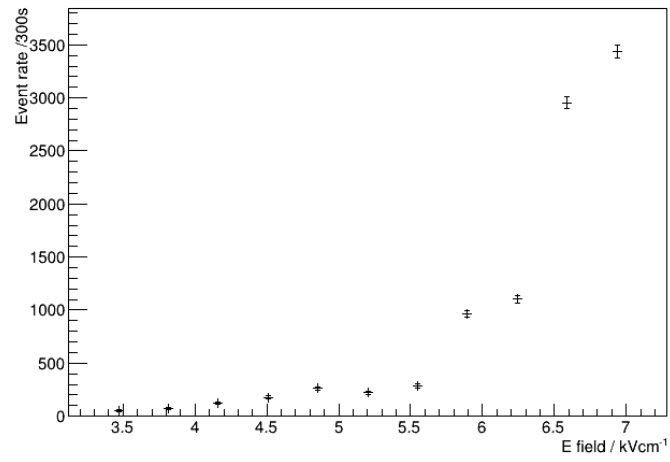


Figure 4.22: Event rate as a function of electric field in MIPN solvent.

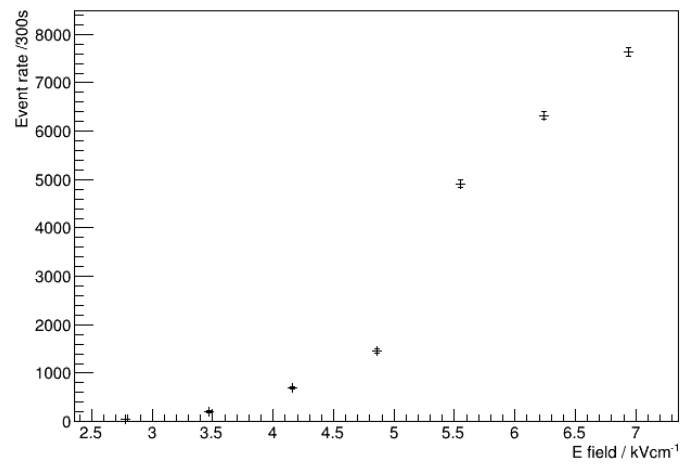


Figure 4.23: Event rate as a function of electric field in MIBP solvent.

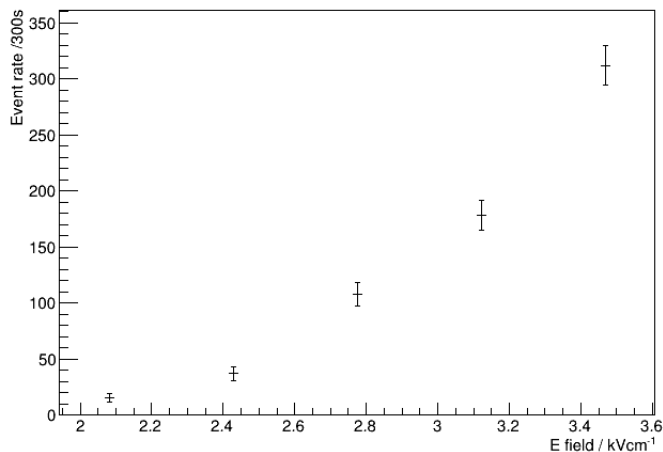


Figure 4.24: Total event rate as a function of electric field in LAB scintillator cocktail.

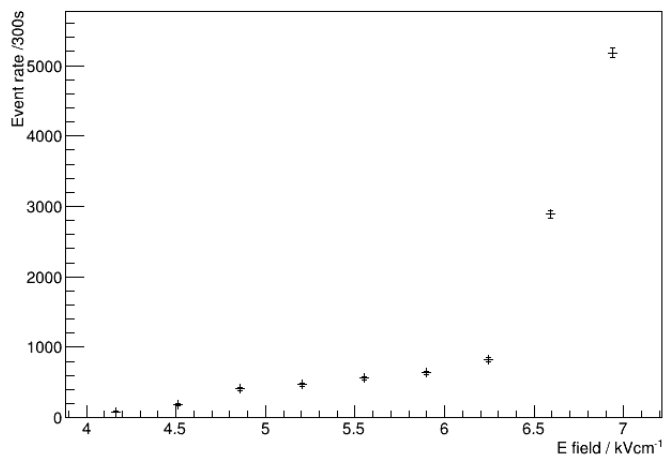


Figure 4.25: The event rate as a function of electric field in Ecoscint O.

work on charge transport in hydrocarbons [78], the shape of the LAB molecules (as shown in table 2.5) is a long molecular chain, which is the shape synonymous with low mobility liquids. The sampling for the dataset presented in figure 4.24 could be considered to be triggering in noise, as the data samples present show no consistent pulse structure, unlike the other data samples.

At the time of data-taking, PXE was obtained only as a scintillation cocktail, Ecoscint O. This liquid also showed signs of breakdown at high voltages, at fields of 7 kVcm^{-1} and above. The event rate is shown in figure 4.25, and shows a low initial rate, with a large increase in event rate above 6.5 kVcm^{-1} .

Subsequent analysis of PXE and PXE-based liquids shows a high initial dark

current, followed by a decrease over time. The pulses observed at high electric fields in this instance considered to be the precursors to breakdown could in fact be the high initial dark current. This is further discussed in section 4.2.3.

The liquid PXE was subsequently sourced as a solvent, without scintillation fluors, and subsequent measurements were taken with this liquid, using much higher electric fields, without signs of breakdown. This suggests that the presence of fluors may be lowering the dielectric strength of the liquid.

Drift speed measurements

In reference [2], electron drift speed measurements were presented for the liquids DIN, MIPN and MIBP. The drift speed was calculated by selecting a population of pulses, fitting the rise time distribution with a Landau function, and calculating the speed across the 7 mm anode-grid distance in the gridded ionisation chamber. The selected population of pulses is shown in figure 4.20(b). Pulses belonging to this population were found to be present in all of the data. Using cut-based pulse selection required a large number of cuts, however, and produced an inefficient, but pure sample.

In order to select a pure sample more efficiently, and thereby make improved measurements, the data taken in DIN has been returned to using a pulse fitter (as described in section 3.9). The cut-based analysis is presented first, followed by the pulse fitter analysis.

Despite this data being presented as a drift speed measurement, it is, in retrospect a flawed measurement, in light of the dark current present in the detector. A proportion of the pulses at least must belong to the dark current, and therefore have no well-defined start point. Although there is clearly charge moving in the detector, the signal induced by said charge cannot be used to make measurements of the drift speed. The data and cuts are nevertheless presented as in [2] for completeness.

The drift speed in MIBP as a function of electric field is shown in figure 4.26. The cuts made to select the desired pulse population are the following; *failflag*<1, *amplitude*>0.02, *position*<325 μ s, *onset*>100 μ s, *decaytime*<175 μ s. These cuts are applied to the rise time data histogram at each electric field value. For reference, all of the pulse parameters are summarised in table 3.5.

The first cut gets rid of data samples which contain nothing with a pulse structure, the second of any baseline triggered pulses with low amplitude. The cuts on onset, position and decay time are those which decrease the efficiency of the pulse selection. They ensure that the pulse falls with the true onset within the data window, and the fast decay time characteristic of the pulse shape is measurable,

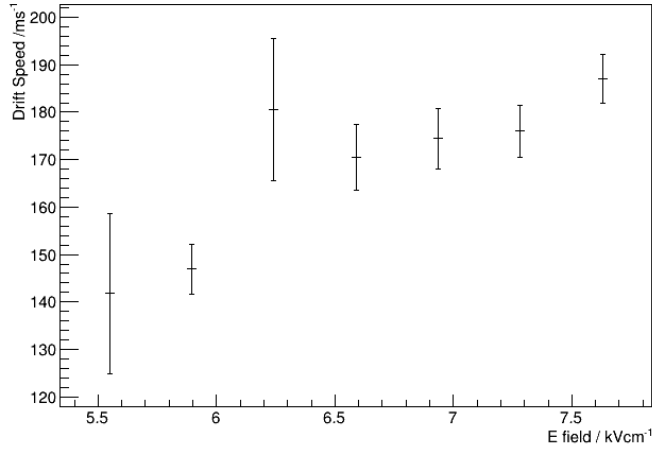


Figure 4.26: Drift speed as a function of electric field, in MIBP.

rather than an artificially short decay time from a pulse at a late position in the data sample.

The drift speed increases with field strength up to an electric field of around 6.2 kVcm^{-1} , where it levels off, to a drift speed of around 180 ms^{-1} .

The drift speed in MIPN as a function of electric field is shown in figure 4.27. The cuts made for this pulse selection were the following; *failflag* <1 , *amplitude* >0.04 , *position* $<625 \mu\text{s}$, *onset* $>100 \mu\text{s}$, *decaytime* $<375 \mu\text{s}$. The justification for these cuts is identical to the MIBP case, as described above.

The drift speed increases as a function of electric field, although the rate of increase is nonlinear, with the largest increase at fields above 6 kVcm^{-1} . At an electric field of 6.93 kVcm^{-1} , the drift speed has been measured to be $143 \pm 9 \text{ ms}^{-1}$.

The drift speed in DIN as a function of electric field is shown in figure 4.28. The cuts applied to select this pulse population were the following; *failflag* <1 , *amplitude* >0.06 , *position* $<700 \mu\text{s}$, *decaytime* $<300 \mu\text{s}$. The justifications for the cuts are identical to the cases of the other two liquids.

The drift speed in DIN appears to increase roughly linearly over the range of $5\text{-}7 \text{ kVcm}^{-1}$. In an electric field of 6.93 kVcm^{-1} , the drift speed is $98 \pm 2 \text{ ms}^{-1}$.

In all of the liquids the absolute rate of the pulse selection is much lower than the expected rate of the alpha source present in the detector. The activity of the source is 37 kBq , and for an example liquid of DIN, the total pulse rate at the highest electric fields corresponding to roughly 17 Hz , without accounting for pulse pileup due to the sampling window. With this full event rate, the efficiency of the detector would be around 0.05% , and with a pulse selection cut, the rates were roughly an order of magnitude lower, giving a correspondingly lower efficiency.

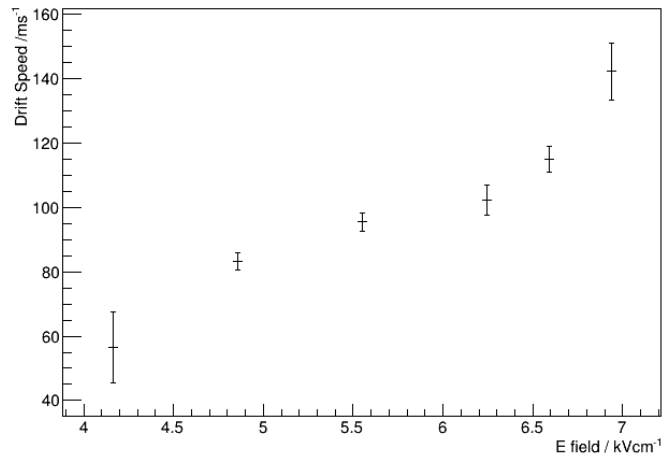


Figure 4.27: Drift speed as a function of electric field, in MIPN.

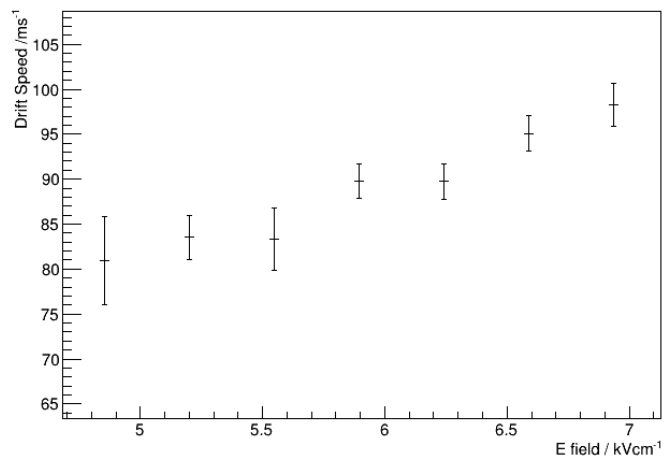


Figure 4.28: Drift speed as a function of drift field, in DIN.

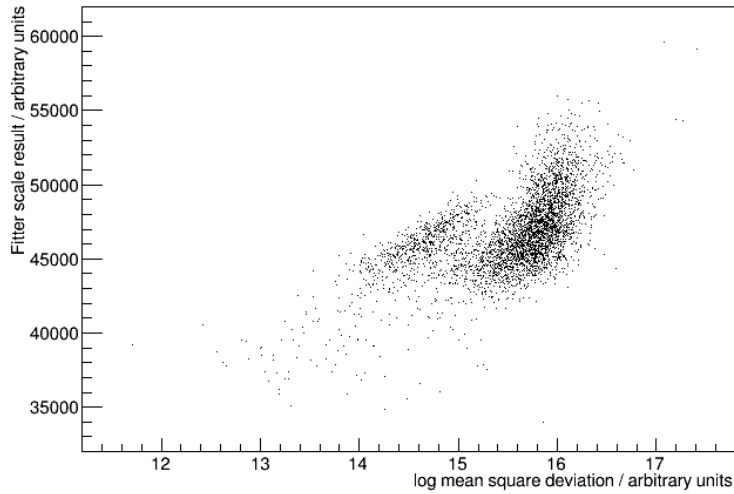


Figure 4.29: A scatter plot of two pulse fitter parameters, showing two distinct populations in a data sample taken with 3.2 kVcm^{-1} drift field.

In light of further experiments, discussed in section 4.2.3, it is suggested that the charge being measured with this detector was in fact, not the alpha source, but was due to a dark current in the liquid itself.

The DIN data was revisited using a pulse fitter analysis, to try to improve on the efficiency of the cut, and examine the different pulses present in the distribution. Two prevalent pulse populations observed in the liquid were selected, examples of which are shown in figures 4.20b and c. A pulse template was created from a small, hand selected sub-group of each these types of pulses, as described in section 3.9. These pulse templates were then each applied to the full data set in turn.

The *scalerresult* and the *logms* parameters, fully described in section 3.9 were plotted against each other, to give a visible representation of how the different scale factors grouped against the deviation from the template. For the pulse type shown in 4.20b, there are two consistently distinguishable populations in the fit. For the lower drift field data sets, these populations are visually distinguishable in the scatter plots, as shown in figure 4.29. For the higher voltages, the populations are less distinguishable from the scatter plot, but the difference in density of points is clearly evident from contour plots, as is shown in figure 4.30.

These plots show that a cut at a value of 15.2 units on the log mean square deviation scale would separate the populations. Pulses below this value, namely pulses more similar to the template, are selected. Using this cut, combined with a cut to exclude failed pulses (as described above), the efficiency is much better than in the purely parameter cut-based selection. An example of this is shown in figure

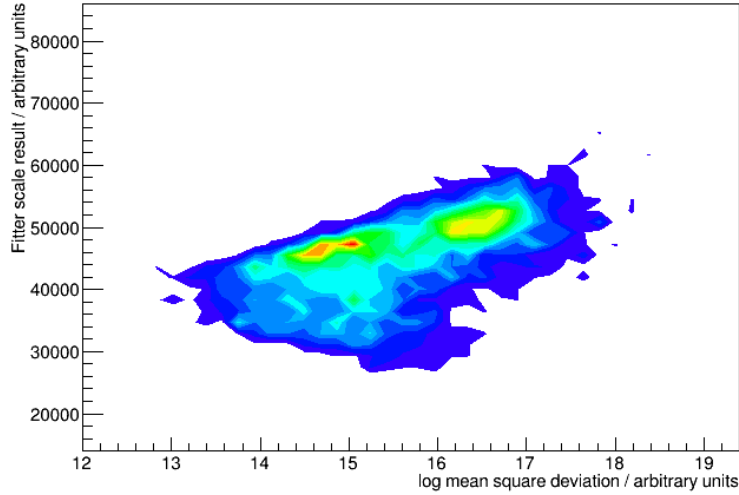


Figure 4.30: A contour plot of two pulse fitter parameters, showing two populations which are not very well separated, in a data sample taken with 5.1 kVcm^{-1} drift field.

4.31, for a drift field of 3.2 kVcm^{-1} . The blue line represents the full, uncut sample (4213 pulses), the green shows the pulsefitter selected pulses (920), and the red shows the pulses selected using the previous data cuts (46). The larger selection of pulses allows for a much better fit, whilst discriminating against other pulse populations.

This cut, $failflag < 1$, $logms < 15.2$ was applied to each of the data sets, and the rise time data was fitted with a Landau distribution. This is shown in figure 4.32, as a function of electric field. The drift speed measurements using a parameter-based fit are also shown, as well as the Landau distribution fit to an uncut sample, are shown in black. For electric fields up to 5.4 kVcm^{-1} the fitter-based pulse selection has similar mean values to the parameter-based pulse selection, but smaller errors. This means it can be considered to be selecting the same pulses, with a high purity.

For drift fields above 5.4 kVcm^{-1} , the fitter-based pulses are much closer to the uncut sample. This supports the visual evidence that the pulse distributions are not well separated by the pulse fitter at higher electric field values, and explains why the selection cut made little difference to the pulse parameters, namely risetime. In order to select the correct pulse population with high purity for the entire range of electric fields, more stringent cuts would have to be applied. Since it transpires that there is ultimately little we can learn from a clean spectrum of this data, these extra cuts have not been implemented.

The second filter pulse class (as shown in figure 4.20c) yields much less in terms of selection of pulse population. The filter response was much more homo-

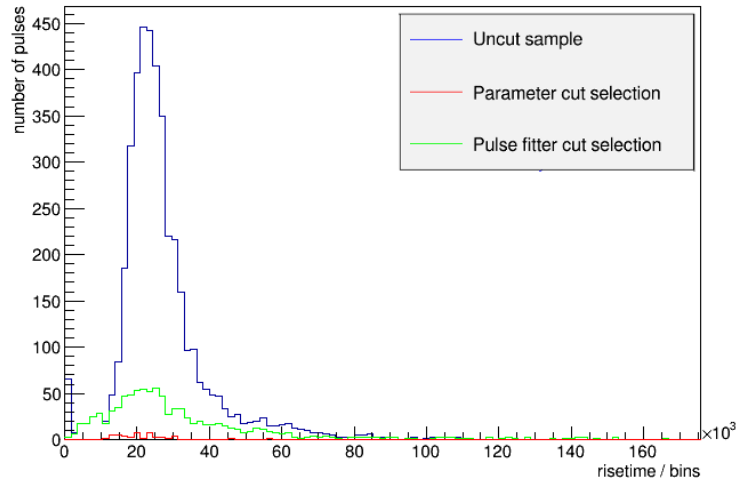


Figure 4.31: A histogram of the rise time pulse parameter at a drift field of 3.2 kVcm^{-1} , showing histograms of the uncut sample (blue), the pulse fitter-based cut selection (green), and the parameter-based cut selection (red). There are 5 ns per timing bin.

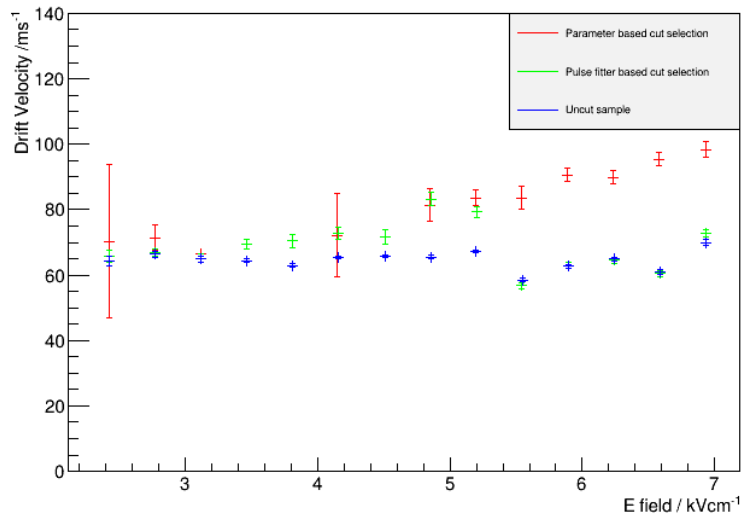


Figure 4.32: The drift speed in DIN as a function of electric field, showing the uncut sample (blue), the pulse fitter-based cut selection (green), and the parameter-based cut selection (red).

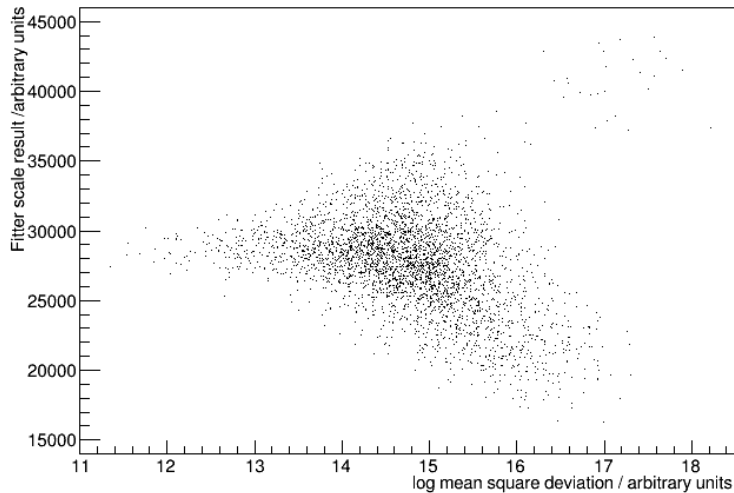


Figure 4.33: A scatter plot of two pulse fitter parameters, which shows a concentration of pulses, but no distinct populations, in a sample taken with 4.6 kVcm^{-1} drift field.

geneous throughout the range of voltages, and therefore no additional cutting has been made using this tool. An example of the scatter plot from this pulse filter is shown in figure 4.33.

The “drift speed” measurements in this section are presented for completeness, and in spite of not having value in terms of determining the charge transport speed of the medium, they do show the variation in risetime of background pulses with electric field. The changes present in the sample provide strong supporting evidence for the dark current discussed in the following section. A combination of these data gives more of an insight into how the liquids behave in detectors of different types, namely the pulse shapes in the uniform fields of an ionisation chamber compared to the high field regions of a MWPC.

4.2.3 Dark Current

The dark current discussed in section 2.4.2, which is a characteristic of liquid hydrocarbons examined in references [81],[84],[83],[85] has been observed in several of the liquids, both as slow current measurement, and as fast pulses. A high voltage was applied to the detectors, and measurements were taken over the course of several days in order to observe the changes in detector behaviour.

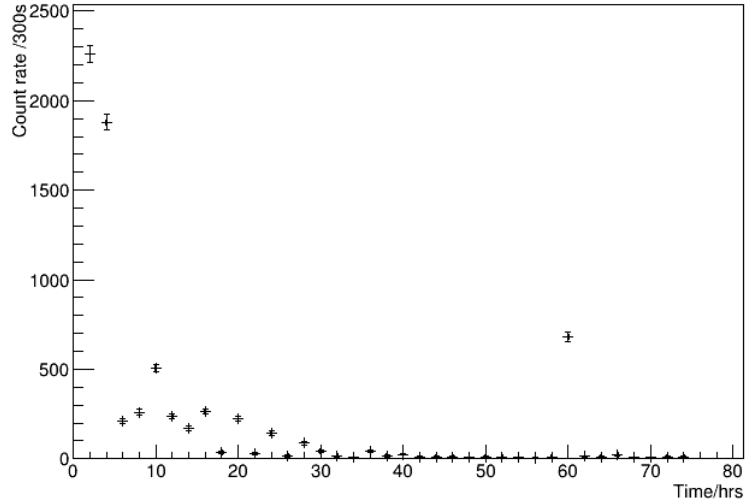


Figure 4.34: Background pulse rate in DIN at a field of 5 kVcm^{-1} .

Fast Pulse measurements

The dark current was first measured in the liquids tested in this thesis using the MWPC, described in section 3.5. The liquids tested were DIN and PXE, which have both been shown to exhibit time-dependent behaviour.

The important difference between these measurements and those made previously is that the historical observations were all using detectors designed to measure a continuous current, whereas the MWPC is designed to measure fast transients. The ability to resolve pulses gives new and interesting opportunities to identify the cause of different pulse populations, using pulse shape analysis. This analysis primarily concerns the observed changes in pulse populations over time, for selected data runs.

Figure 4.34 shows the total event rate with no cuts in DIN as a function of time. This data was taken with no source present in the detector, at drift fields of 5 kVcm^{-1} , with 300s sampling every 2 hours. The total number of pulses present decreases over the course of roughly a day, and flattens off, apart from occasional bursts of spurious pulses.

From this data, it is evident that the measurements taken with the gridded ionisation chamber, shown in section 4.2 which were taken within 5 minutes of changing the high voltage, could contain a large amount of pulses which did not correspond to the source.

Figure 4.35 shows the total rate of pulses in PXE with a 300 Bq $\text{Pb210 } \beta$ source in the detector, at a drift voltage of 2.5 kVcm^{-1} , sampling hourly for 300s.

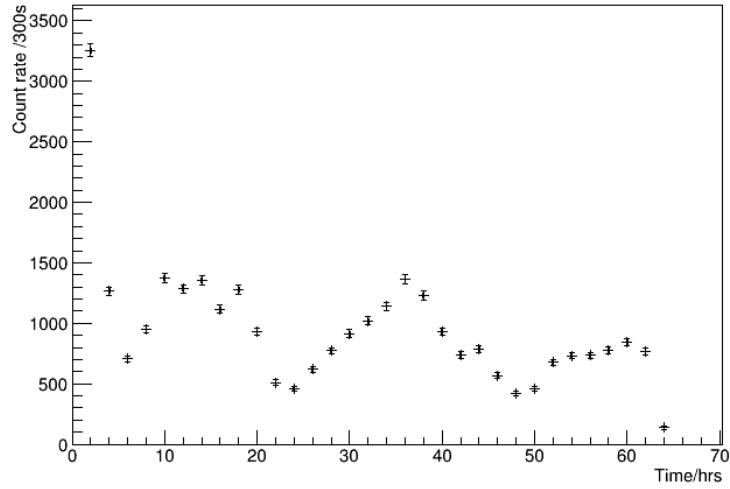


Figure 4.35: Total PXE event rate at 2.5 kVcm^{-1} , with no cuts.

The total event rate decreases, as well as exhibiting a clear temperature dependence; the oscillation has a period of 24 hours. Not only does the total event rate decrease as a function of time, but the numerous pulse populations present in the detector change differently over time, supporting the theory that the background current is caused by multiple sources. The observation of pulse populations which vary over a long timescale fits in well with the observations in the historical papers concerning dark current.

Figures 4.36 and 4.37 show the rates of two distinct pulse classes taken from figure 4.35. The graph in figure 4.36 shows the rate of pulses of shape shown. The cuts made to select this pulse population were simply on the baseline of the pulses: $baseline > 0.4$, which selected this population of pulses whose rise time was sufficiently slow that the sampling window did not contain the full rise time of the pulse (hence the high baseline calculation from the initial pulse bins). The shape of the pulse distribution in figure 4.36 is very different to the total rate. These pulses have a very slow rise time, which suggests that they have extremely low mobility, and could correspond to the motion of low mobility impurities. The disappearance of impurities as a function of time was investigated in [84]. Indeed, there is discussion of using a high electric field to clean the liquid Tetramethylsilane (TMS).

Figure 4.37 conversely shows a selection of pulses with much faster rise time, selected using the following cuts; $baseline < 0.4$, $risetime < 300 \text{ ns}$. The baseline cut removes the previous population of pulses, and the selection characteristic of this pulse population is the fast rise time.

This pulse population clearly exhibits the temperature-dependent property

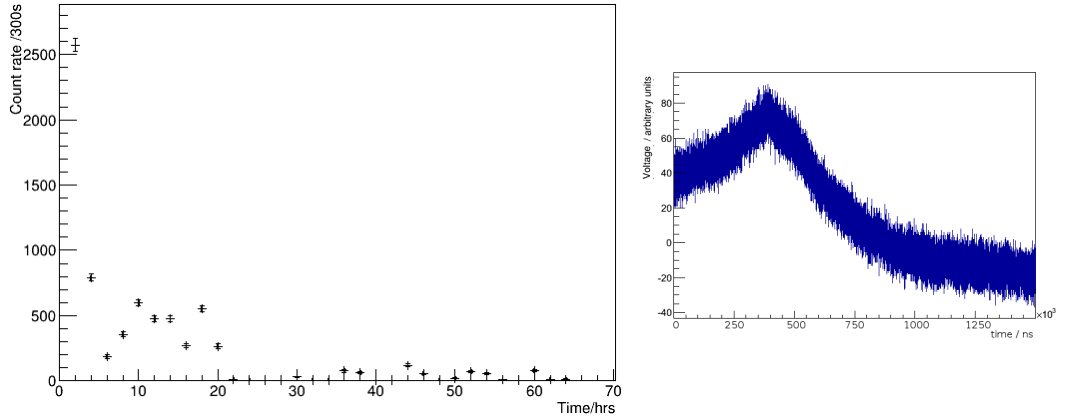


Figure 4.36: Left: Event rate of cut selection at 2.5 kVcm^{-1} . Right: Selected pulse type, with sampling window of $1500 \mu\text{s}$, with 5 ns per time bin.

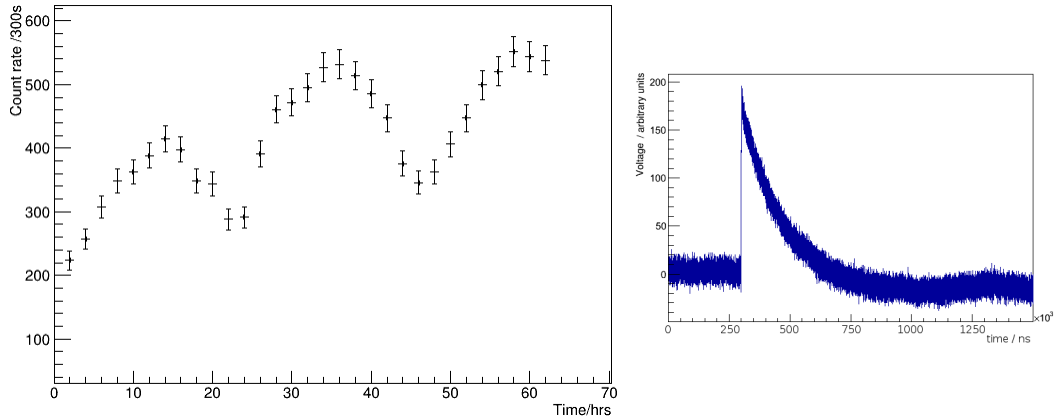


Figure 4.37: Left: Event rate of cut selection at 2.5 kVcm^{-1} . Right: Selected pulse type, with sampling window of $1500 \mu\text{s}$, with 5 ns per time bin .

of the liquid. The rate does not decrease as a function of time. It appears to increase, but since the behaviour of the detector during the first 10 hours was deteriorated due to the slow pulses, it is possible that the rate stayed constant. This is consistent with observation of charges moving because of molecular dissociation. The fast pulse rise time suggests that the effect is happening close to the wire, where the electric fields are highest. This also points towards the bubble effect hypothesis (as discussed in 2.4.2). A constant event rate could also suggest the observation of the β source, but the event rate suggests that the source is not visible at these field strengths.

Figure 4.38 shows data taken in PXE, with the Pb210 β source present in the detector, and a drift field of 11 kVcm^{-1} . The sampling was hourly, for 120 s.

At higher drift fields, as in figure 4.38, the pulse event rate decreases as a

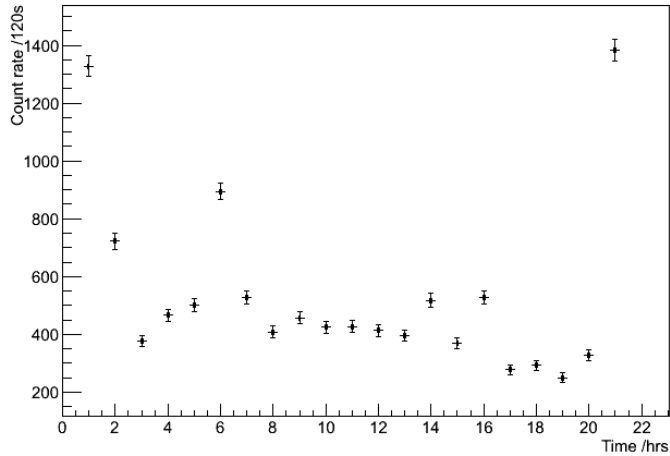


Figure 4.38: Total event rate PXE at 11 kVcm^{-1} .

function of time, although it seems to plateau more quickly.

The pulse population shown in figure 4.39 was selected with the cuts: *fail-flag* < 1, *amplitude* > 6, which removed any non-pulse samples, and selected large amplitude pulses.

The samples presented with the pulse shape selections show clear evidence of a dark current in the two liquids tested, PXE and DIN. The variation in pulse shape as a function of electric field suggests that pulse shape analysis gives more information than the previous current measurements, which gives stronger evidence to support the causes of the dark current.

The slow pulse population, which has been shown to disappear over the first few hours of data taking, could correspond to the impurities present in each sample, which will move extremely slowly, hence the slow rise time. The amount of time taken for this population to flatten off in rate decreases as a function of electric field, which again, points to a faster “cleaning” of the detector.

This pulse population could also correspond to the slow rise time pulses observed in the gridded ionisation chamber (as shown in figure 4.20c). Since the gridded ionisation chamber data was taken immediately after a change in electric field, one would expect a large proportion of pulses of the same type as observed in the first MWPC measurement, taken immediately after switching on the electric field. The pulse shapes observed in the two detectors are different due to the detector type, and therefore the potentials which the charge is experiencing. Particularly at higher drift field values, there are many of this pulse population present in the gridded ionisation chamber.

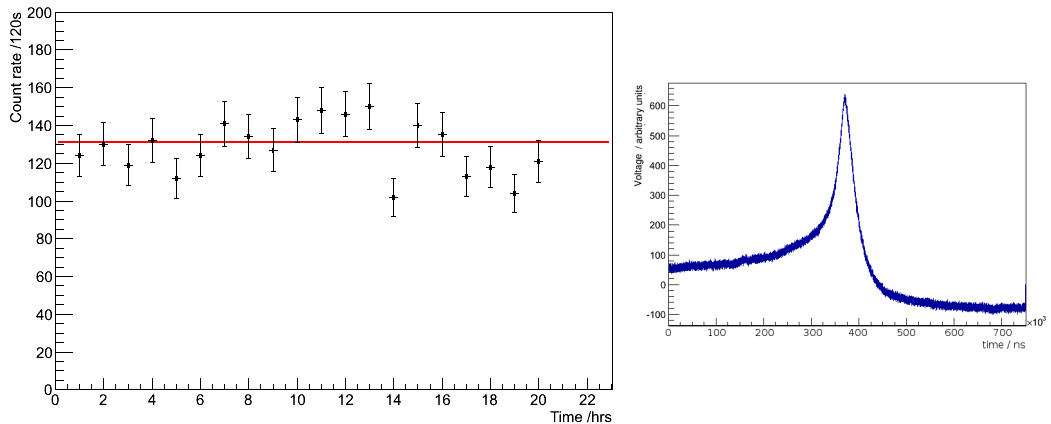


Figure 4.39: Left: Event rate of cut selection at 11 kVcm^{-1} , fit with a straight line at a rate of 131 events. Right: Selected pulse type, with sampling window of $750 \mu\text{s}$, with 5 ns per time bin.

In order to ascertain whether the origin of the slow pulses does correspond to the motion of impurities, experiments could be carried out to insert impurities into the liquid in a controlled way. The pulse populations could then be monitored as a function of the amount of impurities in the detector. This is beyond the scope of this thesis.

There is some evidence

The comparison of fast pulse shapes also provides some evidence against one of the theories for the source of dark current. The bubble hypothesis is that a source of the dark current is surface imperfections at the electrodes. Evidence for this would be a decrease in the rise time of pulses as a function of electric field, since the stronger electric fields in immediate proximity to the anode wire would cause a faster drift speed. Contrary to this, the fast pulses observed in PXE have an increase in average pulse rise time, from $248.5 \pm 0.2 \text{ ns}$ to $25.75 \pm 0.05 \mu\text{s}$. This fits with the theory of molecular dissociation, as discussed earlier. This evidence is somewhat inconclusive, since the event rate for this fast pulse population must be constant to support the theory of molecular dissociation. Figure 4.37 does not conclusively show a constant rate, therefore it would be necessary to take data over a longer time period to demonstrate conclusive support for this theory.

The large bursts of spurious pulses appearing on several occasions in each data sample remain unexplained. This is further discussed with respect to the current measurements in the following section.

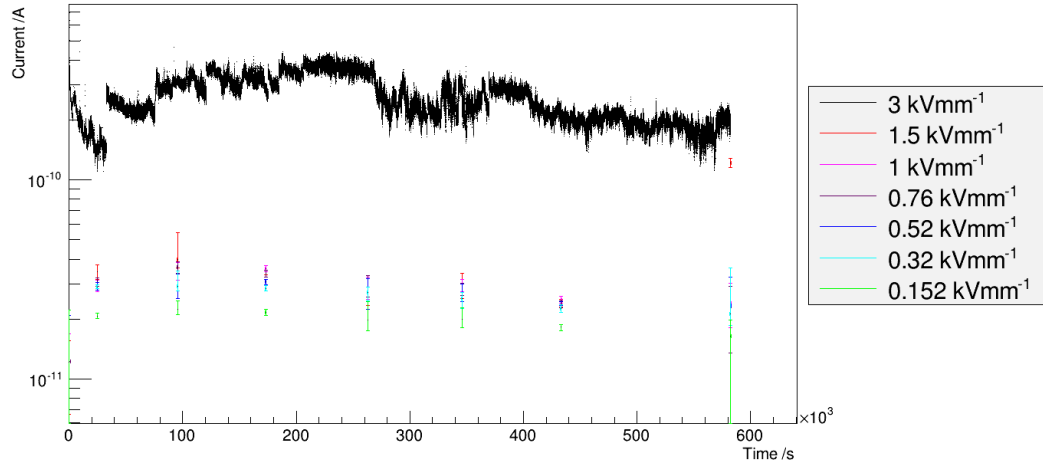


Figure 4.40: Dark current in DIN as a function of time and electric field.

Current measurements

In addition to the fast transients observed in the MWPC, dark current measurements were taken in PXE, DIN, Optifluor O and Ultima Gold over a period of days. This allows for more direct comparison of the dark current in these liquids to the historic data taken in other liquids.

Data was taken at seven different electric field strengths, listed in table 3.4. The continuous data sampling was using the highest drift field in the detector, of 3 kVmm^{-1} . The point measurements are at the 6 lower drift field strengths.

The data taken in both DIN and the DIN-based scintillator cocktail Ultima Gold, both show a predominantly constant current as a function of time, for all of the electric fields measured. The data is shown in figures 4.40 and 4.41.

The continuous current measurement, at an electric field of 3 kVcm^{-1} , has a much higher current than the lower electric fields measured. The data shown in figures 4.40 and 4.41 were fit with flat straight lines, giving the average current over time. Figure 4.42 shows the average current plotted against the electric field for both liquids.

It is evident that the current does not increase linearly with electric field. The dark current reaches a plateau at roughly 0.3 kVmm^{-1} . The continuous data point at 3 kVmm^{-1} has a significantly higher current than the lower drift fields. This suggests that there is a threshold above which the current increases, a shape common to both liquids.

Similarly to the measurements taken in the gridded ionisation chamber, the current for DIN and Ultima Gold is similar at low electric field strengths, but for

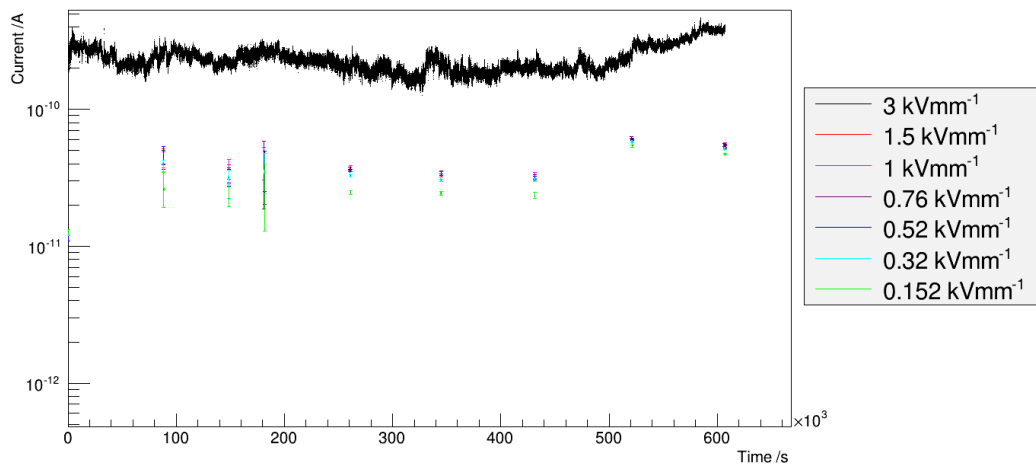


Figure 4.41: Dark current in Ultima Gold F as a function of time and electric field.

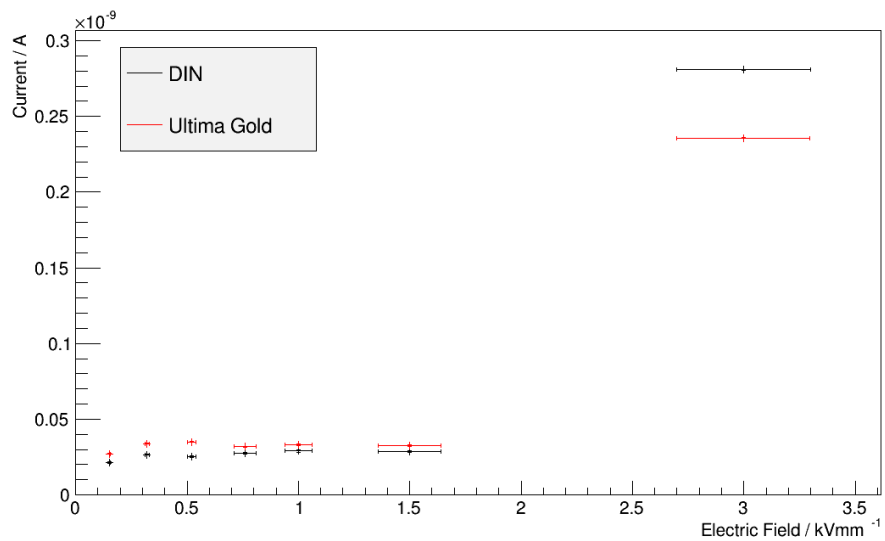


Figure 4.42: The dark current as a function of drift field in DIN (black) and Ultima Gold (red).

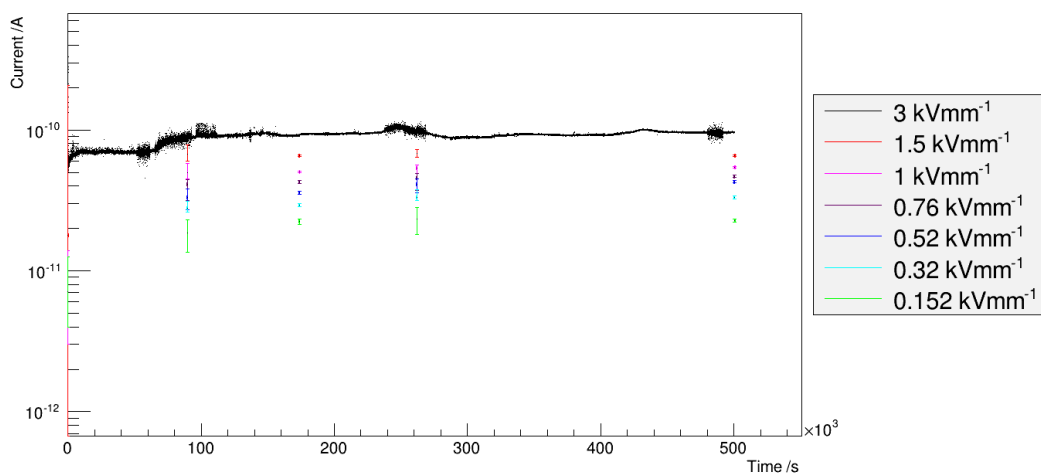


Figure 4.43: Dark current in Optifluor O as a function of time and electric field.

high electric fields, there is a higher current in DIN. This supports the hypothesis that fluors are detrimental to charge transport in liquids.

A dark current is also measured in Optifluor O, the LAB-based liquid scintillator. In this liquid, the current remained constant as a function of time, with much less variation than in the DIN-based liquids. Each drift field had very little variation over time. The dark current as a function of time is shown in figure 4.43, with the colours of the discrete data points representing the current measurements at lower electric fields.

The variation as a function of drift field is completely different to that in DIN. Figure 4.44 shows the straight line fit values of current plotted against the drift field. The increase in current with drift field seems to be roughly linear for the drift fields measured. This supports earlier evidence of the liquid having a low dielectric strength.

The absolute values of the current in LAB are roughly an order of magnitude lower than those observed in DIN. This, again ties in well with the liquid having a lower mobility due to the long, chain-like molecular structure, as well as the possible suppressing effect of the equally lengthly fluor molecules on the current.

Phenyl xylol ethane behaves very differently to the other liquids measured, in that the dark current varies as a function of time. Although it is more chemically similar to DIN, this puts the liquid in a more similar class of liquids to TMS and n-heptane whose dark current has been shown to decrease as a function of time (as shown in figure 2.16). The dark current seems to change across a similar timescale to these liquids; comparing the main features of figures 4.45 and 2.16, there is a

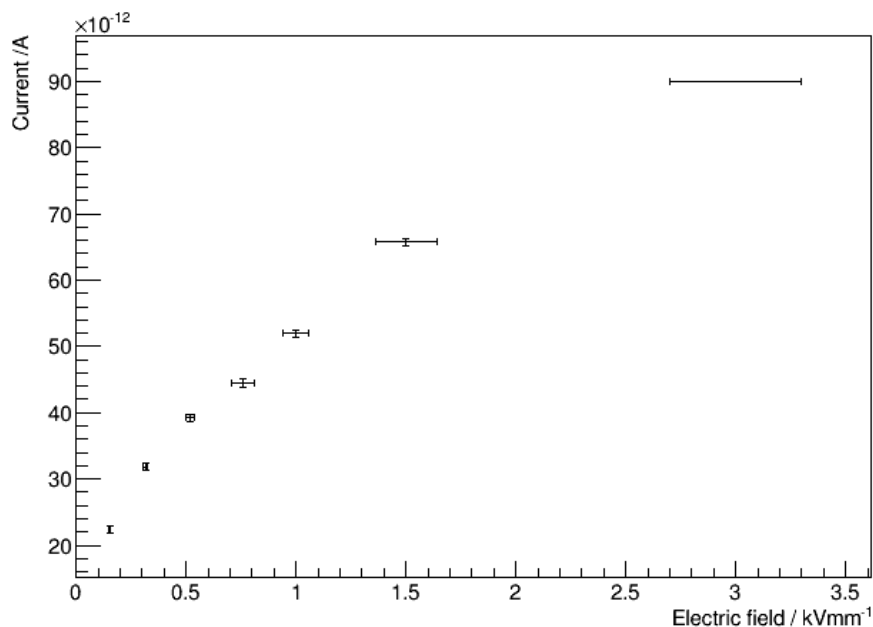


Figure 4.44: The dark current as a function of electric field for Optifluor O.

sharp drop in current over the first day, and the current levels off over the course of the proceeding 6 days (N.B. 6×10^5 s \sim 7 days).

The change in current over time also has an electric field dependence. The variation over time for electric fields of 1 kVmm^{-1} and above (red, magenta) follows the basic shape of the continuous measurement, with a decrease over time but with a lower initial current, and higher final current. This suggests that the dark current is affected by mobility of the liquid. Moving charges in lower electric fields move more slowly, therefore the net decrease in current over time is less. This is supported by the measurements taken at electric fields of between 0.32 kVmm^{-1} and 0.76 kVmm^{-1} (purple, blue), where the amount of charge remains roughly constant as a function of time. At the lowest electric fields (cyan, green), the current is comparable with the background reading without electric field, which suggests that there is a threshold below which there is little or no dark current.

In addition to the change in rate over time, there are more features on the continuous dark current measurement in PXE. There are spikes in the current rate throughout the entire measurement. These vary in amplitude, not decreasing as a function of time. This was initially thought to be a detector effect in the measurement, but comparing the behaviour of the detector in PXE and all of the other liquids, the current measurements taken in the three other liquids have much smaller variations per unit time than PXE. Therefore it is thought to be a feature of the

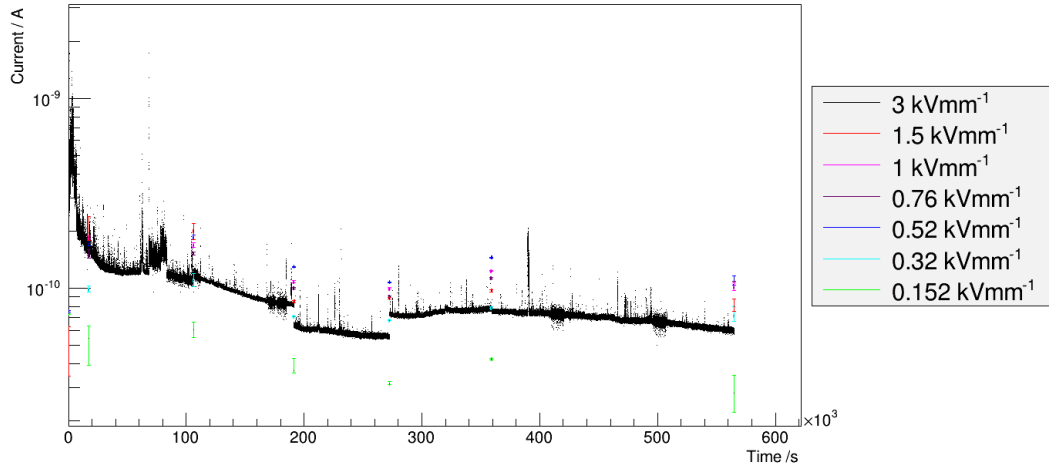


Figure 4.45: Dark current in PXE as a function of time and electric field..

liquid, suggesting instability under electrical stress. This also corresponds to the spurious pulses observed in the MWPC data.

This dark current data can be compared to the pulse measurements taken in PXE at a drift field of 11 kVcm^{-1} , as shown in figure 4.38. The magenta points, at a drift field of 1 kVmm^{-1} are the closest in drift field strength to this data. For the MWPC data, the time runs up to roughly 80,000 seconds. The event rate in the MWPC has a similar shape to that of the dark current, both decreasing, initially rapidly, and subsequently at a slower rate. This ties together the measurements of dark current made with the MWPC and ionisation chambers.

Including the measurements made with the gridded ionisation chamber as dark current measurements presents a coherent picture of charge transport in each liquid.

In DIN, the liquid which has been researched in most depth, the dark current seems to be composed of roughly constant contributions over time in uniform electric fields. The magnitude of this varies as a function of electric field. The effect of high electric fields on this liquid can further be explored by examining the data taken with the MWPC (and WPC), which show that there are fast pulses in the high field regions of the detector, consistent with molecular dissociation.

MIBP and MIPN have not been investigated in such depth, but from the gridded ionisation chamber data, and molecular structure, their behaviour is expected to be similar to that of DIN, with variations due to their different dielectric strengths.

In PXE, the dark current is more consistent with historical liquids, in that

the dark current decreases as a function of time. The different pulse populations identified in the dark current fit to the pulse populations identified historically to compose the dark current. The MWPC data also provides supporting evidence for molecular dissociation in the liquid in high field regions.

The dark current in LAB, increasing roughly uniformly as a function of electric field, is consistent between measurements using the gridded ionisation chamber, and the current detector. Both show a low level of charge transport compared to other liquids, which fits with historical evidence for poor charge transport in long chain molecular liquids.

In summary, in spite of the liquids not showing signs of transporting charge deposited by incident radiation, they show a consistent response to the presence of an electric field, and strong evidence of the presence of a dark current.

4.3 Optical readout of a THGEM in liquid scintillator

This setup was intended to combine both charge and optical readout of the liquids, in order to improve the knowledge of the pulse populations observed in the charge sensitive detectors, and see how they related to any optical observations.

Due to the limitations on the detector setup, as discussed in section 3.6, there is minimal data from this detector setup. Optical data was taken, using the incident PMTs with THGEM operational and non-operational as a function of drift field in PXE. Muons were used as the source, with a liquid depth of 2 cm, hence an expected energy deposition of 3.94 MeV.

Data was taken with drift fields of up to 5 kVcm^{-1} , since the high voltage input was limited to 5 kV by the high voltage feedthrough.

Data was taken in 5 hour samples across 2-3 days. However, it was found that the light output does not change significantly as a function of time for any of the drift voltages measured. An illustration of this is figure 4.46, which shows the pulse amplitude as a function of time, over 40 hours of data taking. Since measurements at all of the fields are consistent in this way, the results for each drift field are presented as a combined data sample across 20 hours.

Figure 4.47 shows the event rate as a function of drift field. The rate across all field strengths can be fitted with a straight line at 5188 ± 29 events per 20 hours. This shows that the sensitivity of the scintillation detector is unaffected by the presence of a drift field of up to 5 kVcm^{-1} .

Each pulse parameter seems to be similarly unaffected by a change in drift field. The pulse amplitude as a function of drift field can be fitted by a constant of

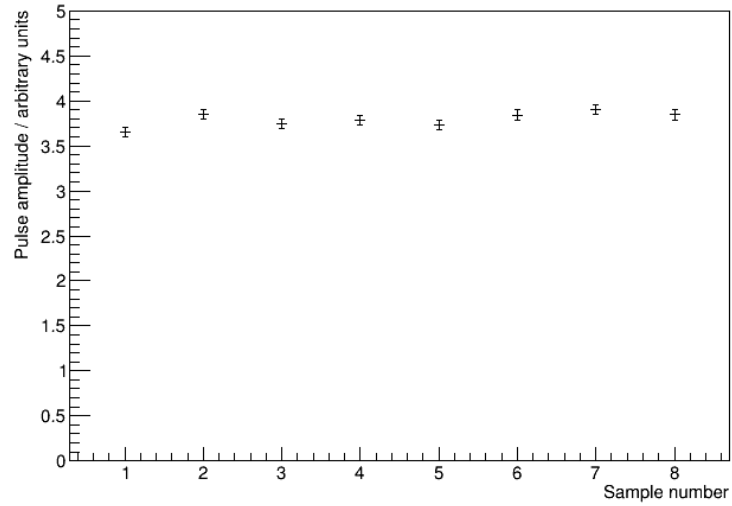


Figure 4.46: Pulse amplitude as a function of time with a drift field of 5 kVcm^{-1} . Samples were taken continuously, with 5 hours of data taking per sample.

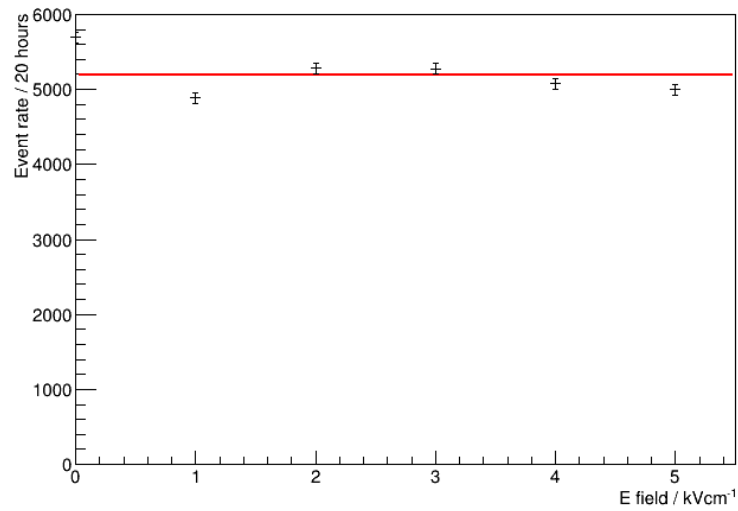


Figure 4.47: Event rate as a function of drift field, fitted with a straight line at 5188 ± 29 events per 20 hours.

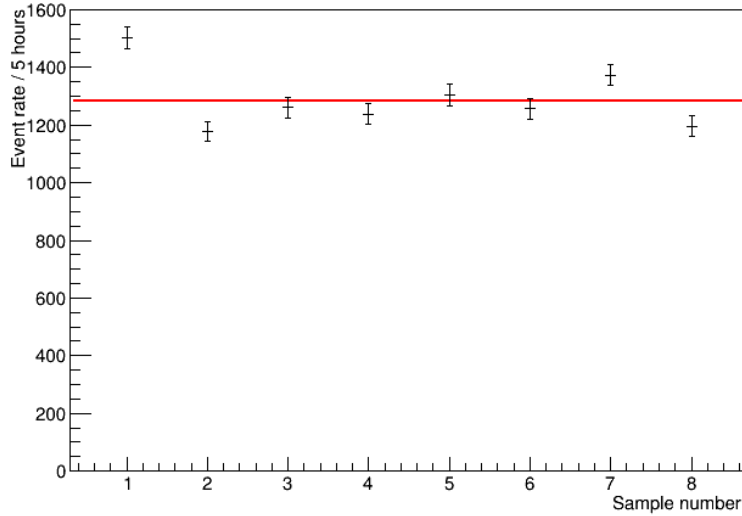


Figure 4.48: Event rate as a function of time, with THGEM operational. Each consecutive sample lasted 5 hours.

3.95 ± 0.011 (arbitrary units, comparable with the data in section 4.1.2) with a χ^2 value of 5.83 (5 degrees of freedom). This is within the error of the 2 cm muon peak measured in the 2 PMT (light only) measurement, shown in figure 4.14.

The rise time is fitted by a straight line fit value of $128.59 \pm 0.02 \text{ ns}$ with a χ^2 value of 67.25 (5 degrees of freedom). The spread of the data points for electric fields of between 0 and 5 kVcm^{-1} is 0.8 ns, and since the timing resolution is 5 ns, the variation is much smaller than one bin, and is therefore negligible.

Since the pulses retain the same properties irrespective of drift field ($< 5 \text{ kVcm}^{-1}$), it can be deduced that the light output is unaffected by the presence of a drift field.

Data was also taken with a bias of 1.5 kV across the THGEM, with a drift field of 3.5 kVcm^{-1} . The event rate as a function of time is shown in figure 4.48, with continuous sampling, and 5 hours of data per sample. The event rates in this data set likewise do not vary over time, and are well fitted by a straight line at 1281 ± 13 events per 5 hours. This shows that the effect of the THGEM on the light output does not change over time. In fact, the amount of light does not change with the THGEM operational, since the event rate with no THGEM, across all drift voltages (scaled to the appropriate time period), is within error of the rate fit with THGEM.

The pulse shapes show very little variation as a function of time. The pulse amplitude remains constant at a constant fit value of 3.792 ± 0.018 (arbitrary units), with a χ^2 value of 15.0 (7 degrees of freedom). Although this is lower than the

amplitude fit with the THGEM non-operational, it is still comparable to the 2 cm muon peak in PXE with no drift fields, as shown in figure 4.14.

The pulse rise times likewise remain constant as a function of time at a straight line fit value of 128.56 ± 0.05 ns, with a χ^2 value of 5.4 (7 degrees of freedom). As mentioned above, the timing resolution is 5 ns, therefore the pulse rise times in the detector with and without the THGEM operational are identical.

The light output of the detector does not seem to vary with operation of a THGEM over time, since the pulse parameters remain constant, and the optical sensitivity remains the same, with a constant rate as a function of time. Similarly, the optical behaviour of the detector does not change with and without a THGEM in operation.

Comparing this behaviour to other liquid scintillators with the ability to transport charge gives an insight into the behaviour of PXE.

In liquid argon, the scintillation light yield drops as the electric field and charge collection increase [67]. The electric fields prevent some of the recombination, as the charge is drifted and collected for readout.

Despite the inability in this project to measure both charge and light readout simultaneously in a single setup, it is probable that in the above experiment with the THGEM, the charge yield was nil (due to conservation of energy). Since the light yield in PXE did not decrease as a function of drift field, the ionisation charge yield from the incident radiation did not increase even at fields of 5 kVcm^{-1} .

This suggests that the ionisation electrons in the liquid scintillator are close enough to their corresponding ions to be dominated by the Coulomb field, making the external electric field negligible with respect to preventing recombination. This is further supported by the lack of change in light yield when the THGEM is operational, since the electric fields present in the THGEM holes would be much higher than those in the drift regions. The proximity of the electron-ion pairs suggests that the thermalisation drift path for ionisation electrons is short in this liquid.

In summary, the optical properties of PXE behave uniformly as a function of electric field and time, which is different to what one would expect where incident radiation was producing both detectable light and ionisation charge. This suggests a lack of measurable ionisation charge in this liquid.

Chapter 5

Discussion and Conclusions

It is indisputable that a liquid time projection chamber is well suited to rare event physics, especially where the liquid in the active medium has good scintillation properties, as well as high charge mobility. A TPC offers excellent granularity in tracking, described as an “electronic bubble chamber”[109], it enables topological particle identification. Combined scintillation light and charge collection gives excellent energy resolution. This, coupled with a potential for a larger target mass than gaseous counterparts, motivates the study of liquids with both charge transport and optical properties, for use in a TPC.

The favoured liquid with the above properties is liquid argon, which is an excellent scintillator, with high mobility. The disadvantage of liquid argon is that it requires a temperature of 87 K, which requires considerable cryogenic infrastructure, thus additional expense. This motivates the search for a room temperature liquid scintillator with high mobility for use in a large volume time projection chamber.

A large volume room temperature liquid TPC would have excellent potential, not only as the far detector for a long baseline neutrino experiment, but also as a large volume double beta decay detector, when loaded with isotopes. This thesis is concerned with the search for such a liquid, approaching it from two perspectives: the optical and charge properties.

The majority of the thesis is concerned with investigation of the charge transport properties in room temperature liquid scintillators. The liquid scintillators chosen were a class of liquid hydrocarbons with low toxicity, flash point and flammability, whose optical properties are well characterised, but charge transport properties had never previously been investigated. The liquids were investigated both as off-the-shelf liquid scintillator cocktails, and as the solvents forming the primary constituent of these cocktails, since a difference in behaviour was observed

between the two. The liquids tested were linear alkyl benzene (LAB), phenyl xylyl ethane (PXE), di isopropyl naphthalene (DIN), mono isopropyl naphthalene (MIPN) and mono isopropyl biphenyl (MIBP). The final two liquids are not typically used in scintillation cocktails; they were investigated in addition to the others due to the similarity of molecular structure to DIN, as shown in table 2.5.

The optical properties of the above liquids were investigated, in addition to two organic liquids historically shown to have good charge transport properties, whilst being relatively non-toxic: Cyclopentane (C5) and Tetramethyl pentane (TMP). Looking at the emission and absorption spectra of each of the liquids, as well as the response to ionising radiation, enabled comparison of the scintillation properties of the liquids. Since MIPN and MIBP are not used for scintillation either, this allowed us to determine their suitability.

The results, presented in section 4.1, show that out of the unknown liquids tested, only MIBP shows promise of being a good scintillator, as expected from the similarity of molecular structure to DIN. Since the scintillation properties of MIBP were previously unknown, this has potential impact for the company which manufactures both liquids.

Although TMP produces scintillation light under incident radiation, it cannot be described as a good scintillator. It exhibits signs of after-pulsing when the liquid is exposed to a high rate of radiation, and has low light output, and poor α/β discrimination.

MIPN and C5 both scintillate, and could operate as a low efficiency scintillator detector, but the amount of light output from the detector was, in the case of C5, 1-2 orders of magnitude lower than a commercial liquid scintillator cocktail, with a poor energy resolution. Some of this poor efficiency is due to the quantum efficiency of the PMT in the detector to the emitted wavelengths, but the light output was still around an order of magnitude less than DIN, which is a liquid with a similar peak emission wavelength. See section 4.1.1 for details of emission spectra, and table 4.3 for a summary of the optical results for each liquid.

For the investigation of the charge transport properties of these liquids, several detector setups were designed, constructed and commissioned. These were a wire proportional counter, a gridded ionisation chamber, and a multiwire proportional counter, which are all described in detail in chapter 3.

Through the use of these detectors, the liquids were discovered to have a time-dependent dark current in the presence of an electric field in the detector, analogous to the dark current historically observed in certain other hydrocarbons, as described in section 2.4.2. The dark current was measured both as a continuous

current, and for the first time in such a measurement, as charge pulses. These results are presented in section 4.2.3. The measurement of charge pulses gives a plethora of new information about the dark current. There were multiple pulse populations present in the data, which varied as a function of high voltage, and over time.

In the results chapter, hypotheses for the causes of the different pulse populations are presented, which are well motivated by both the data, and historical evidence. The verity of these hypotheses are not conclusively shown in this work, since the experiments required to do so are beyond the scope of this thesis, and are not motivated by its initial purpose.

Charge transport of ionisation electrons has not been successfully demonstrated in any of the above liquids. Several possible reasons for this are discussed below.

One reason is the purity of the liquids. Historical measurements of charge transport in room temperature liquids showed a large deterioration in signal for 1ppm impurities in the liquids. The initial observation of pulses in the detector with out-of-the-bottle liquids motivated the use of the liquids in this state, although effort was made to clean the liquids in-situ by inert gas bubbling. The purity of the detectors was historically found a challenge, with uncontrolled purity levels giving “scarcely reproducible” results [84], which is something I can certainly relate to. It is possible, therefore, that the impurities were present in the detector at too high of a level for charge transport to be measurable.

A second reason to consider is the amount of energy needed to liberate an electron-hole pair in the liquid. The optical test stand was used to measure light output from the liquid PXE in a small drift chamber with and without a THGEM readout plane operational, as described in section 3.6. The scintillation light output was identical irrespective of drift field value, and operation of the THGEM. This suggests that the thermalisation drift path for ionisation electrons is short, since the locality of the electron to its corresponding ion is enough that the drift fields of the detector are negligible compared to the Coulomb field.

As is shown by the dark current measurements, it is not the transport of the charge which is the problem in these liquids, but freeing the ionisation electrons. The room temperature liquids with measured mobility have been shown to have smaller numbers of ionisation electrons per unit energy than the noble liquids. This could likewise be due to the thermalisation drift path.

Bearing these factors in mind, in addition to the strong motivation for finding a room temperature liquid scintillator suitable to be the active medium for a TPC, the search for a suitable liquid is not over. This thesis has provided a strong starting

point for such a search.

Similarly to the two angles explored in this thesis, there are two distinct avenues of investigation, testing the optical and charge transport properties of room temperature liquids that have been measured to exhibit appropriate properties of either the former or the latter.

There are many room temperature liquids whose mobility has been measured. Although these liquids are for the most part volatile, toxic and dangerous to work with, the range of liquids will have different molecular structures, some of which may be excited in a way appropriate to an efficient scintillator.

Likewise, there are many room temperature liquid scintillators, whose mobility could be measured. These, again, include a class of liquids more dangerous than those tested in this thesis. With an existing awareness of the possibility of a dark current, it will be possible to design a measurement programme to effectively test the charge transport properties of these liquids.

In addition to this practical approach, there exist theoretical techniques which could be extremely beneficial to such an investigation. Companies such as Quantemol-N¹ offer products which can calculate electron-molecule scattering cross sections, using density functional theory. This would provide estimates for the thermalisation path length of ionisation electrons in a liquid, for a given molecule. Since the molecules in question are very large, by the standards of the programme, it is at the edge of the capability of such a technology. It would, however, offer the best starting point for searches for a liquid with the appropriate properties for charge transport.

In conclusion, the measurements presented in this thesis show no clear evidence for charge transport in the organic liquid scintillators tested, nor for suitable scintillation properties in the tested liquids with high mobility.

¹www.quantemol.com/products/quantemol-n/

Bibliography

- [1] N. McConkey, “Development of the Liquid Argon Detector Facility at Warwick,” MSc by Research in Physics, University of Warwick, October 2010.
- [2] N. McConkey and Y.A.Ramachers, “Liquid Scintillator Time Projection Chamber Concept,” *Nucl. Inst. Meth. A*, vol. 718, pp. 459–461, 2013.
- [3] N. McConkey and Y.A.Ramachers, “Liquid Scintillator Time Projection Chamber Concept - time dependence in organic liquids,” *JINST*, vol. 9, p. C03058, 2014.
- [4] W. Pauli, December 1930. Open letter to the Physical Institute of the Federal Institute of Technology Zurich meeting in Tübingen, Germany.
- [5] K. Zuber, *Neutrino Physics*. Institute of Physics, 2004.
- [6] J. Chadwick, “The intensity distribution in the magnetic spectrum of beta particles from radium (B + C),” *Verh.Phys.Gesell.*, vol. 16, pp. 383–391, 1914.
- [7] E. Fermi, “An attempt of a theory of beta radiation. 1,” *Z. Phys.*, vol. 88, pp. 161–177, 1934.
- [8] F. Reines, C. L. Cowan, F. B. Harrison, A. D. McGuire, H. W. Kruse, “Detection of the Free Antineutrino,” *Phys. Rev. Lett.*, vol. 117, no. 1, 1960.
- [9] B. Pontecorvo, “Electron and muon neutrinos,” *Sov. Phys. JETP*, vol. 10, pp. 1236–1240, 1960.
- [10] G. Danby *et al.*, “Observation of High-Energy Neutrino Reactions and the Existence of Two Kinds of Neutrinos,” *Phys.Rev.Lett.*, vol. 9, pp. 36–44, 1962.
- [11] M. L. Perl *et al.*, “Evidence for Anomalous Lepton Production in $e^+ - e^-$ Annihilation,” *Phys.Rev.Lett.*, vol. 35, pp. 1489–1492, 1975.

- [12] D. Decamp *et al.*, “Determination of the Number of Light Neutrino Species,” *Phys.Lett.*, vol. B231, p. 519, 1989.
- [13] S. Schael *et al.*, “Precision electroweak measurements on the Z resonance,” *Phys.Rept.*, vol. 427, pp. 257–454, 2006.
- [14] A. Aguilar-Arevalo *et al.*, “Evidence for neutrino oscillations from the observation of anti-neutrino(electron) appearance in a anti-neutrino(muon) beam,” *Phys.Rev.*, vol. D64, p. 112007, 2001.
- [15] K. Kodama *et al.*, “Observation of tau neutrino interactions,” *Physics Letters B*, vol. 504, no. 3, pp. 218 – 224, 2001.
- [16] C. Giunti and C. W. Kim, *Neutrino Physics and Astrophysics*. Oxford University Press, 2007.
- [17] R. Davis, D. S. Harmer, and K. C. Hoffman, “Search for Neutrinos from the Sun,” *Phys. Rev. Lett.*, vol. 20, no. 21, 1965.
- [18] J. N. Bahcall, A.M. Serenelli and S. Basu, “New Solar Opacities, Abundances, Helioseismology and Neutrino Fluxes,” *ApJ*, vol. 621, no. 1, 2005.
- [19] T. A. Kirsten *et al.*, “GALLEX solar neutrino results and status of GNO,” *Physics Letters B*, vol. 447, no. 1, 1999.
- [20] V. N. Gavrin *et al.*, “Solar neutrino results from SAGE,” *Physics Letters B*, vol. 447, no. 1, 1999.
- [21] Y. Fukuda *et al.*, “Measurements of the Solar Neutrino Flux from Super-Kamiokande’s First 300 Days,” *Phys. Rev. Lett.*, vol. 81, no. 6, 1998.
- [22] Q. Ahmad *et al.*, “Direct Evidence for Neutrino Flavor Transformation from Neutral-Current Interactions in the Sudbury Neutrino Observatory,” *Phys. Rev. Lett.*, vol. 89, no. 1, 2002.
- [23] Y. Fukuda *et al.*, “Evidence for Oscillation of Atmospheric Neutrinos,” *Phys. Rev. Lett.*, vol. 81, no. 8, 1998.
- [24] W. Allison *et al.*, “Measurement of the atmospheric neutrino flavor composition in Soudan-2,” *Phys.Lett.*, vol. B391, pp. 491–500, 1997.
- [25] C. Mariani *et al.*, “K2K recent results,” *AIP Conf.Proc.*, vol. 981, pp. 247–249, 2008.

- [26] J. Hewett, H. Weerts, R. Brock, J. Butler, B. Casey, *et al.*, “Fundamental Physics at the Intensity Frontier,” *arXiv:1205.2671 [hep-ex]*, 2012.
- [27] L. Chau and W. Keung, “Comments on the Parametrization of the Kobayashi-Maskawa Matrix,” *Physical Review Letters*, vol. 53, pp. 1802–1805, 1984.
- [28] K. Olive *et al.*, “Review of Particle Physics,” *Chin.Phys.*, vol. C38, p. 090001, 2014.
- [29] S. Mikheyev and A. Smirnov, “Resonant Amplification of ν Oscillations in Matter and Solar-Neutrino Spectroscopy,” *Il Nuovo Cimento C*, vol. 9, pp. 17–26, 1986.
- [30] L. Wolfenstein, “Neutrino oscillations in matter,” *Phys. Rev. D*, vol. 17, pp. 2369–2374, 1978.
- [31] E. Kolb and M. S. Turner, *The Early Universe*. Addison-Wesley, 1990.
- [32] J. Christenson, J. Cronin, V. Fitch, and R. Turlay, “Evidence for the 2 pi Decay of the $k(2)0$ Meson,” *Phys.Rev.Lett.*, vol. 13, pp. 138–140, 1964.
- [33] K. Abe *et al.*, “Observation of large CP violation in the neutral B meson system,” *Phys.Rev.Lett.*, vol. 87, p. 091802, 2001.
- [34] B. Aubert *et al.*, “Observation of CP violation in the B^0 meson system,” *Phys.Rev.Lett.*, vol. 87, p. 091801, 2001.
- [35] W. Buchmuller, R. Peccei, and T. Yanagida, “Leptogenesis as the origin of matter,” *Ann.Rev.Nucl.Part.Sci.*, vol. 55, pp. 311–355, 2005.
- [36] S. Bauer, R. Berendes, F. Hochschulz, H.-W. Ortjohann, S. Rosendahl, *et al.*, “Next generation KATRIN high precision voltage divider for voltages up to 65kV,” *JINST*, vol. 8, p. P10026, 2013.
- [37] N. Haba and R. Takahashi, “Constraints on neutrino mass ordering and degeneracy from Planck and neutrino-less double beta decay,” *arXiv:1305.0147 [hep-ph]*, 2013.
- [38] L. Winslow *et al.*, “Characterizing quantum-dot-doped liquid scintillator for applications to neutrino detectors,” *JINST*, vol. 7, p. P07010, 2012.
- [39] P. Harris *et al.*, “The MINOS light injection calibration system,” *Nuclear Instruments and Methods A*, vol. 492, pp. 325–343, 2002.

- [40] L. H. Whitehead *et al.*, “The MINOS Experiment and MINOS+,” in *The proceedings of International Workshop on Next generation Nucleon Decay and Neutrino Detectors*, 2013.
- [41] J. Bian, “The NO ν a experiment: overview and Status,” in *arXiv:1309.7898 [physics.ins-det]*, 2013.
- [42] N. Agafonova *et al.*, “New results on $\nu_\mu \rightarrow \nu_\tau$ appearance with the OPERA experiment in the CNGS beam,” *arXiv:1308.2553 [hep-ex]*, 2013.
- [43] N. Agafonova *et al.*, “Evidence for $\nu_\mu \rightarrow \nu_\tau$ appearance in the CNGS neutrino beam with the OPERA experiment,” *arXiv:1401.2079 [hep-ex]*, 2014.
- [44] S. Amerio *et al.*, “Design construction and tests of the ICARUS T600 detector,” *Nuclear Instruments and Methods A*, vol. 527, pp. 329–410, 2004.
- [45] K. Abe *et al.*, “Observation of electron neutrino appearance in a muon neutrino beam,” *arXiv:1311.4750 [hep-ex]*, 2013.
- [46] O. Cremonesi and M. Pavan, “Challenges in double beta decay,” *arXiv:1310.4692 [physics.ins-det]*, 2013.
- [47] B. Schwingenheuer, “Status and prospects of searches for neutrinoless double beta decay,” *Annalen Phys.*, vol. 525, pp. 269–280, 2013.
- [48] J. Gómez-Cadenas *et al.*, “Sense and sensitivity of double beta decay experiments,” *JCAP*, vol. 1106, p. 007, 2011.
- [49] Albert, J.B. *et al.* [EXO-200 Collaboration], “Search for Majoron-emitting modes of double-beta decay of ^{136}Xe with EXO-200,” *Phys.Rev.*, vol. D90, no. 9, p. 092004, 2014.
- [50] J. Gómez-Cadenas *et al.*, “Present status and future perspectives of the NEXT experiment,” *IFIC*, vol. 46, 2013.
- [51] J. Maneira *et al.*, “SNO+ experiment: status and overview,” *J. Phys.: Conf. Series*, vol. 447, p. 012065, 2013.
- [52] S. Biller, “SNO+ with Tellurium,” *arXiv:1405.3401 [physics.ins-det]*, 2014.
- [53] A. Gando *et al.*, “Measurement of the double-decay half-life of ^{136}Xe with the KamLAND-Zen experiment,” *Phys. Rev. C*, vol. 85, p. 045504, 2012.

- [54] Y. Huang and B.-Q. Ma, “Constraints on absolute neutrino Majorana mass from current data,” *arXiv:1407.4357 [hep-ph]*, 2014.
- [55] A. Barabash *et al.*, “SuperNEMO double beta decay experiment,” *arXiv:1112.1784 [nucl-ex]*, 2011.
- [56] S. D. Dominizio *et al.*, “Status of the CUORE and CUORE-0 experiments at Gran Sasso,” in *24th Workshop on Weak Interactions and Neutrinos*, 2013.
- [57] M. Agostini *et al.*, “Results on neutrinoless double beta decay of ^{76}Ge from GERDA Phase I,” *Phys.Rev.Lett.*, vol. 111, p. 122503, 2013.
- [58] R. Martin *et al.*, “Status of the MAJORANA DEMONSTRATOR experiment,” *arXiv:1311.3310 [physics.ins-det]*, 2013.
- [59] C. Adams *et al.*, “Scientific Opportunities with the Long-Baseline Neutrino Experiment,” *arXiv:1307.7335 [hep-ex]*, 2013.
- [60] D. Wark, “Current and future prospects on long-baseline experiments in europe,” in *NuPhys*, 2013.
- [61] H.-K. W. Group, “Hyper-kamiokande physics opportunities,” *arXiv:1309.0184 [hep-ex]*, 2013.
- [62] C. Gruppen and B. Shwartz, *Particle Detectors*. Cambridge University Press, second edition ed., 2008.
- [63] J. Knoll, *Radiation Detection and Measurement*. Wiley, 3rd ed., 2000.
- [64] E. Buckley *et al.*, “A study of ionization electrons drifting over large distances in liquid argon,” *Nuclear Instruments and Methods A*, vol. 275, pp. 364–372, 1989.
- [65] A. Breskin *et al.*, “A concise review on THGEM detectors,” *Nuclear Instruments and Methods A*, vol. 598, pp. 107–111, 2009.
- [66] R. Chechik *et al.*, “Advances in Thick GEM-like gaseous electron multipliers - Part I: atmospheric pressure operation,” *Nuclear Instruments and Methods A*, vol. 558, pp. 475–489, 2006.
- [67] E. Aprile *et al.*, *Noble Gas Detectors*. Wiley-VCH, 2006.
- [68] P. Lightfoot *et al.*, “Optical readout tracking detector concept using secondary scintillation from liquid argon generated by a thick gas electron multiplier,” *JINST*, vol. 4, p. P04002, 2009.

- [69] D. Stewart *et al.*, “Modelling electroluminescence in liquid argon,” *JINST*, vol. 5, p. P10005, 2010.
- [70] H. Spieler, *Semiconductor Detector Systems*. Oxford University Press, 2005.
- [71] Y. K. Suh, “Modeling and Simulation of Ion Transport in Dielectric Liquids Fundamentals and Review,” *IEEE Transactions on Dielectrics and Electrical Insulation*, vol. 19, pp. 831–848, 2012.
- [72] J. Engler and H. Keim, “A Liquid Ionisation Chamber using Tetramethylsilane,” *Nucl. Instr. Meth. A*, vol. 223, pp. 47–51, 1984.
- [73] M. Cohen and J. Lekner, “Theory of hot electrons in gases, liquids, and solids,” *Physical Review*, vol. 158, pp. 305–309, 1967.
- [74] J. Engler, “Liquid ionization chambers at room temperatures,” *Journal of Physics G: Nuclear and Particle Physics*, vol. 22, pp. 1–23, 1996.
- [75] R. A. Holroyd and M. Allen, “Energy of Excess Electrons in Nonpolar Liquids by Photoelectric Work Function Measurements,” *J. Chem. Phys.*, vol. 54, p. 5014, 1971.
- [76] R. M. Minday, L. D. Schmidt, and H. T. Davis, “Mobility of Excess Electrons in Liquid Hydrocarbon Mixtures,” *J. Chem. Phys.*, vol. 76, p. 443, 1971.
- [77] P.H. Tewari and G.R. Freeman, “Dependence of Radiation Induced Conductance of Liquid Hydrocarbons on Molecular Structure,” *J Chem. Phys.*, vol. 49, p. 4394, 1968.
- [78] I. Adamczewski and J. H. Calderwood, “The mobility of fast charge carriers in liquid paraffins and its dependence on molecular structure,” *J. Phys. D: Appl. Phys.*, vol. 9, pp. 2479–2483, 1976.
- [79] W. Schmidt, *Liquid State Electronics of Insulating Liquids*. CRC Press, 1997.
- [80] M. Albrow *et al.*, “Performance of a uranium / tetramethylpentane electromagnetic calorimeter,” *Nucl. Instr. Meth. A*, vol. 265, pp. 303–318, 1988.
- [81] M. Chara and D. E. Watt, “Charge transport in liquid tetramethylsilane (TMS) at low and high electric fields,” *Nucl. Instr. Meth B*, vol. 184, pp. 615–626, 2001.
- [82] H. J. Plumley, “Conduction of Electricity by Dielectric Liquids at High Field Strengths,” *Physical Review*, vol. 59, pp. 200–207, 1941.

- [83] C. Pao, “Conduction of Electricity in Highly Insulating Liquids,” *Physical Review*, vol. 64, pp. 60–74, 1943.
- [84] M. P. M. Ladu and M. Roccella, “On the Background Current in the Dielectric Liquid Ionisation Chambers,” *Nucl. Inst. Meth.*, vol. 37, pp. 318–322, 1965.
- [85] T. Nakayama and M. Kawano, “Background Current of the Liquid Ionisation Chamber,” *Nucl. Inst. Meth.*, vol. 108, pp. 203–204, 1973.
- [86] D. André, “Conduction and breakdown initiation in dielectric liquids,” in *IEEE International Conference on Dielectric Liquids (ICDL) Proceedings*, 2011.
- [87] M. F. L’Annunziata, *Handbook of Radioactivity Analysis*. Academic Press, 2nd ed., 2003.
- [88] H. Band *et al.*, “Assembly and installation of the daya bay antineutrino detectors,” *JINST*, vol. 8, p. 11006, 2013.
- [89] J.K.Ahn *et al.*, “Observation of Reactor Electron Antineutrino Disappearance in the RENO Experiment,” *Phys. Rev. Lett.*, vol. 108, p. 191802, 2012.
- [90] E. O. H.M. O’Keeffe and M. Chen, “Scintillation decay time and pulse shape discrimination in oxygenated and deoxygenated solutions of linear alkylbenzene for the SNO+ experiment,” *Nucl. Inst. Meth. A*, vol. 640, pp. 119–122, 2011.
- [91] Y. Abe *et al.*, “Reactor ν_e disappearance in the double chooz experiment,” *Phys. Rev. D*, vol. 86, p. 052008, 2012.
- [92] H. O. Back *et al.*, “Study of phenylxylylethane (PXE) as scintillator for low energy neutrino experiments,” *Nucl. Inst. Meth. A*, vol. 585, pp. 48–60, 2008.
- [93] J. Thomson, “Proceedings of the International Conference on New Trends in Liquid Scintillation Counting and Organic Scintillators, Chapter 3,” *Proceedings of the International Conference on New Trends in Liquid Scintillation Counting and Organic Scintillators*, pp. 19–33, 1989.
- [94] Lombardi *et al.*, “Decay time and pulse shape discrimination of liquid scintillators based on novel solvents,” *Nucl.Instrum.Meth.*, vol. A701, pp. 133–144, 2013.

- [95] J. Maruer, “Operation and performance of the ATLAS liquid argon electromagnetic calorimeters,” *PoS*, vol. EPS-HEP2013, p. 039, 2014.
- [96] W. Wahl, *Alpha, beta, gamma tables of commonly used radionuclides*. Institute for spectrometry and radiation protection, Schliersee, Germany, 1996.
- [97] Perkin Elmer, *Opti Fluor O Safety Data Sheet*, 2009.
- [98] Perkin Elmer, *Ultima Gold F Safety Data Sheet*, 2009.
- [99] National Diagnostics, *Ecoscint O Material Safety Data Sheet*, 2009.
- [100] Fisher Scientific, *Di-iso-propylnaphthalene Safety Data Sheet*, 2012.
- [101] Dixie Chemical Company Inc., *PXE Material Safety Data Sheet*, 2010.
- [102] Ruetgers, *Ruetasolv MP Technical Datasheet*, 2011.
- [103] Ruetgers, *Ruetasolv BP 4103 Technical Datasheet*, 2011.
- [104] Alfa Aesar, *2,2,4,4-Tetramethylpentane Material Safety Data Sheet*, 2012.
- [105] Sigma-Aldrich, *Cyclopentane Safety Data Sheet*, 2013.
- [106] COMSOL, *Comsol Multiphysics*, 4.4.0.150 ed., 2013.
- [107] Electron Tubes, *9954B series data sheet*, 2010.
- [108] R. Brun and F. Rademakers, “Root - an object oriented data analysis framework,” *Nucl. Inst. Meth. A*, pp. 81–86, 1997. Proceedings AIHENP’96 Workshop, Lausanne, September 1996.
- [109] C. Rubbia, “The ICARUS Liquid Argon TPC: A neutrino ‘bubble chamber after Gargamelle,” *J.Phys.Conf.Ser.*, vol. 308, p. 012002, 2011.